Lehrstuhl für Biomedizinische Physik
Physik Department
Technische Universität München

PhD Thesis

PHOTON-COUNTING HYBRID-PIXEL DETECTORS FOR SPECTRAL X-RAY IMAGING APPLICATIONS

SEBASTIAN EHN

2017

Supervisors: Prof. Dr. Franz Pfeiffer
PD Dr. Peter Noël

Dedicated to my family...

TECHNISCHE UNIVERSITÄT MÜNCHEN
Physik Department
Lehrstuhl für Biomedizinische Physik

Photon-counting hybrid-pixel detectors for spectral x-ray imaging applications

Sebastian Siegfried Lukas Ehn

Vollständiger Abdruck der von der Fakultät für Physik der Technischen Universität München zur Erlangung des akademischen Grades eines

Doktors der Naturwissenschaften (Dr. rer. nat.)

genehmigten Dissertation.

Vorsitzender:	apl. Prof. Dr. Norbert Kaiser
Prüfer der Dissertation:	1. Prof. Dr. Franz Pfeiffer
	2. Prof. Dr. Laura Fabbietti

Die Dissertation wurde am 22. 6. 2017 bei der Technischen Universität München eingereicht und durch die Fakultät für Physik am 3. 7. 2017 angenommen.

Abstract

This thesis focuses on the use and optimization of spectral x-ray imaging methods based on energy-discriminating photon-counting detectors in medical and material-scientific applications.
Photon-counting detectors offer improvements over conventional detectors by added energy discrimination capabilities and absence of dark current and dynamic range down to zero photons. To assist the development of novel image processing algorithms required by such systems, a simulation framework for photon-counting detectors was designed and implemented. A method to reduce the extensive calibration efforts required by today's spectral imaging approaches was developed offering a projection-based estimator for material decomposition based on a semi-empirical model of registered detector signals. Experimental measurements verified the quantitative accuracy of the proposed methods to lie within a few percent of the theoretical values and show some preliminary applications of projection-based material decomposition in material science micro-CT.

Zusammenfassung

Die vorliegende Arbeit befasst sich mit der Umsetzung und Optimierung von spektralen Röngenbildgebungsmethoden basierend auf energie-sensitiven photonenzählenden Detektoren. In medizinischen und materialwissenschaftlichen Anwendungen bieten photonenzählende Detektoren weitreichende Vorteile gegenüber konventionallenen Detektoren, darunter die Möglichkeit der Energieunterscheidung sowie das Fehlen eines Dunkelstroms und der daraus resultierende weite dynamische Bereich. Im Zuge der Arbeit wurde eine Simulation für photonenzählende Detektoren implementiert um die Entwicklung neuer Bildverarbeitungsalgorithmen zu unterstützen. Eine neue Methode zur pojektionsbasierten Materialzerlegung in der spektralen Bildgebung wurde auf der Basis eines semi-empirischen Vorwärtsmodells für das erhaltene Detektorsignal entwickelt. Mittels experimenteller Messungen wurde die Genauigkeit der entwickelten Methoden evaluiert und ergab eine Abweichung innerhalb nur weniger Prozent der theoretischen Werte. Etliche erste Anwendungen von projektionsbasierter Materialzerlegung im Bereich der materialwissenschaftlichen Micro-CT wurden zudem untersucht.

Contents

1 Introduction

Over the last decades, x-ray imaging methods have become an invaluable tool in clinical diagnostics as well as for industrial and scientific purposes. Especially the development of x-ray CT in the early 1970's [Hounsfield1973] has revolutionized diagnostic and material scientific imaging as it offers quantitative measurements of the three-dimensional (3D) distribution of the attenuation properties. The introduction of helical CT in the 1990's has enabled fast and continuous scanning of large volumes [Kalender1990]. The availability of high-power x-ray sources and advances in semiconductor technology with rapidly increasing computing power resulted in the development of multi-slice CT where today's scanners offer simultaneous acquisition of several hundred slices at reduced radiation dose. The competition between vendors in the years after 2000 to offer the scanner with the largest spatial and temporal resolution is often dubbed the 'slice-wars' [Mahesh2009].
In the field of industrial and material scientific imaging, the development of large-area digital x-ray detectors lead to the application of cone-beam CT for high-resolution at the micro-meter scale [Flannery1987, Lee2003].
In the more recent years spectral x-ray imaging methods have come into the focus of research fueled by the need for improved image quality at reduced radiation dose and the trend towards functional (or physiologic) imaging[1] in clinical diagnostics and pre-clinical research [Lee2002, VanBeek2008]. Measuring at different energy levels, spectral imaging methods exploit the energy-dependent attenuation of x-rays by different materials to extract information about the chemical composition of the object. Dual-energy spectral imaging was proposed in a clinical context already a few years after the invention of CT itself [Alvarez1976] and its mathematical properties derived [Alvarez1979, Kelcz1979]. For a long time since then this technique has not been very popular due to limited image quality and lack of processing capability. The introduction of the first dual-source CT scanner in 2005 [Flohr2006] operating with two tube-detector pairs to acquire two energy channels simultaneously can be considered a breakthrough for dual-energy CT imaging and numerous medical applications have been identified so far [McCollough2015]. Since then spectral imaging methods have gained a lot of renewed interest.

[1] Opposed to mere structural imaging, functional imaging probes the physiological activities of the metabolism in specific types of tissue. Common examples in CT are blood perfusion of lung vessels or an assessment of the vascular structure of neoplastic lesions.

One of the latest developments in x-ray imaging is the development and implementation of single PCDs. Originally developed for application in high-energy physics and now adopted to x-ray imaging [Anghinolfi1992, Delpierre2014], such detectors are designed to register and process each arriving photon individually. Thereby, PCDs offer many advantages over conventional detection systems including equal weighting of all registered photons in the image, energy discrimination capability and absence of dark current [Ballabriga2016]. In the context of imaging, capability to acquire multiple (≈ 5) energy images at the same time can allow to distinguish between several different materials in an object while the absence of dark current drastically improves the detected signal-to-noise ratio (SNR) at very counts of ≤ 10 photons where the Poisson statistics dominates. This might allow a considerable reduction of radiation exposure which is an all-important goal in medical imaging as well as measurement time in micro-CT. However, the application of PCDs usually requires increased efforts and special methods for data handling and image processing.

With these developments in mind, this thesis focuses on the advancement of spectral x-ray imaging techniques in general and specifically it investigates new methods for the application of PCDs in x-ray imaging. After recapitulating the basic theory of spectral x-ray imaging and PCD technology in the following two chapters we will discuss a simulation framework applicable to spectral imaging and present a material decomposition scheme based on a novel forward-model for the registered signal in PCDs. Practical implementation of these methods in an experimental set-up will be presented in chapter 7 where the performance of the proposed methods is validated experimentally and several novel applications in material science and non-destructive testing (NDT) micro-CT are explored. Finally, a novel approach to obtain sub-pixel resolution with PCDs will be outlined and a short outlook to future studies and research will be given.

2 Principles of spectral x-ray imaging

In the following sections a brief overview of the basic theoretical concepts used throughout this work is given. The first section presents the fundamental physics of x-ray interaction with matter which need to be understood to derive the concepts presented in the work. Afterwards the physical and mathematical framework of spectral x-ray imaging is discussed.

2.1 Interaction of x-rays with matter

Classically, the attenuation of a monochromatic beam of x-rays with energy E and intensity I_0 passing a homogeneous object of thickness d is described by Beer-Lambert's law:

$$I(d) = I_0 \mathrm{e}^{-\mu(E)\cdot d}. \tag{2.1}$$

The linear attenuation coefficient $\mu(E)$ describes the energy-dependent attenuation properties of the materials inside the object. On the atomic scale it is related to the total atomic interaction cross-sections σ_a via the mass density ρ of the object:

$$\frac{\mu}{\rho}(E) = \frac{1}{\rho}\frac{\rho N_\mathrm{A}}{A}\sigma_\mathrm{a}(E), \tag{2.2}$$

where N_A is Avogardo's number and A is the atomic weight.

Setting the focus on diagnostic and material scientific applications of x-ray imaging the typical energy range to be used is more or less constrained by $10\,\mathrm{keV} \leq E \leq 250\,\mathrm{keV}$. In this range the total atomic cross section is the sum of three contributing interaction mechanisms: Photoelectric effect, elastic

(coherent) scattering and inelastic (incoherent) scattering. Characterizing each chemical element by its atomic number Z, the cross-section can be written as

$$\sigma_{\mathrm{a}}(Z,\, E) = \sigma_{\mathrm{a}}^{\mathrm{ph}}(Z,\, E) + \sigma_{\mathrm{a}}^{\mathrm{coh}}(Z,\, E) + \sigma_{\mathrm{a}}^{\mathrm{incoh}}(Z,\, E). \tag{2.3}$$

For any compound material the mass attenuation coefficient is obtained by applying the mixture rule:

$$\begin{aligned} \frac{\mu}{\rho}(E) &= \sum_i w_i \left(\frac{\mu}{\rho}(E)\right)_i, \\ w_i &= \frac{n_i A_i}{\sum_j n_j A_j}, \end{aligned} \tag{2.4}$$

where i, j index all chemical elements present in the mixture or compound, w_i are the mass fractions of each element contributing to the mixture, n_i are the associated stoichiometric coefficients and A_i the atomic weight.

A strict analytic treatment of the processes in equation 2.3 requires a rigorous quantum-mechanical description of the photon-atom interaction with relativistic corrections and different approaches of perturbation theory [Cohen-Tannoudji2004] and is therefore very cumbersome and elaborate. Consequently we will focus here only on the basic results for the individual cross-sections and discuss approximations and limits where appropriate. A concise review of the quantum-mechanical description and its approximations can e. g. be found in [Jackson1981].
In many cases the dependencies on the energy and the atomic number can not be separated when parameterizing the atomic cross-sections. However, spectral imaging methods used today rely on a strict separation of these contributions and therefore separable approximations of the form

$$\sigma(Z,\, E) \simeq f(E) Z^m,\ m \in \mathbb{R} \tag{2.5}$$

are frequently employed.

Photoelectric effect

The photoelectric effect involves the transition of an atomic electron from a bound to an unbound (continuum) state. This process can be described by a superposition of a continuous part and the edge jumps when the energy of the incident photons is large enough to eject electrons from the next atomic shell. In absence of absorption edges the cross-section for the photoelectric effect is often approximated by [White1977]

$$\sigma_{\mathrm{a}}^{\mathrm{ph}}(Z,\, E) = C_{\mathrm{ph}} \frac{1}{E^{2.5-3.5}} Z^{4-5}. \tag{2.6}$$

The exact value for the exponents depends on the specific element or mixture to be parameterized. Since biological tissues normally contain only light elements with $Z \leq 20$, the absorption edges are located below the energy range of interest and approximation 2.6 is reasonably accurate. For heavier elements the k-edges lie within the used range of energies and a separation of the form 2.5 is no longer possible[1]. In such cases, tabulated values for the mass absorption coefficients are normally used in spectral x-ray imaging.

X-ray scattering

Scattering contributions to the total atomic cross-section can be divided into elastic and inelastic processes:

- **Elastic scattering:**

  Elastic scattering of x-rays from electrons is called Thomson scattering when the electrons can be considered free (low energy limit) and Rayleigh or coherent scattering when it involves bound electrons. The classical Thomson cross-section for scattering from a single electron is independent of the photon energy and given by

$$\sigma^{\mathrm{Th}} = \frac{8\pi}{3} \left(\frac{e^2}{m_{\mathrm{e}} c^2} \right)^2. \tag{2.7}$$

[1] An important case for this is the use of contrast agents like I or Gd in clinical radiology.

The total cross section for coherent scattering from atoms (bound electrons) is given by

$$\sigma_{\mathrm{a}}^{\mathrm{coh}}(Z,\, E) = \int F_0(Z,\, E) \frac{\mathrm{d}\sigma^{\mathrm{Th}}}{\mathrm{d}\Omega} \mathrm{d}\Omega, \tag{2.8}$$

where $F_0(Z,\, E)$ is the atomic form factor. A separation of energy- and Z-dependency is not easily possible for the above equation. However, the limits of

$$\begin{aligned} &\lim_{E\to 0} F_0(Z,\, E) = Z^2 \text{ and} \\ &\lim_{E\to \infty} F_0(Z,\, E) = 0 \end{aligned} \tag{2.9}$$

imply that

$$\begin{aligned} &\lim_{E\to 0} \sigma_{\mathrm{a}}^{\mathrm{coh}}(Z,\, E) = Z^2 \sigma^{\mathrm{Th}} \text{ and} \\ &\lim_{E\to \infty} \sigma_{\mathrm{a}}^{\mathrm{coh}}(Z,\, E) = 0. \end{aligned} \tag{2.10}$$

- **Inelastic scattering:** The general relativistic expression for the differential cross section of photon scattering from unbound electrons is given by the Klein-Nishina formula

$$\begin{aligned} \frac{\mathrm{d}\sigma^{\mathrm{KN}}}{\mathrm{d}\Omega}(E) &= \frac{1}{2} \left(\frac{e^2}{m_{\mathrm{e}} c^2} \right)^2 y^2 \left[y + \frac{1}{y} - \sin^2\theta \right], \\ y &= \frac{1}{1 + \epsilon(1 - \cos\theta)}, \\ \epsilon &= \frac{E}{m_{\mathrm{e}} c^2}, \end{aligned} \tag{2.11}$$

where θ is the angle of scattering. This expression reduces to the classical Thomson cross-section for small energies, i. e. $E \ll m_{\mathrm{e}} c^2$.

Similar to equation 2.8, the total cross-section for general inelastic scattering is given by

$$\sigma_{\mathrm{a}}^{\mathrm{incoh}}(Z,\, E) = \int ZS(E)\frac{\mathrm{d}\sigma^{\mathrm{KN}}}{\mathrm{d}\Omega}\mathrm{d}\Omega, \tag{2.12}$$

where $ZS(E)$ is the incoherent scattering function [Hubbell1975, Hubbell1997]. It has the limits

$$\begin{aligned} &\lim_{E\to 0} ZS(E) = 0 \ \text{ and} \\ &\lim_{E\to \infty} ZS(E) = Z. \end{aligned} \tag{2.13}$$

Therefore at higher energies the incoherent scattering cross-section becomes

$$\sigma_{\mathrm{a}}^{\mathrm{incoh}}(Z,\, E) = Z\sigma^{\mathrm{KN}} \tag{2.14}$$

Despite the fact that atomic electrons can neither be considered free nor at rest, this process described by the equations 2.12 - 2.14 is usually referred to as Compton-scattering in x-ray imaging physics.

Tabulated values of the mass attenuation coefficients according to equation 2.2 are plotted in figure 2.1 for soft tissue and bone (International Commission on Radiation Units (ICRU) report 44) [ICRU44]. Generally, photoelectric absorption dominates the mass attenuation coefficients at smaller energies up to a few $10\,\mathrm{keV}$. Towards higher energies, scattering effects become more important. The amount of incoherent scattering is normally stronger compared to coherent scattering, however the exact point where both effects are equal depends strongly on the investigated material. For example in bone, incoherent scattering is approximately one order of magnitude higher for energies $\geq 60\,\mathrm{keV}$ and almost two orders of magnitude stronger for $E \geq 100\,\mathrm{keV}$. This observation often leads to the assumption that coherent scattering can safely be neglected in x-ray imaging applications. Under these assumptions and putting together the equations 2.2, 2.5, 2.6 and 2.12 the energy-dependent mass attenuation coefficient of an arbitrary material without k-edges in the interesting energy range can be parameterized by

$$\frac{\mu}{\rho}(E) = a_{\mathrm{Ph}} f_{\mathrm{Ph}}(E) + a_{\mathrm{C}} f_{\mathrm{KN}}(E), \tag{2.15}$$

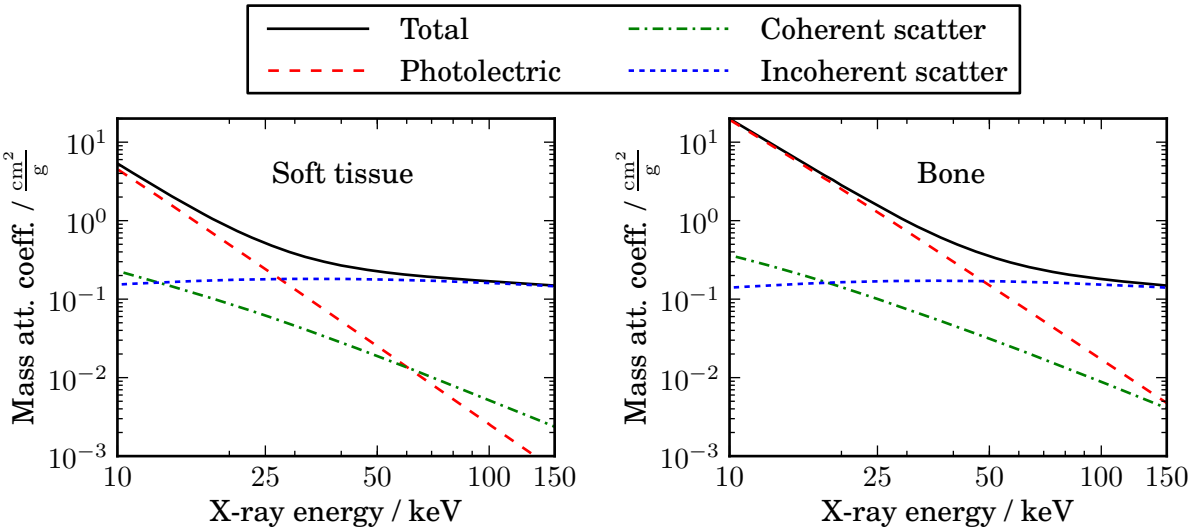

Figure 2.1: **X-ray mass attenuation coefficients for soft-tissue and bone.** The plots show the tabulated values for all involved interaction mechanisms [ICRU44]. At higher energies, coherent scattering effects are much smaller compared to incoherent scattering. E. g. in bone, the contribution of incoherent scattering is approximately one order of magnitude stronger for energies $\geq$ 60 keV and almost two orders of magnitude stronger for $E \geq 100$ keV. This observation justifies in many scenarios the neglection of coherent scattering.

with the characteristic energy dependency of the photoelectric effect $f_{\mathrm{Ph}}(E) = \frac{1}{E^{3.2}}$ while the Compton effect is described by the energy dependency $f_{\mathrm{KN}}(E) = \sigma^{\mathrm{KN}}$ of the Klein-Nishina cross-section. For the coefficients of the basis functions we get

$$\begin{aligned} a_{\mathrm{C}} &= N^{\mathrm{eff}}, \\ a_{\mathrm{Ph}} &= C_{\mathrm{Ph}} N^{\mathrm{eff}} (Z^{\mathrm{eff}})^{3.8}, \end{aligned} \tag{2.16}$$

with the effective electron density N^{eff} of the material or mixture and its effective atomic number Z^{eff}. C_{Ph} is a constant used to approximate the photoelectric cross-section [White1977].

2.2 Spectral basis functions

According to the equations presented in section 2.1 the superposition of several characteristic energy-dependent functions determines the x-ray attenuation of any material. Therefore, the energy-dependent

x-ray attenuation can be treated as M-dimensional vector space with the photoelectric effect, Compton and Rayleigh scattering and eventually k-edge jumps as vector basis:

$$\frac{\mu}{\rho}(E) = \sum_{\alpha=1}^{M} a_\alpha f_\alpha(E), \tag{2.17}$$

where the index α identifies each interaction mechanism to be considered. The characteristic energy dependencies $f_\alpha(E)$ are called the spectral basis functions. For a two-dimensional (2D) basis under the assumption that each material can be approximated by photoelectric absorption and Compton scattering (cf. equation 2.15), Lehmann et al. have shown that the attenuation of any arbitrary material can be written in terms of a linear combination of two other 'reference' materials a and b [Lehmann1981]:

$$\frac{\mu}{\rho}(E) = c_a \frac{\mu_a}{\rho_a}(E) + c_b \frac{\mu_b}{\rho_b}(E). \tag{2.18}$$

The transition from equation 2.17 to equation 2.18 can be understood as basis transformation in terms of vector algebra and is visualized in figure 2.2: The characteristic energy-dependency of photoelectric effect and Compton scattering are linearly independent and therefore any two linear combinations of these functions is itself a new basis for the vector space.

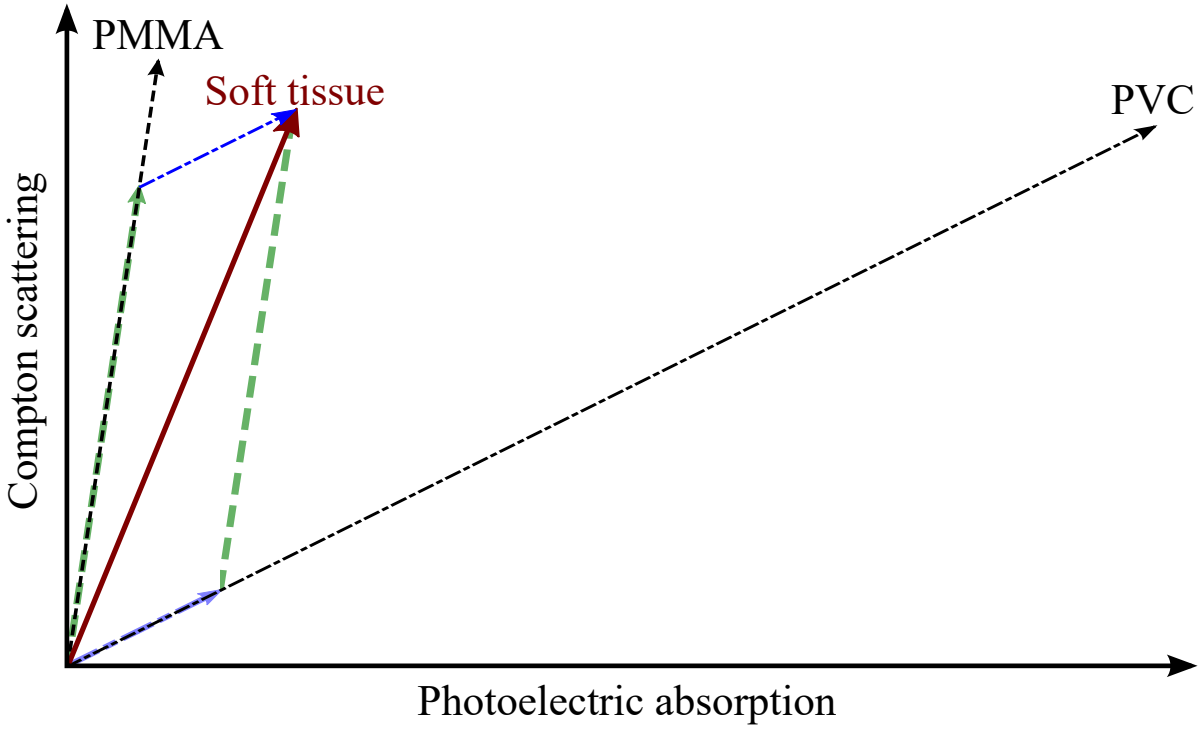

Figure 2.2: **Visualization of the spectral basis material transformation.** A material, e. g. soft-tissue is characterized by the unique contributions of photoelectric absorption and Compton scattering. Therefore, these two effects span the vector space of x-ray attenuation. The same holds true for any other two materials in the vector space, e. g. the polymers PMMA and PVC. According to a transformation of basis functions, the attenuation of soft-tissue can be expressed by a suitable linear combination of other materials which then constitute a new vector basis.

2.3 Spectral forward-models and MLE of basis material line-integrals

The basic measurement process in x-ray imaging yields the so called line-integrals of the attenuation $\mu_{\mathrm{L}}(E)$ of the object's mass attenuation coefficient. If the mass attenuation coefficient is 3D distributed within the object dependent on the location vector $\boldsymbol{r}$, then

$$\mu_{\mathrm{L}}(E) = \int_{\boldsymbol{S}} \frac{\mu}{\rho}(E, \boldsymbol{r})\rho(\boldsymbol{r}) \cdot \mathrm{d}\boldsymbol{s}, \tag{2.19}$$

where $\boldsymbol{S}$ describes the path of the x-ray beam through the object. In the notation of the spectral basis functions (equation 2.15) the attenuation line-integral can be expressed as

$$\begin{aligned} \mu_{\mathrm{L}}(E) &= \sum_{\alpha} A_\alpha f_\alpha(E), \\ A_\alpha &= \int_{\boldsymbol{S}} a_\alpha(\boldsymbol{r})\rho(\boldsymbol{r}) \cdot \mathrm{d}\boldsymbol{s}, \end{aligned} \tag{2.20}$$

where A_α is the line-integral of material α and $f_\alpha(E)$ is the unique energy-dependency of the basis material.

For the most basic case in spectral x-ray imaging we consider the measurement of an object composed of a number M of materials at $N \geq M$ discrete monochromatic energies $E_1 \cdots E_N$. The obtained set of images can be expressed by the vector

$$\begin{pmatrix} \mu(E_1) \\ \vdots \\ \mu(E_N) \end{pmatrix} = \underbrace{\begin{pmatrix} f_1(E_1) & \cdots & f_M(E_1) \\ \vdots & \ddots & \vdots \\ f_1(E_N) & \cdots & f_M(E_N) \end{pmatrix}}_{\boldsymbol{B}} \begin{pmatrix} A_1 \\ \vdots \\ A_M \end{pmatrix}, \tag{2.21}$$

with the $N \times M$ spectral basis function matrix $\boldsymbol{B}$. The process of retrieving the basis material line-integrals from the measured spectral attenuation data is called material decomposition. In this simple case and when $N = M$ the material decomposition can be obtained analytically by solving the above set of equations:

$$\begin{pmatrix} A_1 \\ \vdots \\ A_M \end{pmatrix} = \boldsymbol{B}^{-1} \begin{pmatrix} \mu(E_1) \\ \vdots \\ \mu(E_N) \end{pmatrix}. \tag{2.22}$$

In the more general case of imaging using a polychromatic (tube-)spectrum, a so-called spectral forward-model F_i relates the basis material line-integrals to the registered image intensity $\mathcal{C}_i$ in several bins i of the continuous energy spectrum (e. g. the number of photons registered by a PCD):

$$\mathcal{C}_i = F_i(A_\alpha). \tag{2.23}$$

A very general and exact spectral forward-model was stated by Roessl et al. [Roessl2007] implying detailed knowledge of properties of the x-ray source and the energy response of the used detector system. In this work the expected number of photon counts in each energy bin i of a PCD can be accurately calculated and will be called the ground-truth value $\mathcal{C}_i^{\mathrm{GT}}$:

$$\mathcal{C}_i^{\mathrm{GT}} = \int_0^\infty \Phi_{\mathrm{eff}}(E)\mathrm{e}^{-\sum_{\alpha=1}^{M} A_\alpha f_\alpha(E)} S_i(E)\mathrm{d}E, \;\; i = 1...N. \tag{2.24}$$

Here $\Phi_{\mathrm{eff}}(E)$ is the effective source spectrum comprising the emitted photon number spectrum and the sensor quantum efficiency. $S_i(E)$ describes the bin sensitivity function of the used detector for energy bin i. $S_i(E)$ accounts for the specific detector type used and contains effects that may lead to overlapping energy bins. For a PCD the most important factors that contribute to $S_i(E)$ will be discussed in the sections 3.3 and 5.1. Exact knowledge of the system parameters $\Phi_{\mathrm{eff}}(E)$ and $S_i(E)$ enable the direct decomposition of registered images into basis materials. This was, for example, demonstrated by the use of a MLE [Roessl2007, Schlomka2008] resulting in unbiased and efficient (i. e. minimum variance) estimates of the basis material line-integrals.

To circumvent the need for exact knowledge of all system parameters, empirical methods have been developed that rely on the measurement of well-known calibration phantoms to subsequently extract the basis material composition of samples. One particular method that models the object transmission using rational polynomials of varying degree has already been proposed at an early stage in the development of spectral x-ray imaging [Cardinal1990]. For example a rational polynomial of degree 2 yields in a two-material basis

$$\mathcal{C}_i^{\mathrm{RP}} = \frac{c_{i,0} + c_{i,1}A_\alpha + c_{i,2}A_\beta + c_{i,3}A_\alpha^2 + c_{i,4}A_\alpha A_\beta + c_{i,5}A_\beta^2}{c_{i,6} + c_{i,7}A_\alpha + c_{i,8}A_\beta}. \tag{2.25}$$

Models of the form 2.25 can be inverted numerically, for example by a least squares fit. Despite its success in decomposing into two basis materials in dual-energy applications and the relatively simple calibration which requires only a small number of measurements, the method tends to produce excessive noise when used with over-determined spectral data [Alvarez2011]. That is, when more energy bins are

present than basis materials, standard polynomial methods can not take into account the proper noise characteristics and therefore result in inaccurate estimations of the basis material line-integrals. In addition, the number of required terms in the polynomials and thereby the number of calibration coefficients rises very quickly for larger numbers of energy bins and basis materials. Hence, projection-based decomposition into more than two basis materials using polynomial approaches is hardly feasible in practice. For the use with multi-bin PCD systems, a two-step method based on a MLE of linearised counting numbers followed by the correction of the initial decomposition using a lookup table was implemented [Alvarez2011]. This so-called A-table method has the advantage that the estimator is computationally fast as well as unbiased and efficient for any number of energy bins. However, appropriate sampling of the involved lookup table also needs an excessive amount of calibration measurements.

If the number of available PCD energy bins is equal to or greater than the dimensionality of the attenuation basis, $N \geq M$, a suitable parameter estimation method has to be employed in order to decompose into the basis materials. Due to its unbiasedness and efficiency [Kay1993], a MLE method was chosen for the processing of the PCD data. Since there is a lot of literature available on the application of MLE to spectral x-ray imaging [Roessl2007, Schlomka2008, Alvarez2011] , only the most basic features will be described here.

Let c_i denote the counts measured in energy bin i during an actual imaging experiment. This value is a Poisson random number due to the statistical nature of x-ray emission and detection. Therefore, one calculates the total probability $\mathcal{P}$ for a measurement to yield a set of count values c_i. Assuming an object characterized by a set of basis materials A_α, this probability evaluates as

$$\mathcal{P}(c_1, ..., c_N, A_\alpha) = \prod_{i=1}^{N} \frac{\mathcal{C}_i(A_\alpha)^{c_\mathrm{i}}}{c_\mathrm{i}!} \mathrm{e}^{-\mathcal{C}_i(A_\alpha)}, \alpha = 1...M. \tag{2.26}$$

The task is now to find parameters A_α that maximize $\mathcal{P}$ under a given set of c_i. This is analogous to minimizing the negative logarithm of $\mathcal{P}$ (NLL). Calculating the NLL and neglecting terms that are independent of A_α one obtains a cost function $\mathcal{L}$ for the MLE:

$$\mathcal{L}(c_1, ..., c_N, A_\alpha) = \sum_{i=1}^{N} \left(\mathcal{C}_i(A_\alpha) - c_i \ln \mathcal{C}_i(A_\alpha)\right), \alpha = 1...M. \tag{2.27}$$

The maximum-likelihood estimate of A_α will be called A_ML and can now be stated as

$$A_{\mathrm{ML}} = \arg\min_{A_\alpha} \mathcal{L}(c_1, ..., c_N, A_\alpha). \tag{2.28}$$

Material decomposition can in general be done in the projection domain working directly on line-integrals as well as in the reconstructed image space working on individual voxels. For systems with separate acquisition of energy channels like dual-source concepts, the latter concept has to be applied since projections are never registered to one another. However there are some issues associated with image space decomposition. As mentioned already, registration of volumes with respect to each other has to be performed prior to decomposition. E. g. in clinical scans this becomes necessary due to patient movement during acquisition. Voxel values in the reconstructions are in general already subject to artifacts like beam-hardening. Therefore, the obtained images have to be corrected for such artifacts prior to material decomposition. Furthermore, reconstruction techniques and correction algorithms might alter the noise statistic in the images. Therefore, correlations in the basis material images might not be exploited in subsequent postprocessing of basis material images which is also true for imperfections in image registration.
Working in the projection space in turn offers the possibility to handle beam-hardening effects a priory with no need to perform additional corrections. The resulting basis material line-integrals are independent of energy and the full statistical information is preserved and available to subsequent analysis. As energy-selective projections are acquired simultaneously by PCDs there is no need for image registrations. Therefore, projection-based material decomposition will be considered in the remainder of this work.

2.4 Noise considerations in spectral x-ray imaging

The emission and detection of photons is a stochastic process. Therefore, noise is present in each x-ray image recorded by a detector. For an ideal photon-counting image, the behavior of noise follows a Poisson distribution. During the material decomposition this noise will propagate into the estimates of the basis materials. Two major considerations apply to the statistical noise in basis material images namely the correlation of noise between basis material images and a general boundary for the noise level in the images.

Anti-correlated basis material noise

Assuming uncorrelated measurements in each of the PCD energy bins, one can apply a general form of error propagation [James2000, Roessl2007a]. Let the matrix $\boldsymbol{\mathcal{J}}$ be the Jacobian of the employed spectral forward-model, i. e. $\boldsymbol{\mathcal{J}}_{ij} = \partial \mathcal{C}_i / \partial A_j$. In a two-material attenuation basis the covariance matrix $\boldsymbol{V}_A$ of the obtained basis material estimates can formally be calculated as

$$\boldsymbol{V}_A = \boldsymbol{\mathcal{J}}^{-1} \underbrace{\begin{pmatrix} \sigma_1^2 & 0 \\ 0 & \sigma_2^2 \end{pmatrix}}_{\boldsymbol{P}} (\boldsymbol{\mathcal{J}}^{-1})^{\mathrm{T}}, \tag{2.29}$$

where the matrix $\boldsymbol{P}$ contains the statistical noise present in the measurements of photon count numbers. Since we assumed uncorrelated energy bins the off-diagonal terms in $\boldsymbol{P}$ vanish. After carrying out the matrix multiplication in equation 2.29 the off-diagonal terms in $\boldsymbol{V}_A$ (i. e. the covariance $\sigma_{A_1 A_2}$ of the basis material estimates) become finite since all $\boldsymbol{\mathcal{J}}_{ij} \neq 0$. A rigorous calculation [Roessl2007a, Kalender1988] further yields that the covariance

$$\mathrm{cov}(A_1 | A_2) = \sigma_{A_1 A_2} \overset{!}{<} 0. \tag{2.30}$$

This means that the estimates for both basis materials are anti-correlated. An over-estimation of one basis material line-integral will result in an under-estimation of the other.

The Cramér-Rao lower bound for the estimator

We first consider the general case of measuring random variables X that depend on a N-dimensional vector $\boldsymbol{\theta} = (\theta_1, \theta_2, \ldots, \theta_{\mathrm{N}})^{\mathrm{T}}$ of parameters. The probability density function $\mathcal{P}(X, \boldsymbol{\theta})$ describes the probability that a specific parameter vector yields the observed set X. A measure for the amount of statistical information contained in this experiment is given by the so-called Fisher information matrix $\boldsymbol{\mathcal{F}}$ [Kay1993] with $N \times N$ elements:

$$\boldsymbol{\mathcal{F}}_{ij} = \left\langle \frac{\partial \ln \mathcal{P}(X, \boldsymbol{\theta})}{\partial \theta_i} \frac{\partial \ln \mathcal{P}(X, \boldsymbol{\theta})}{\partial \theta_j} \right\rangle_{\theta}, \tag{2.31}$$

where $\langle \ldots \rangle_\theta$ denotes the expectation value with respect to the parameters $\boldsymbol{\theta}$.

In the case of spectral x-ray imaging X corresponds to the vector $\boldsymbol{c} = (c_1,\, c_2,\, \ldots, c_\mathrm{N})^\mathrm{T}$ of counts recorded in each energy bin, the parameter vector is given by $\boldsymbol{A} = (A_1,\, A_2,\, \ldots, A_\mathrm{M})^\mathrm{T}$ as defined by equation 2.20 and the probability density function can be replaced by the negative log-likelihood (NLL), $\mathcal{P} \rightarrow \mathcal{L}(c_i,\, A_\alpha)$. The counts recorded by a PCD are Poisson distributed with $\langle c_i \rangle = \mathrm{var}[c_i] = \mathcal{C}_i^\mathrm{GT}$. Under these conditions a special expression for the now $M \times M$ Fisher matrix elements has already been deduced very early in the history of spectral x-ray imaging [Alvarez1976, Roessl2009]:

$$\boldsymbol{\mathcal{F}}_{\alpha\beta} = \sum_{i=1}^{N} \frac{1}{\mathcal{C}_i(\boldsymbol{A})} \frac{\partial \mathcal{C}_i(\boldsymbol{A})}{\partial A_\alpha} \frac{\partial \mathcal{C}_i(\boldsymbol{A})}{\partial A_\beta}. \tag{2.32}$$

As discussed under section 2.3 the basis material line-integrals $\boldsymbol{A}$ must be inferred from the measured counts by means of a suitable parameter estimation method, e. g. MLE. In case of an unbiased estimator for the vector $\boldsymbol{A}$, the so-called Cramér-Rao lower bound (CRLB) gives the lower limit for the variance that is propagated from the measurements into the estimates related to the Fisher information matrix [Kay1993]. Hence it can be used to determine the minimum variance $\sigma^2_{A_\mathrm{ML}}$ of the estimates A_ML. In the context of the cost function $\mathcal{L}$ from equation 2.27 with Poisson-distributed counting data, the CRLB yields [Roessl2009]

$$\sigma^2_{A_{\alpha,\,\mathrm{ML}}} \geq (\boldsymbol{\mathcal{F}}^{-1})_{\alpha\alpha}. \tag{2.33}$$

Note that the actually obtained variance in the basis materials depends on the data processing scheme that is implemented and may result in larger variance than predicted by the CRLB. Specific estimators that achieve the CRLB are called efficient.
A very important application of the CRLB is the optimization of acquisition parameters for a specific measurement. Examples thereof will be investigated in section 5.2.

3 Photon-counting detector technology

Photon-counting detector technology is becoming increasingly attractive for spectral x-ray imaging applications [Taguchi2013, Ballabriga2016]. The ability to acquire multiple energy-selective images in a single shot and other benefits associated with individual processing of single photons offer many advantages for material-selective imaging at reduced exposure levels and acquisition time. Therefore, a major part of this thesis focuses on applications of such detectors to x-ray imaging techniques. This chapter will provide the necessary technical background on the design and operation principles of PCDs and discuss the unique features and limitations of these devices.

3.1 Classification of x-ray detectors

The purpose of every x-ray detector system used for imaging is the detection, quantification and digitization of the amount of radiation that is impinging on the detector at any given time interval. Therefore, each detector must provide two more or less individual features:

- A radiation sensor that directly interacts with the x-rays, converting them into electrical signals and
- Electronics to process theses signals and create digital images.

These two parts can be used to classify the various x-ray detector systems according to way the incoming photons are registered and processed [Knoll2010].

Indirect vs. direct conversion of x-rays

Radiation sensors can be distinguished by the way they facilitate the conversion from x-ray photons to electrical signals. In that sense two major principles need to be distinguished:

- **Indirect conversion:** In this conversion scheme, the x-rays are first converted to visible light in a scintillator crystal. These low-energy photons are subsequently converted to electrical signals, often accomplished by Si photo-diodes. Typical materials for indirect conversion include ZnSe:Te, Gd_2O_2S:Pr (Gadox, GOS), $CdWO_4$ and CsI:Ti [Shefer2013] where a fast conversion from x-rays to visible light is a crucial parameter for their use in CT. Since many of these crystals contain significant amounts of high-Z elements their x-ray efficiency is usually relatively high. While the wavelength of the emitted visible photons depends on the used material, the intensity is proportional to the energy of the impinging x-ray photon.

- **Direct conversion:** In this detection mechanism, x-ray photons are directly converted into electrical signals by photoelectric absorption in a depleted semiconductor diode by the creation of electron-hole pairs. Therefore, the electrical charge created per x-ray photon is usually much higher after direct conversion and is proportional to the energy of the registered x-rays. Often used semiconductors are Si, amorphous Se, GaAs, and CdTe/CZT (cf. section 3.2.1 where the last one is of particular importance in clinical imaging due to its high efficiency.

Energy-integrating detectors vs. single-pulse processing

The second major difference between detection systems is found in the way that the individual electrical signals obtained from single events are handled by the readout electronics.

- **Energy-integrating detectors (EIDs):** The electric charge generated by all impinging photons is integrated over a defined time period (integration time T_i) in a storage capacitor. Afterwards, the current from discharging the capacitor is measured and digitized. Such detectors can intrinsically handle an almost arbitrarily high photon flux. This integration process causes the contribution of each photon in polychromatic beams to be weighted with its original energy. Therefore, the output signal of EIDs is proportional to the radiation dose deposited in the sensor material.

- **Single-pulse processing:** The signal pulse generated by each x-ray photon is processed individually and independent from the others. In some sense, this process can be understood by taking

$\lim_{T_i \to 0}$ in EIDs. Thereby, the current after discharging the capacitor is still proportional to the x-ray energy. However, signals are typically very small and require further signal processing (cf. section 3.2.2). Thereby, a discrimination of x-rays on the basis of their energy becomes feasible.

3.1.1 Overview of different detector types

Until today, a large variety of x-ray detectors have been developed for imaging applications. This paragraph will provide a short list of the most widely used detectors with respect to the classification offered above.

- **Charge-coupled devices (CCDs):** These detectors are EIDs and utilize mostly indirectly conversive sensors. Each pixel consists of a photodiode and switchable electrode structures. Since not every pixel has its own readout circuit, shift registers are used. The charge is shifted sequentially to the end of a pixel row and read out serially. A long readout time is the result [Smith2009]. Due to the simplicity of the readout electronics the production costs are comparable low. Furthermore, the simple structure allows for very small pixel sizes in the order of a few µm and below.

- **Computed radiography (CR) detectors based on storage phosphors[1]:** CR systems were one of the first digital x-ray imaging detectors available. They use an indirect conversion scheme by first storing the absorbed x-ray energy in crystal defects in a metastable state. During readout, the imaging plate is illuminated by a laser beam causing the stored energy to be emitted as visible photons [Rowlands2002, Leblans2011]. Therefore, such detectors always are EIDs and have a very long readout time in the order of several 10 s.

- **Flat-panel detectors (FPDs):** The energy integrating FPDs are currently the most widely used detector type in radiography and cone-beam CT [Cowen2008]. Most FPDs are equipped with indirectly conversive scintillators, however amorphous Se is used for direct conversion in some models. The charge signal is read out by a thin film transistor. Therefore, FPDs can be produced with large detector areas, as the manufacturing process is similar to display-panel production, leading also to comparatively low production costs per pixel. Read out times are relatively slow[2] and high dark current and gain non-linearities can limit image quality and need special consideration [Wischmann2002, Willis2011].

[1] The term ‘phosphor´ here does not imply that the actual chemical element P is used. It rather serves as a collective term for compounds which exhibit phosphorescence.

[2] Frame-rates of a few 10 fps can be realized

- **Hybrid-pixel photon-counting detectors (PCDs):** This detector system belongs to the class of direct and single-pulse processing detectors [Taguchi2013, Ballabriga2016]. Pulse processing and readout circuits are strictly separated from the sensor layer, where the conversion from x-rays to electric signals takes place. This allows an individual optimization of the sensor layer and readout electronics. The design of the readout electronics is derived from CMOS technology. Advantages are a high read out speed of more than $1000\,\mathrm{fps}$, spectral resolution, a high dynamic range and the possibility to suppress dark current. The concept of these detectors will be presented in more detail throughout the following sections.

3.2 Design of photon-counting detectors

The technology of hybrid-pixel PCDs dates back to the late 1980's where they have been developed at CERN for tracking detector systems in particle collider experiments. The first hybrid pixel detector was tested in the *OMEGA* spectrometer in the CERN heavy ion experiment in 1991 [Anghinolfi1992, Anghinolfi1992a]. A few modifications of the readout application-specific integrated circuit (ASIC) allowed the use of this technology for X-ray imaging [Ballabriga2016]. PCDs are attractive for x-ray imaging because they make use of direct conversion of the x-ray photons to an electric signal, which provides a significant higher amount of charge per photon compared to indirect conversion mechanisms. Furthermore, the single event handling allows to weight all photons equally. Also it enables to introduce energy discrimination which allows for data acquisition without dark current and electronic noise. The implementation of energy thresholds also allows to acquire energy selective images. The hybridization between readout circuit and semiconductor layer offers the choice to fit the detector with a suitable sensor material for a given application.

Figure 3.1 shows the general structure of a hybrid-pixel PCD. The conversion from x-rays to electric signals is facilitated by the diode-structures in the sensor layer. Processing of the charge pulses, energy discrimination and analog-to-digital conversion is performed by the readout ASIC. In contrast to CCDs or standard FPDs each single pixel has its own chain of active electronics to amplify and shape the incoming signals in order to improve the SNR. A very general block diagram of such a pulse processing chain is also illustrated in figure 3.1.

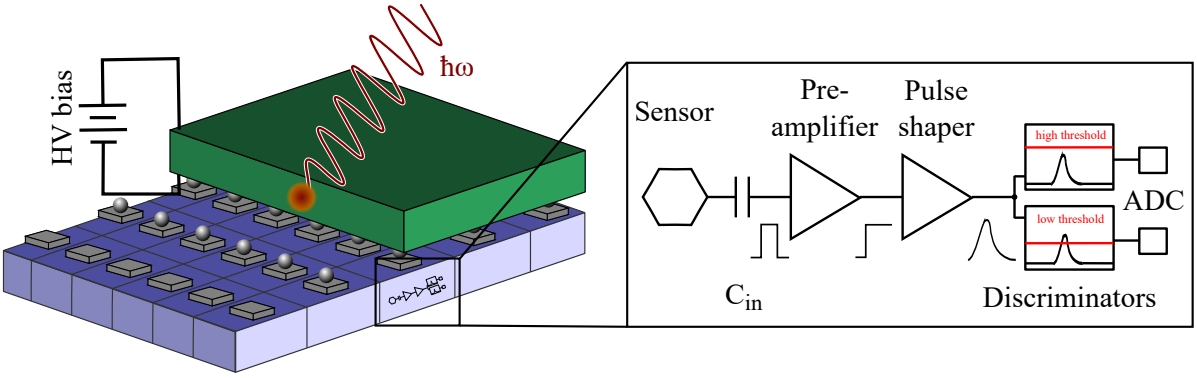

Figure 3.1: **Schematic representation of a PCD.** The detection system consist of two major parts, a semiconductor sensor and a readout ASIC which are connected via a bump-bonding process. Electric signals are generated in the sensor directly by absorption of x-rays and subsequent creation of electron-hole pairs that are separated and accelerated towards the sensor electrodes in an electric field caused by the HV bias. The readout ASIC contains electronics for pulse processing and energy discrimination of each single event and stores the registered number of photons in a counter after analog-to-digital conversion.

3.2.1 Directly-conversive semiconductor sensors

This section will provide a short introduction to the basic properties and mechanisms of semiconductor x-ray sensors. A more detailed treatment of these devices is e. g. given in [Spieler2005]. The sensors used in PCDs are in principle a 2D array of semiconductor diodes. Hereby n- or p-type regions are periodically implanted into a monolithic bulk material of opposite doping. The resulting sensor is sensitive to incoming x-rays over its entire surface area. Via a metal contact layer, the sensor is connected to a high voltage bias U_b in reverse direction, causing full depletion of the diode structure from intrinsic charge carriers. Figure 3.2 shows the simplified structure of a p-in-n silicon sensor. A metal bond-pad allows the connection of the sensor to the readout system via solder bump-bonds.

When an x-ray photon is absorbed in the sensor layer of thickness d, a charge cloud consisting of electrons and holes is created. Thereby, the total amount of charge Q is determined by the ionization energy E_i which is proportional to but greater than the band gap of the semiconductor [Spieler2005]:

$$q = \frac{E_\mathrm{x}}{E_\mathrm{i}}, \tag{3.1}$$

where E_x is the energy of the absorbed x-ray photon. Therefore, the amount of charge created is also

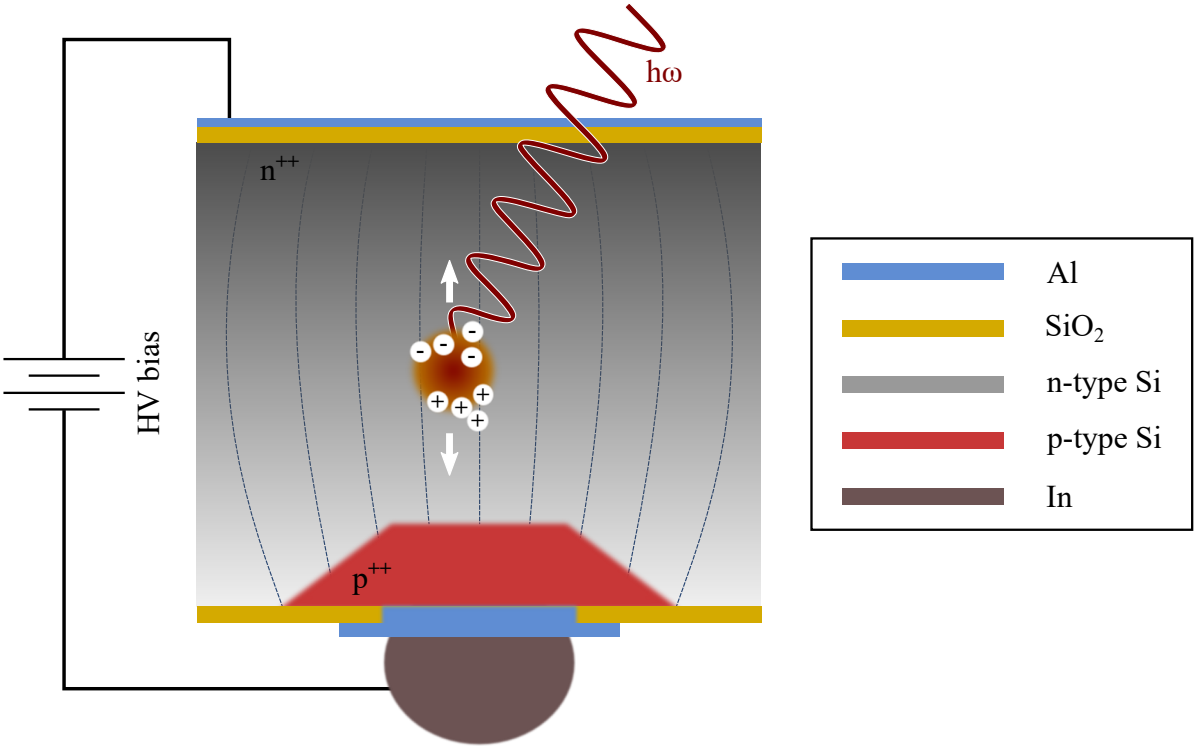

Figure 3.2: **Schematic representation of a semiconductor sensor.** In this drawing, a p-in-n Si sensor is shown, however the generals structure of the sensors is the same for all used materials. Incoming x-rays are absorbed in the bulk material and create a charge cloud of electrons and hols proportional to the energy of the absorbed photon. The charges are separated and transported to the electrodes in the externally applied electric field from the HV bias.

proportional to the energy of the photons.

Subsequently the charge carries drift towards the electrodes under the influence of the electric field $\vec{E}$, $|\vec{E}| = U_\mathrm{b}/d$. The current density $\vec{J}$ induced in this way depends not only on the amount of charge, but also on the individual mobility $\mu_{\mathrm{n,\,p}}$ of electrons and holes since the drift velocity v_D is determined by the mobility:

$$\vec{J} = q(nv_{\mathrm{D,\,n}} + pv_{\mathrm{D,\,p}}) = (n\mu_\mathrm{n} + p\mu_\mathrm{p})q\vec{E}, \tag{3.2}$$

where n and p are the volume densities of the charge carriers. Typically the mobility of the charge carriers is different for electrons and holes in a given semiconductor. This very often determines the sensor structure (p-in-n vs. n-in-p) since it is desirable to collect the charge carriers with the larger

mobility at the readout electrode [Ballabriga2016]. From equation 3.2 the nominal charge collection time t_{C} can be derived:

$$t_{\mathrm{C}} \simeq \frac{d}{v_{\mathrm{D}}} = \frac{d^2}{\mu U_{\mathrm{b}}}. \tag{3.3}$$

This defines the minimum amount of time required for the shaping of a single pulse such that the complete input signal is collected and processed by the readout electronics. The loss of signal amplitude for shorter collection times is referred to as ballistic deficit and can degrade the energy resolution of the detection system.

At the same time that the charge carriers drift towards the electrodes, lateral diffusion of the carriers takes place. Assuming a gaussian charge profile, the broadening σ of the initial charge cloud during the collection time t_{C} in equation 3.3 can be obtained by using the Einstein relations of the diffusion coefficient D and the carrier mobility [Ballabriga2009]:

$$\sigma = \sqrt{2Dt_{\mathrm{C}}} = \sqrt{2\frac{kT}{e}\frac{d^2}{U_{\mathrm{b}}}}, \tag{3.4}$$

where k is the Boltzmann constant, T is the temperature and e the elemental charge.

As discussed in section 2.1, the x-ray absorption characteristics of a material depend strongly on its atomic number Z. For a complete deposition of the x-ray energy within a small volume it is desirable that the x-rays interact with the sensor primarily via the photoelectric effect and therefore larger Z values are beneficial. One can define the energy-dependent fraction $\mathrm{Q}(E)$ of photons absorbed by a sensor as

$$\mathrm{Q}(E) = 1 - e^{-\mu_{\mathrm{S}}(E)d_{\mathrm{S}}}, \tag{3.5}$$

where $\mu_{\mathrm{S}}(E)$ and d_{S} are the sensor's absorption coefficient and thickness. $Q(E)$ is also called the sensor's quantum efficiency.

Figure 3.3 summarizes the important material constants for various semiconductors that are frequently used for PCD sensors. Comparing the quantum efficiencies for Si, GaAs and CdTe one can see that

Properties of different semiconductors

Semiconductor	Si	GaAs	CdTe
Atomic number Z	14	31, 33	48, 52
Band-gap at 300 K / eV	1.12	1.42	1.56
Ionization energy E_i / $\frac{\mathrm{eV}}{\mathrm{pair}}$	3.61	4.26	4.43
Electron mobility / $10^3 \frac{\mathrm{cm}^2}{\mathrm{Vs}}$	1.4	8.5	1.1
Hole mobility / $10^3 \frac{\mathrm{cm}^2}{\mathrm{Vs}}$	0.45	0.4	0.1

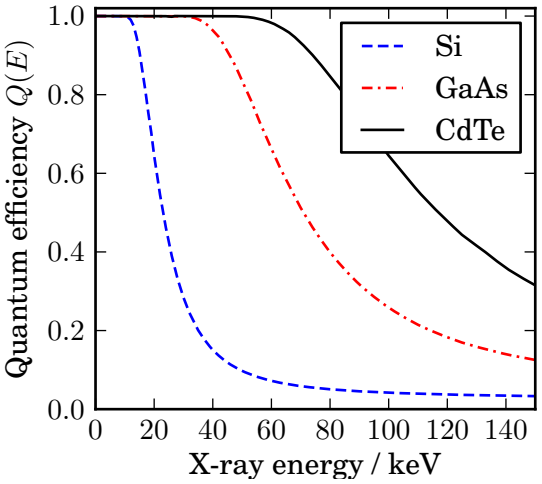

Figure 3.3: **Properties of different semiconductors used as PCD sensors.** The table lists frequently used materials and summarizes their most important material parameters. The plot compares the absorption efficiency of 1 mm thick sensors using Si, GaAs and CdTe calculated using equation 3.5.

primarily for medical applications, where an almost complete usage of the x-ray dose delivered to the patient is crucial, high-Z semiconductors like CdTe are essential. For CT applications, thicknesses of $2 - 3$ mm are typically required. Therefore, a lot of effort was put into the development of high-purity materials covering larger ares suitable for sensor applications during the recent years [DelSordo2009, Ruat2014, Prokesch2016] and the availability of CdTe/CZT detectors with thickness of more than 1 mm is increasing.

3.2.2 Photon-counting readout electronics

The most important part setting apart a PCD from an integrating detector like a flat-panel detector is the readout ASIC. In this section we will have a closer look on the design and functionality of the pulse processing electronics that are employed in PCDs.

Besides some common blocks like voltage and current references and readout lines, each pixel in the detector array has its own active signal processing chain consisting of amplifiers, signal shaper, discriminators and digital elements. Since the physical size of a pixel is usually small in the order of $50 - 300\,\mu$m, the processing chain and the digital electronics are implemented in a sub-micrometer CMOS process [Broennimann2009a]. Figure 3.4 gives an overview of the basic structure found in each pixel separated into an analog part and a digital part.

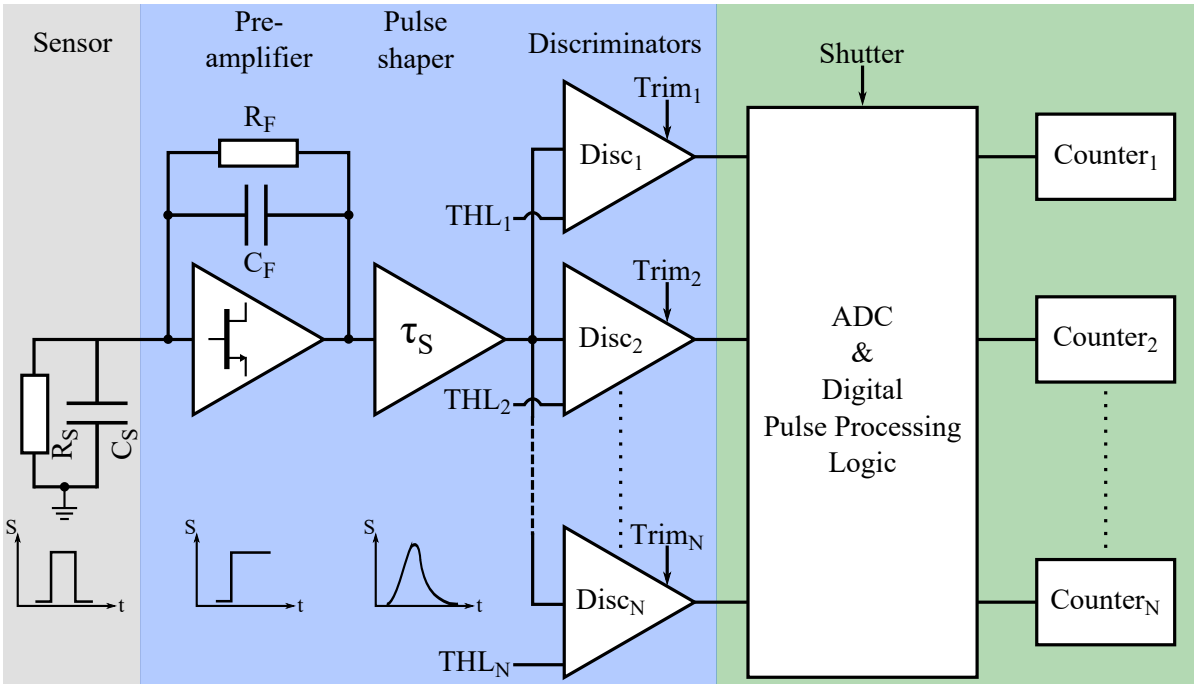

Figure 3.4: **Block diagram of a PCD readout ASIC.** The electronics can be grouped into an analog part (blue area) and a digital part (green area). Charge signals coming from the sensor are amplified and shaped in order to increase the SNR of each event and to prepare them for energy discrimination in an array of several discriminators. The output of the discriminators is passed to a digital pulse processing logic and finally the registers in the counters are increased where appropriate. Sketches of the signal waveforms after each stage are shown below the blocks.

Three major components can be found in the analog front-end: A pre-amplifier, pulse shaper and energy discriminators:

- **Pre-amplifier:**

  Under typical operating conditions in x-ray imaging, the electric charge deposited in the sensor is very small. According to equation 3.1 a 50 keV photon will result roughly in a charge of merely 1.8 fC. Thus amplification is necessary before further processing can be applied to the pulses. The pre-amplifier can be seen as operation amplifier configured with an integrating feedback loop. An incoming current pulse is amplified and transformed to a step impulse with a long decay time. The amount of amplification (i. e. the amplifier gain) is determined mainly by the feedback capacitance C_F and is inversely proportional to C_F. Many PCDs offer a switchable feedback capacitance to adjust the gain to specific needs of the sensor material and the used energy range.

The amplitude of the signal after the pre-amp should be directly proportional to the energy of the incoming photon. For very high photon energies or high amplifier gains, non-linearities of the output and saturation effects of the signal might occur that limit the energy resolution.

- **Pulse shaper:**

After amplification, the signal pulse is transformed by the pulse shaper. Its main purpose is to increase the Signal-to-Noise ratio of the detector system since the pre-amp also amplifies input noise. The signal pulse coming from the pre-amplifier is a function of time, but the signal power spectrum is also distributed in frequency space. The frequency spectra of the signal pulse induced by a photon event and noise components are in general different. Thus, a frequency response filter can be utilized to selectively amplify the signal and attenuate the noise. Since the filter changes the frequency response, the time dependency of the curve respectively its pulse shape is modified as well[3]. A typical shaper is configured as a CR high-pass and a RC low-pass filter. The high-pass filters works as differentiator that introduces the wanted decay time to the step impulse. Its bandwidth is limited by the subsequent integrating low-pass filter which also determines the rise time τ_s of the resulting pulse. The simplified shaper output signal can be described by the function [Spieler2005]

$$V(t) = V_0 \left(\frac{t}{\tau_\mathrm{s}}\right) \mathrm{e}^{-t/\tau_\mathrm{S}}. \tag{3.6}$$

Typical values for τ_s in PCDs are in the range of a few $100\,\mathrm{ns}$. The amount of electronic noise that is still present in the signal after the shaper output depends on the feedback capacitance C_F and the shaping time τ_s. Thereby high values of C_F, i. e. small gain and short peaking times τ_s increase the electronic noise floor. The amount of electronic noise determines the energy resolution achievable via energy discrimination.

- **Energy discriminators:**

The discriminators are the interfaces between the analog and digital side of the signal processing. The discriminator detects zero-crossings of the incoming signal and emits a digital pulse when the falling flank of the signal drops below zero. By using global offset threshold signals $\mathrm{THL}_{1\ldots N}$ which a re subtracted from the input signals energy discrimination is enabled. Therefore, a discriminator detects any signal with a higher amplitude than the threshold or in terms of photon energy

[3] Therefore the name pulse-shaper

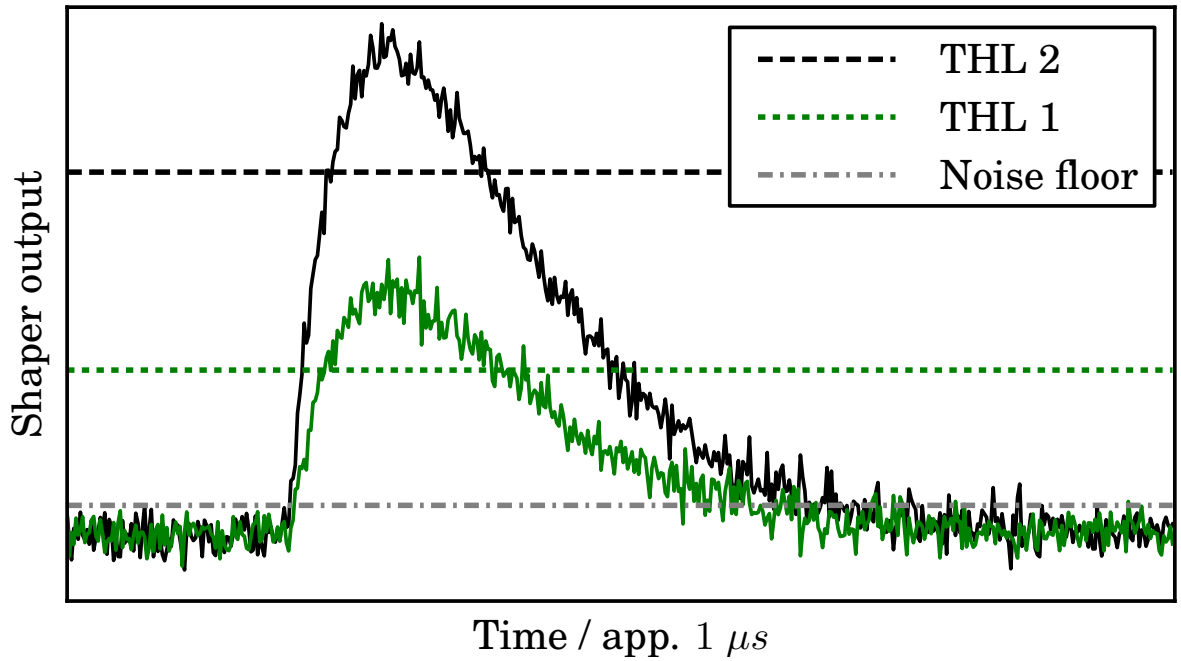

Figure 3.5: **Shaper output and energy discrimination in PCDs.** The curves show two typical shaper output signals according to equation 3.6 belonging to photons of different energy. When the signal amplitude exceeds the value defined by the threshold signals, the discriminators increase the associated counter registers. Electronic noise imposed on the shaper output limits the energy resolution of discriminable photons. By setting the thresholds above the noise floor, the influence of electronic noise in form of dark current can be effectively eliminated from the images.

, it detects any photons with a energy higher than the energy associated with the discriminator threshold. A series of N parallel discriminators enables sorting of incident photons into N discrete energy bins. Although the input signals to the discriminators are proportional to the photon energy, the constant of proportionality differs from pixel to pixel. This effect has to be attributed to manufacturing tolerances of the analog components (resistors, capacitors, etc.) resulting in different gain and offset values. To compensate for this effect, a second offset signal $\mathrm{Trim}_{1\cdots N}$ is fed to the discriminators which is individual for each pixel. Therefore, the CNR in x-ray images is increased by reducing inter-pixel variations of the spectral response. In a dedicated calibration or 'trimming' process, the energy-to-threshold relation and the required trimming parameters are determined by measurements of well-known x-ray sources [Kraft2009a, Uher2011, Panta2014]. The processing of the shaper output is visualized in figure 3.5.

- **Analog-to-digital converters (ADC) and counters:**

The acquisition of x-ray images is controlled by the Digital part of the ASIC. As long the digital shutter signal is active, the ADC feeds clock signals to the counters when the associated discriminator is triggered. Each clock pulse increases the values stored in the registers and the number of photons with energy greater than the threshold is recorded. When the shutter signal becomes inactive, the values can be read out and the counters are reset. Additionally, inter-pixel communication is used in some PCDs to correct spectral artifacts on-chip and in real-time, cf. the next section.

3.3 Spectral distortion effects in photon-counting detectors

In an ideal PCD system each registered photon deposits all of its energy in a single pixel. However, several processes lead to spectral distortions as the total energy of a photon is separated between two or more individual pixels. Such cases like charge-sharing, scattering or fluorescence escape degrade both the spatial and spectral resolution of a PCD. Other effects like pulse pile-up only affects the spectral response and the registered count rate. A simple illustration of these effects in the sensor is provided by figure 3.6 together with the associated shaper output. The most important effects will be highlighted and discussed briefly.

- **Charge-sharing:**

  Lateral diffusion and Coulomb repulsion of the created charge cloud result in a broadening of the charge packet during drift towards the sensor electrodes. When the photon hits the sensor close to a pixel boundary, the total charge may spread over two or more neighboring pixels (figure 3.6 B). Thereby, each pixel registers a photon count with reduced energy. The spatial resolution is reduced due to an effective blurring and a positive correlation between photon counts in neighboring pixels is introduced. According to equation 3.4, the amount of charge sharing can be decreased by using a larger pixel area, thinner sensors and higher bias voltages. Charge-sharing is a continuous process resulting in a relatively flat background in the spectral response of the detector. By implementing a summing of the shaper output signals from neighbor pixels and hit detection by inter-pixel communication, some PCD readout ASICs can correct charge-sharing on-chip and in real-time [Ballabriga2011, Ullberg2013]. Hereby, the total charge gets attributed to a single pixel and the spatial resolution is increased by elimination of the cross-correlation. Implications of the improved spatial resolution after correction of charge-sharing are investigated in chapter 8.

- **Scattering and fluorescence emission:**

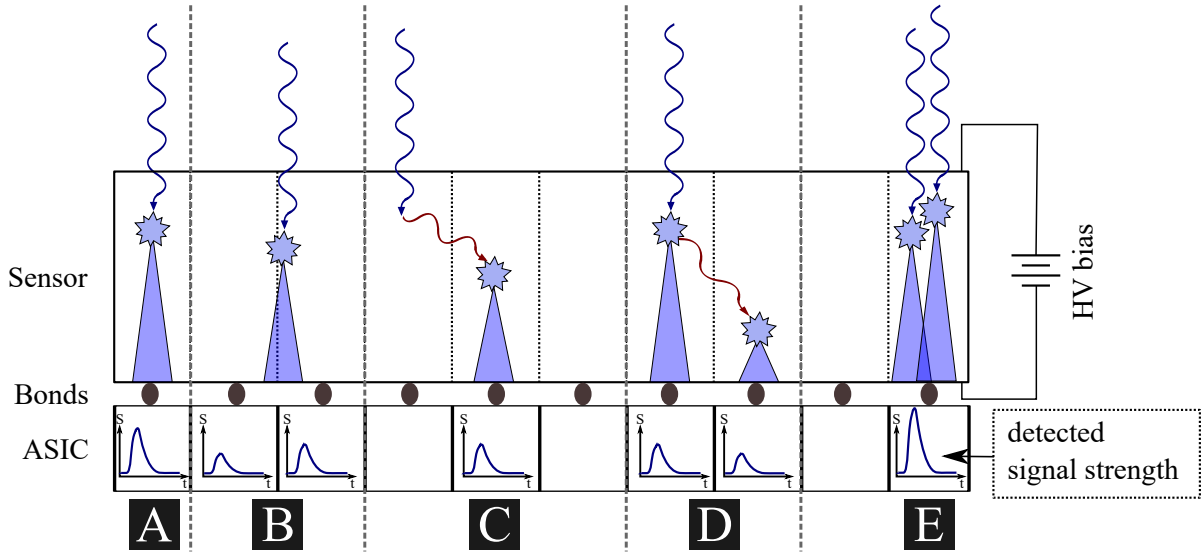

Figure 3.6: **Illustration of spectral distortion effects in PCD sensors.** Ideally a photon deposits all its energy in a single pixel (A). In real systems, different cases of spectral distortion need to be accounted for. Lateral spread of the drifting charge cloud may lead to charge-sharing effects between neighboring pixels (B) degrading both the spatial and spectral resolution of the PCD. Scattering in the sensor (C) and fluorescence escape (D) lead to similar effects. Signal pile-up occurs when two photons arrive very shortly after each other compared to the signal peaking time τ_s (E). This effect usually occurs in high-flux applications and leads to a drop of count rate and incorrect energy bin assignment of photons.

Ideally an absorbed photon should deposit its entire energy locally in the sensor via the photoelectric effect. However, there is a certain probability that incoming photons undergo scattering processes. In such cases, the scattered photons travel further in the sensor and may eventually reach a neighboring pixels before they are absorbed completely. Both coherent and incoherent scattering may occur (figure 3.6 C and D). The effects of Compton scattering on the obtained photon energy spectra consist of a continuous background extending from low energies to the so-called Compton edge [Knoll2010]. Another possibility is that a certain amount of the absorbed energy is re-emitted by means of x-ray fluorescence. Especially high-Z sensor materials are prone to emission of long range secondary fluoresce. For example in CdTe, the mean energy of fluorescence photons is approximately 25 keV resulting in a mean free path-length of $\approx 110\,\mu m$ [Ballabriga2016] which is enough to cover a distance of several pixels. The overall spectral distortions introduced by these processes are similar to those arising from charge-sharing and can be corrected to some extent by inter-pixel communication on the ASIC.

- **Pulse pile-up:**

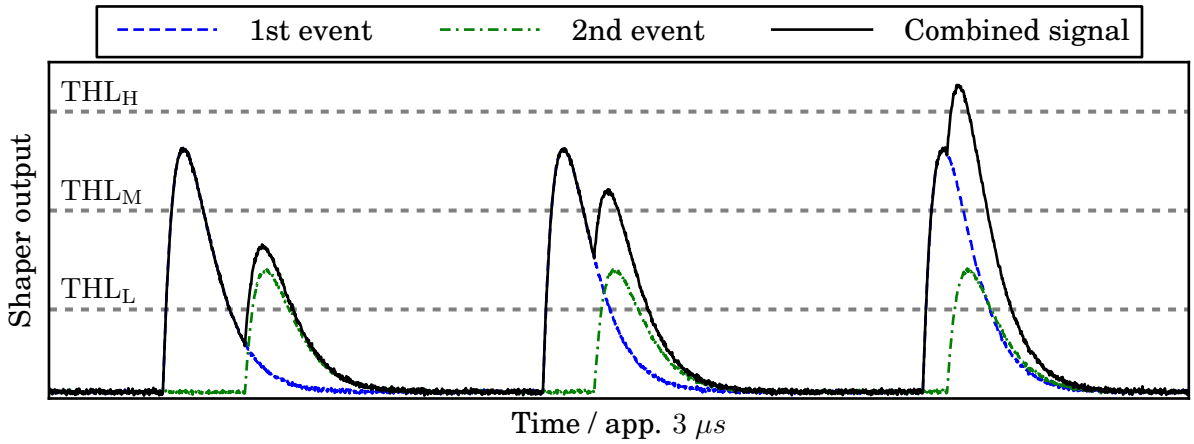

Figure 3.7: **Illustration of the pile-up effect in PCDs.** In the presented scenario, photons of two different energy are sorted into three different energy bins. In the leftmost case, the photons arrive with enough delay and the two events are well separated and registered in the correct energy bins. When the time between the arrivals decreases, a photon is lost in the lower energy bin and falsely registered in the middle bin. Further decreasing the time gap, the signals overlap such that the resulting shaper output corresponds to a single photon with strongly increased energy.

Due to the Poisson nature of x-ray emission, the arrival times of the photons at the sensor follow a stochastic distribution. Accordingly, there is a finite probability that two or more signals induced by consecutively arriving photons overlap in the processing chain (figure 3.6 E). This process is called pulse pile-up and results in significant spectral distortions when the x-ray flux increases and overlap becomes more likely. Possible pile-up scenarios are illustrated by figure 3.7.

Pile-up generally leads to losses in the registered total number of photon counts combined with spectral distortion due to an improper sorting of photon into the pre-defined energy bins. The probability of pile-up to occur increases with the photon flux and the shaping time τ_s. To reduce pile-up in high flux environments the shaping time constant could be reduced at ASIC design. This is however only feasible to some extent as a strong trade-off exists between a decrease of τ_s and increased electronic noise and ballistic deficit, both of which degrade the energy resolution. Based on the particular implementation of the pulse shaper and discriminator on the PCD ASIC, different analytical models can be employed to describe the count-rate losses due to pile-up [Knoll2010]. In the so-called non-paralyzable model signals from photons arriving within the processing time are simply ignored by the electronics and thus have no further effect on subsequent measurements. In contrast to this, the processing time in the paralyzable model is reset and therefore extended if a second photon arrives within the time required to process the first event. The observed count-rate R_{out} in many PCDs follows the paralyzable model which is described by the equation

$$R_{\mathrm{out}} = R_{\mathrm{in}} \mathrm{e}^{-R_{\mathrm{in}} \cdot \tau}. \tag{3.7}$$

Therefore, the observed count-rate has a maximum when the incident rate satisfies $R_{\mathrm{in}} = 1/\tau$ and drops towards zero for larger incident flux. In this context, τ is referred to as the dead-time and approximately $\tau \simeq \tau_{\mathrm{s}}$.

It can also be understood from figure 3.6 E that the probability for pile-up is a function of the detector energy threshold since the width of the peaks and therefore the dead-time increases at lower thresholds.

- **Sensor polarization:**

  The phenomenon of so-called sensor polarization results in a time-dependent decrease of the registered count rate and an associated shift of the spectral response. It is typically observed in high-Z semiconductor sensors where the concentration of defects is increased [Malm1974]. Trapping and de-trapping of charge carriers in the sensor leads to local distortions of the electric field induced by the bias voltage. Thereby the charge collection efficiency is decreased. It has been shown that a periodic reset of the bias voltage can reverse the effects of polarization [Bell1974, Seino2008]. This technique is also routinely implemented by some commercial PCD systems. It is conceived that CZT sensors are less sensitive to polarization than pure CdTe material [Prokesch2016].

In chapter 5 a model for several of the spectral distortions discussed here will be presented for simulation of PCD data.

4 Characterization of a state-of-the-art dual-energy spectral CT system

One major difference that sets apart spectral PCD-based CT from current dual-energy scanners is the fact that spectral data is acquired perfectly registered both in the temporal as well as in the spatial domain using PCDs. In contrast, most state-of-the-art dual-energy CT systems utilize interlaced acquisition for the low- and high-energy data. Often used concepts include dual-source systems [Flohr2006, Petersilka2008] and rapid kVp-switching between projections [Kalender1986, Hsieh2010, Zhang2011]. Typically, such systems suffer from problems related to incorrect registration of low- and high energy data, cross-scattering of photons from one energy bin to the other [Engel2008, Petersilka2010], potentially increased radiation dose and poor spectral separation [McCollough2015]. On the road to spectral scanners based on multi-bin photon-counting detectors, a new dual-energy CT scanner based on a dual-layer integrating detector was introduced recently. In this concept, the acquisition of dual-energy data is performed simultaneously by a single detector and therefore the data are always registered perfectly in the projection domain.

As discussed briefly in the introduction and chapter 2, projection-based material decomposition has physical and technical advantages over image-based methods leading to many medical applications [Graser2008, Chae2010, Pache2010, Bamberg2011, Yuan2012]. The aim of the study presented in this chapter is to evaluate the quantitative accuracy and imaging quality of the recently introduced dual-layer CT. This was accomplished via various phantom measurements using the dual-layer detector CT system. In the following, an overview will first be given over the used dual-layer spectral CT scanner and the used phantom followed by a detailed analysis of the quantitative accuracy of the spectral images. The measurements presented include the determination of CNR, the measurement of energy-dependent Hounsfield units (HU) and quantification of iodine concentrations and effective atomic numbers.

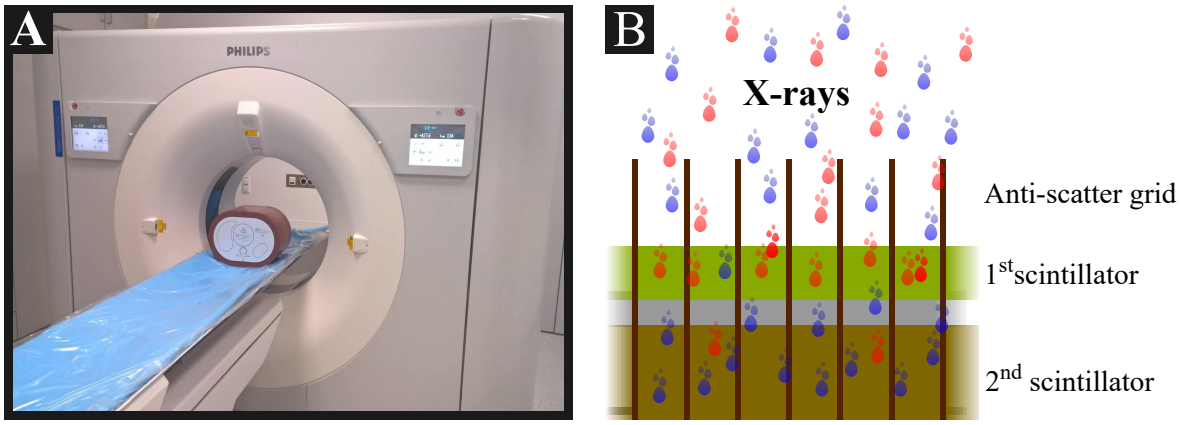

Figure 4.1: **The spectral CT scanner used for this study.** (A) shows a photograph of the dual-layer spectral CT system installed at the Klinikum Rechts der Isar of the Technical University of Munich, Germany. (B) outlines the principle of the dual-layer detector system. A polychromatic beam of x-rays impinges on the detector. The low energy photons (represented by red dots) are mostly absorbed in the top scintillator. This upper layer is mostly transparent to higher energy photons (represented by blue dots), which are then registered by a strongly absorbing second scintillator.

4.1 Dual-layer spectral CT

The measurements have been carried out on a commercially available dual-layer spectral CT system[1] installed at the Klinikum Rechts der Isar of the Technical University of Munich. The concept of a sandwich-type detector consisting of two layers of different scintillators for energy-selective CT imaging has already been proposed in 1978 [Brooks1978]. The present systems utilizes a similar concept consisting of a thin ZnS top layer and a thicker GOS bottom scinillator read out from side by an edge-on photodiode array [Carmi2005, Altman2009]. Since the registered signals in each detection layer can be shown to be effectively uncorrelated [Sones1989], standard methods for projection-based material decomposition can be employed in this concept, e. g. ML-based parameter estimation. The discussed scanner acquires spectral image data per default in every CT scan. Therefore, the need to select task-specific scanning protocols typical for other dual-energy scanners is eliminated. The spectral raw-data are processed in the projection domain and a decomposition into photoelectric and scattering basis functions is performed. This procedure enables efficient elimination of beam-hardening artifacts and proper treatment of the anti-correlated noise introduced by the material decomposition [McCollough2015, Brown2015, Kalender1988]. A conventional polychromatic CT image is also reconstructed from the summed contributions of both detector layers.

[1] IQon spectral CT, Philips Healthcare, USA

The available spectral image results include VMIs, iodine concentration maps, VNC images and effective-Z maps. Since all spectral results can be calculated from a suitable linear combination of the photoelectric and Compton basis images, all evaluations can be done retrospectively with the available scan data.

4.2 Description of the phantom

Semi-anthropomorphic phantom

During the following experiments, a modular semi-anthropomorphic phantom was used. The basic phantom body represents human abdominal anatomy[2] with dimensions of $300 \times 200\,\mathrm{mm}^2$. Larger patient sizes are simulated using additional extension rings made from adipose-equivalent material up to a total diameter of $600 \times 450\,\mathrm{mm}^2$. For the presented studies, extension rings consisting of adipose-equivalent material were used. In the center of the phantom, task-specific inserts can be installed using a $100\,\mathrm{mm}$ borehole. Figure 4.2 shows photographs as well as schematic drawings of the phantom geometry.

Task-specific inserts

For the evaluation of the dual-layer detector CT system, several task-specific inserts were used. Photographs of these inserts are shown in figure 4.3.

One insert consists of several medium-contrast features of decreasing size. The nominal contrast of the features with respect to the background ranges from $-25\,\mathrm{HU}$ to $-100\,\mathrm{HU}$ for the polychromatic spectrum of a W-anode tube at a voltage of $120\,\mathrm{kVp}$. This insert was used to assess the CNR and therefore the detectability of medium-contrast objects in different spectral images.

For the evaluation of the quantitative accuracy in images derived from the material decomposition, a custom-made insert was used providing four slots that can be equipped with rods of different materials. These rods were obtained from the same manufacturer together with their theoretical elementary composition and effective-Z values. A list of the used inserts is provided in table 4.1 along with the expected CT number of the inserts at $120\,\mathrm{kVp}$ and the corresponding effective atomic numbers. According to the

[2] QRM-Abdomen, QRM GmbH, Möhrendorf, Germany

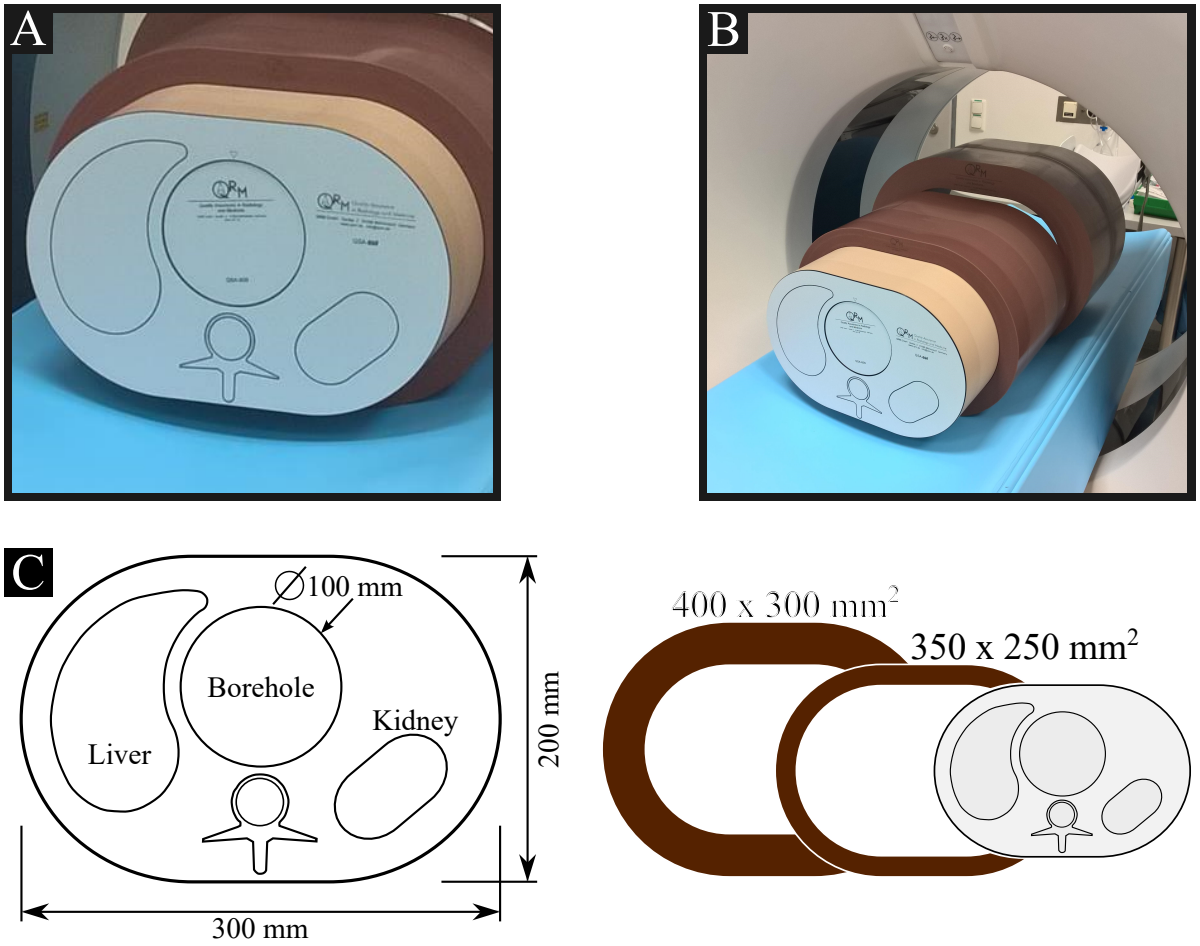

Figure 4.2: **Images of the semi-anthropomorphic abdominal phantom used to assess the image quality of the dual-layer spectral CT scanner.** The phantom features soft-tissue (35 HU), liver, spleen (both 55 HU) and spinal contrast features and can be extended with task-specific inserts located in the central borehole (A). The CT numbers mentioned for the phantom features are reference values valid for a tube voltage of 120 kVp. The phantom can be extended to mimic obese patients using additional stackable rings (B). The dimensions of the phantom and different extension rings are shown in (C) in units of mm.

manufacturer, the iodine samples contain additives in the resin to stabilize the iodine and minimize diffusion. Unfortunately, the exact formulation and amount of these additives are not known and therefore the effective atomic numbers remained undetermined. For the bone-like material, the BMD numbers refer to the mass concentration of calcium-hydroxyapatite (HA) embedded in a special resin.

Insert (tissue equivalent)	App. CT number / HU	Nominal Z_{eff}
Water	0	7.21
Muscle	45	7.31
Liver	56	7.32
Adipose	-80	5.65
Iodine 0.5 mg mL^{-1}	22	n.A.
Iodine 0.75 mg mL^{-1}	28	n.A.
Iodine 1.0 mg mL^{-1}	35	n.A.
Iodine 2.0 mg mL^{-1}	60	n.A.
Iodine 5.0 mg mL^{-1}	138	n.A.
Iodine 10.0 mg mL^{-1}	266	n.A.
Iodine 15.0 mg mL^{-1}	388	n.A.
Bone, BMD 100 mg cm^{-3}	125	8.64
Bone, BMD 200 mg cm^{-3}	255	9.76
Bone, BMD 400 mg cm^{-3}	502	11.17
Bone, BMD 800 mg cm^{-3}	1005	12.90

Table 4.1: **Description of the phantom inserts** used to characterize the quantitative accuracy of the spectral results generated by the dual-layer detector CT system.

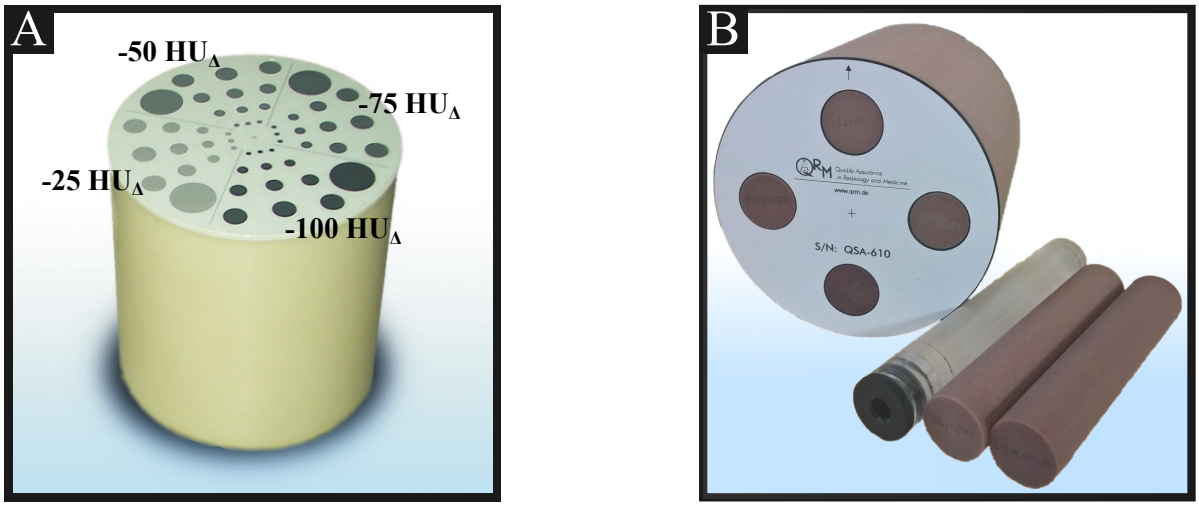

Figure 4.3: **Task-specific inserts for the QRM CT phantom.** An insert with medium-contrast features showing CT-number differences (HU_Δ) between -25 HU and -100 HU with respect to the background at 120 kVp is used to study the CNR behavior (A). Quantitative values of various spectral images (e.g. iodine concentrations, effective atomic numbers, energy-dependent HUs) can be investigated with a modular insert offering exchangeable material rods summarized in table 4.1 (B).

4.3 CT data acquisition and reconstruction

The parameters of the data acquisition were selected such that they are as close as possible to clinical routine protocols. According to the phantom, an abdominal CT protocol was selected. A tube voltage of 120 kVp was selected for all subsequent studies since the thickness of the detector layers is optimized to yield maximum spectral separation at this value. Each experiment was carried out at three distinct exposure levels resulting at volumetric computed tomography dose index (CTDIvol) values of 10 mGy, 20 mGy and 30 mGy. Exposure modulation was not used in order to guarantee direct comparability between different scans. Additionally, the scans were repeated five times each to enable basic statistical analysis of the obtained data. The exact tube loading and spiral pitch values were determined automatically by the scanner according to the selected protocol. For image reconstruction, conventional (polychromatic) CT images were reconstructed from the summed contributions of both detector layers using the manufacturer's proprietary `iDose` algorithm at level 0, i.e. no iterative post-processing was applied to the data. This setting corresponds closely to performing a plain filtered back-projection (FBP). Additionally, so-called spectral base images (SBIs) were obtained using material-decomposition on the projection data and subsequent image reconstruction was also carried out using an FBP-equivalent algorithm. For all images, the slice thickness and spacing was chosen to be 3 mm each. The largest extension ring was not used in this study since the phantom periphery would not be within the available acquisition field-of-view (FOV).

The specific type of spectral images (VMIs, iodine-maps, effective-Z maps) was selected after image reconstruction using the manufacturers spectral workstation[3].

4.4 Behavior of medium-contrast CNR in spectral images

In previous studies it was shown that VMIs can enhance the image quality by increasing the contrast between different tissues and optimizing the CNR [Yu2011, Yu2012, Pomerantz2013, Yamada2014]. Therefore, VMIs can contribute to a more accurate diagnosis and a potential reduction of radiation dose. However, it was also demonstrated e.g. in [Pomerantz2013] that the obtained CNR is a function of the energy at which a VMI is synthesized. This behavior is due to the amount of anti-correlated noise introduced by the material decomposition process as explained in section 2.4. The perfectly registered acquisition of spectral data in the spatial and temporal domain by the dual-layer detector enables to exploit the full statistical information and noise correlations. Advanced de-noising schemes applied directly

[3] IntelliSpace Portal V6.5, Philips Healthcare, USA

after projection-based material decomposition [Kalender1988, Petrongolo2015, Petrongolo2015a] can help to cancel out the correlations and substantially reduce basis image noise. Such an algorithm is implemented in the IQon scanner and an increased noise performance can be obtained compared to systems with sub-optimal spatial registration of spectral data. However, no detailed information on the actual implementation in the this particular system is available from the manufacturer or the literature.

To study the CNR in spectral images obtained by the IQon, CT images have been acquired using the phantom with the medium-contrast insert shown in figure 4.3B. In addition to the polychromatic image, VMIs were reconstructed covering the complete energy range available for evaluation extending from $40\,\mathrm{keV}$ to $200\,\mathrm{keV}$ in steps of $10\,\mathrm{keV}$. The medium-sized extension ring was used in this experiment yielding a total phantom size of $300 \times 400\,\mathrm{mm}^2$. The CNR is defined as

$$\mathrm{CNR} = \frac{|\overline{HU_\mathrm{C}} - \overline{HU_\mathrm{Bg}}|}{\sqrt{\sigma_\mathrm{C}^2 + \sigma_\mathrm{Bg}^2}}, \tag{4.1}$$

where $\overline{HU_{\mathrm{C,\,Bg}}}$ are the mean CT numbers in the contrasting features and the background and $\sigma_{\mathrm{C,\,Bg}}$ the associated standard deviations. To determine these values, a circular region-of-interest (ROI) was selected in the largest feature at each contrast level and the background at the positions indicated in figure 4.4 for each energy level. The five scans for each exposure level were averaged after calculation of the individual CNRs and the obtained values have been normalized to the corresponding CNR observed in the conventional image.

For the majority of contrast levels and energies, the CNR in the VMIs exceeds the values in the associated conventional image. For positive contrast values, the obtained increase is more than two-fold at lower energy levels. The overall behavior of the measured CNR does not depend on the radiation dose, c.f. figure 4.5. The observations made so far can be explained using the determined image noise in the same ROIs. Due to the noise reduction using statistical noise correlations in the basis images, the standard deviations can be kept at a constant value over a wide energy range from $50\,\mathrm{keV}$ up to $200\,\mathrm{keV}$ which is lower than the corresponding noise in conventional images (figure 4.5, right column). Therefore, the CNR is dominated by the difference in HU values. For energies of approximately $80\,\mathrm{keV}$ and higher, CT numbers are known to be roughly independent of energy for a wide range of materials whereas contrasts begin to rise drastically towards lower energies. Therefore, also the determined CNR rises at lower energies.

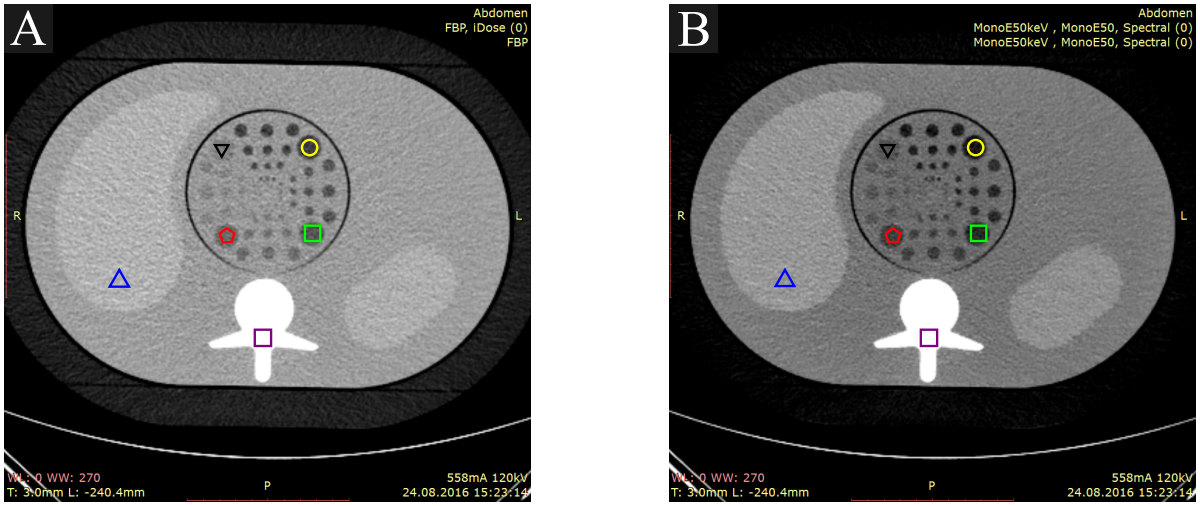

Figure 4.4: **Conventional CT image (A) and** 50 keV **VMI (B) of the medium contrast phantom insert.** Both images are shown in the same HU window. Increased contrast can be observed in the VMI due to the lower virtual photon energy. The location of the ROIs used to assess the CNR are marked in the images.

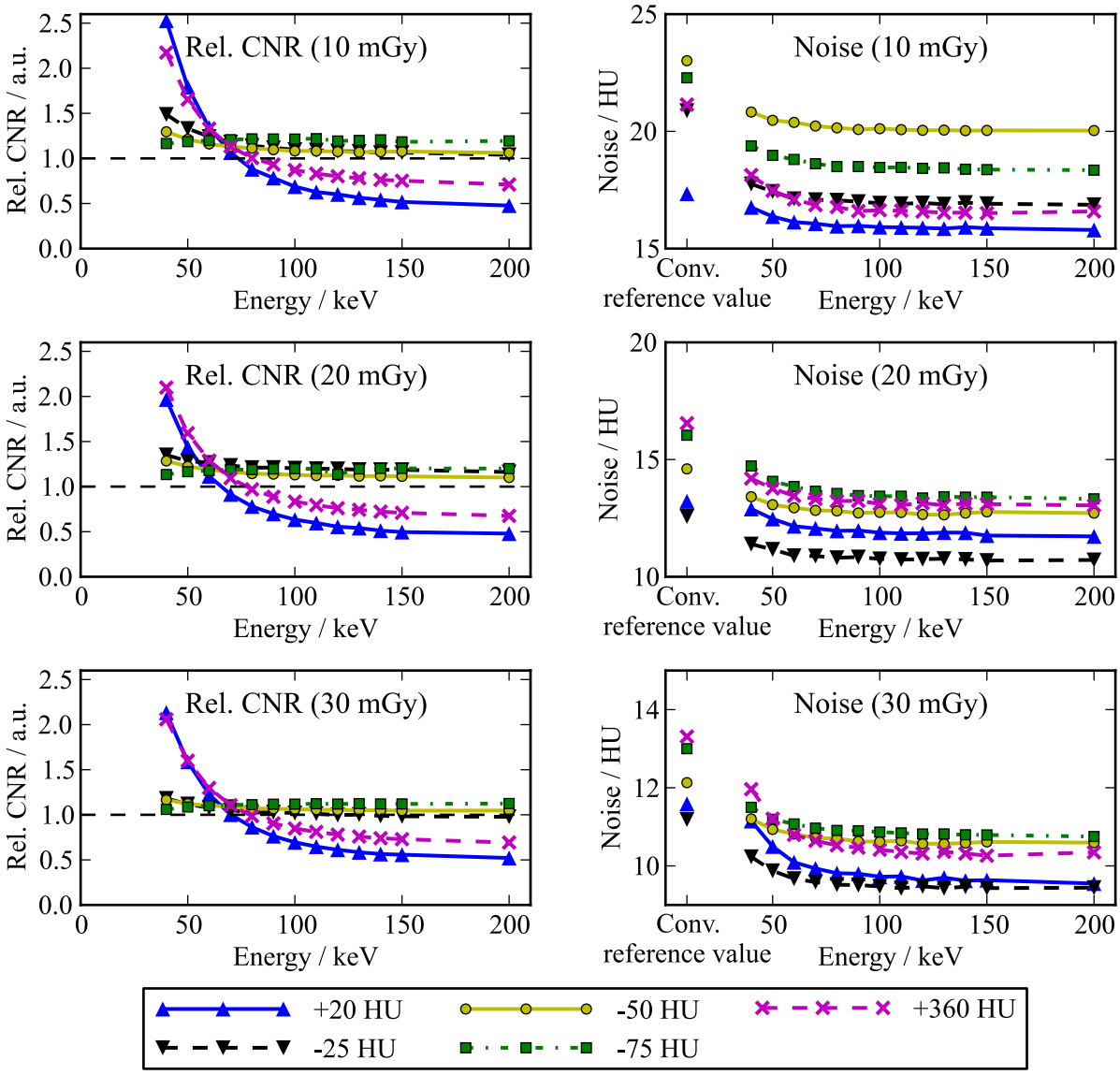

Figure 4.5: **Behavior of CNR in synthesized VMIs of the** $300 \times 400\,\mathrm{mm}^2$ **phantom at different dose levels.** The curves correspond to the ROIs marked in figure 4.4. The left column shows the measured CNR normalized to the conventional image while the corresponding image noise is shown in the right column. CNR values in VMIs are typically higher compared to the conventional image, while for positive contrasts more than a two-fold increase can be observed towards low energies. The mostly energy-independent noise curves are the result of the de-noising algorithm exploiting statistical correlations in the basis image noise.

4.5 Quantitative accuracy of energy-dependent CT numbers in VMIs

In the previous section it was demonstrated that the increased CNR in the VMIs is mostly due to the increased HU difference towards lower energies. Since HU values are based on the x-ray absorption difference of a given material with respect to water, they are in general an energy-dependent quantity. The accuracy of the calculated CT numbers in VMIs covering the available energy range will be evaluated in this section.

A theoretical reference for the values $\mathrm{HU}(E)$ of a given (compound-) material is established using the relation

$$\mathrm{HU}(E) = 1000 \cdot \frac{\rho_{\mathrm{mat}} \cdot \sum_i a_i \left(\frac{\mu}{\rho}\right)_i - \mu(E)_{\mathrm{H2O}}}{\mu(E)_{\mathrm{H2O}}}, \tag{4.2}$$

where E is the photon energy, ρ_{mat} the mass-density of the investigated material, a_i the mass fraction of chemical element i contributing to the material with the associated mass attenuation coefficient $\left(\frac{\mu}{\rho}\right)_i$ and $\mu(E)_{\mathrm{H2O}}$ is the absorption coefficient of pure water.

The evaluation was done measuring the spectral CT numbers for various insert rods representing different types of tissue, e.g. liver, fat, bone and iodinated blood. The theoretical values for these materials were calculated using the known chemical composition of the insert rods and their mass-densities as communicated by the phantom manufacturer. Inserting these values into eq. 4.2 yields the reference values comparison to the dual-layer CT system. However, the chemical composition and densities are subject to measurement inaccuracies and therefore, the reference values for the spectral HU values are of limited accuracy themselves. Applying error propagation to eq. 4.2 yields the accuracy of the reference values. As an example, the error interval for the mass density of the water-like insert is $\pm 0.02\,\mathrm{g\,cm^{-1}}$, which translates into a potential error of $\pm 20\,\mathrm{HU}$ in CT numbers.

The results of this evaluation is shown graphically in figure 4.6. We obtained an overall good agreement between measured and theoretical values. The shaded region around the curves of theoretical values indicate the tolerances of the calculated reference values. The errorbars of the measured values correspond to a 2σ interval with the measured standard deviation of noise. Typical errors of HU values measured in VMIs are well below $10\,\%$ for medium and high energies. At energies lower than $60\,\mathrm{keV}$, deviations of measured values from theoretical values can be detected which do not fall into the error intervals. This

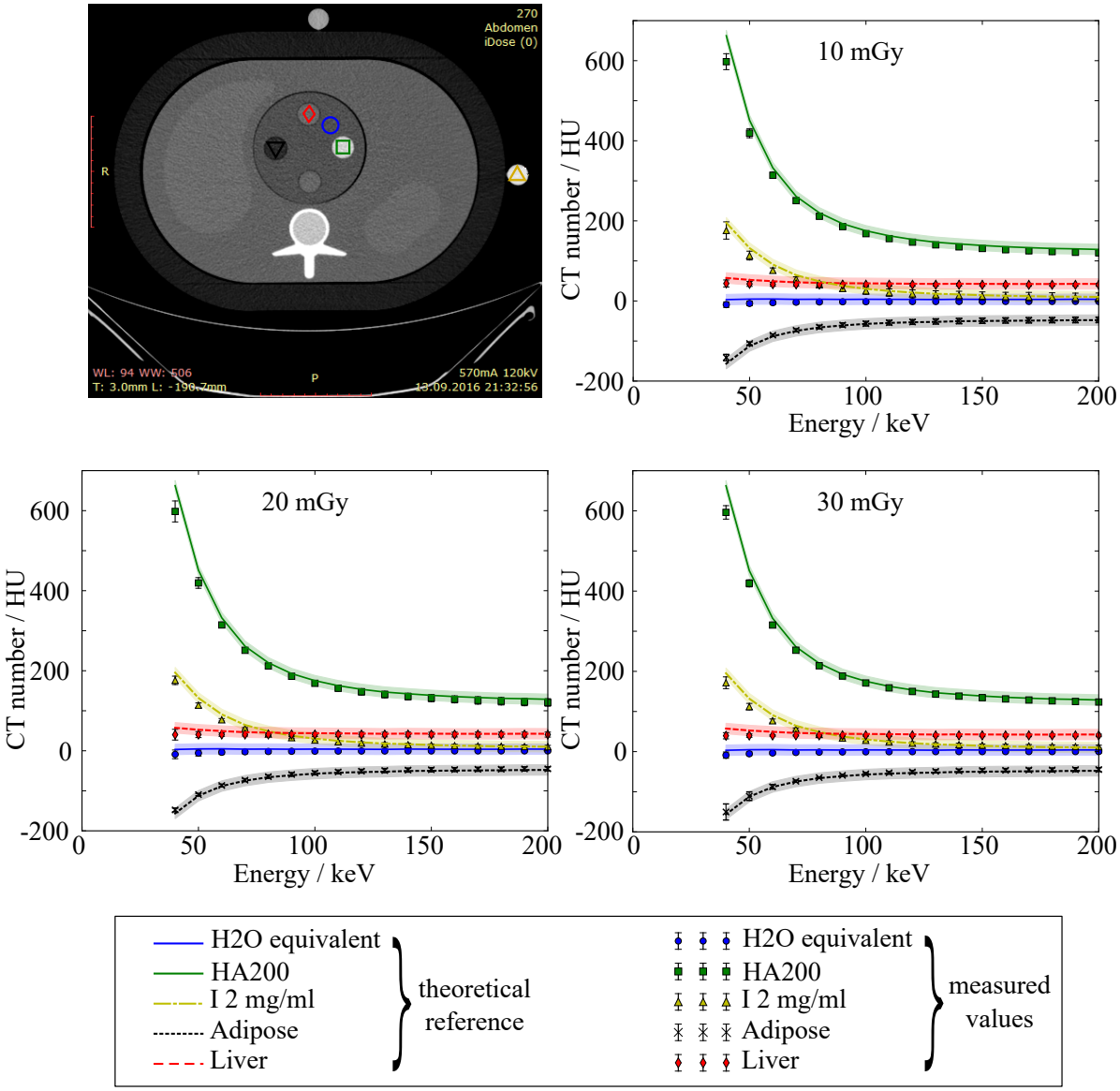

Figure 4.6: **Accuracy of spectral CT numbers at different dose levels.** The values of the spectral CT numbers were measured in the ROIs as indicated in the image. The properties of the different materials used in the measurements are summarized in table 4.1. For dose levels between 10 mGy and 30 mGy, a good overall agreement between measured and calculated HUs is observed. The accuracy of the measured values is indicated by the black errorbars. The reported elemental composition of the inserts are subject to certain tolerances, leading to an error interval for the theoretical values. This tolerance is marked by the shaded areas around the theoretical references.

behavior can partly be attributed to a general problem in a two bin spectral CT, namely the limitation of the decomposition into two basis materials. Especially for elements with higher atomic numbers like calcium or iodine, a two material basis is increasingly inaccurate when considering lower energies. The determined mean HU are mostly independent on the radiation dose which is again underlining the good quantitative performance of the spectral reconstruction algorithm.

4.6 Measurement of iodine concentration and effective atomic numbers

Quantification of iodine concentrations

The majority[4] of all of today's CT studies involve contrast agents based on non-ionic iodine. The average volumes administered to the patients amounts to $300\,\mathrm{mg\,kg^{-1}}$ body weight per examination. However, iodine-based contrast agents can also cause potentially harmful side-effects in patients in the form of allergic reactions and acute renal failure [Nash2002, Wang2008]. Therefore, the reduction of administered iodine amount would be highly desirable from a clinical perspective. Exact quantification of the contrast medium uptake in various tissues even for low concentrations can be a valuable help in achieving this goal. For this purpose, the dual-layer spectral CT scanner offers the possibility to generate iodine-maps where the presumed concentration of iodine in $\mathrm{mg\,mL^{-1}}$ is calculated for each voxel.

The phantom was equipped with different rods containing various known concentrations of iodine embedded into a water-equivalent material, see table 4.1. For the quantification of voxels at the phantom periphery, iodine samples have been added outside the phantom body to study eventual FOV-dependent effects in the decomposition accuracy. To investigate any dependence on patient size, measurements have been performed using the basic phantom ($200 \times 300\,\mathrm{mm^2}$) as well as using two extension rings ($250 \times 350\,\mathrm{mm^2}$, $300 \times 400\,\mathrm{mm^2}$) to simulate larger patients. For both measurements of iodine concentration and effective atomic numbers, the central axial slice from the spectral reconstruction was selected and the values in a circular ROI were measured for each concentration. The individual values from the five scan repetitions were averaged subsequently.

In figure 4.7, the distribution of the measured values of iodine concentrations in the spectral reconstruction is shown. The nominal values in the range from $0.5\,\mathrm{mg\,mL^{-1}}$ to $15.0\,\mathrm{mg\,mL^{-1}}$ are marked by the black dashed lines. Deviations of the measured values from the respective nominal values are typically

[4] approximately $85\,\%$

in the order of $0.25\,\mathrm{mg\,mL^{-1}}$ or less. Slightly increased errors towards larger phantom sizes can be observed for all concentrations.

The relative bias Δ_c of the measured concentration values c_m with respect to the true values c was determined according to

$$\Delta_\mathrm{c} = \frac{c - c_\mathrm{m}}{c}, \tag{4.3}$$

for all concentrations $c \geq 0\,\mathrm{mg\,mL^{-1}}$.

Figure 4.8 shows the relative bias of the measured iodine concentrations in dependence on the phantom size, exposure level and the location of the ROI in the FOV. First it is noted that the relative bias in many cases strongly exceeds a level of $10\,\%$ for smaller iodine concentrations $\leq 1\,\mathrm{mg\,mL^{-1}}$. Since the absolute deviation of measured concentrations from their true values peak at approximately $0.25\,\mathrm{mg\,mL^{-1}}$ (fig. 4.7), it is clear that exact quantification of iodine content becomes hard to achieve at such low concentrations. However, it needs to be noted that measurements in the background without the presence of iodine consistently yield $0\,\mathrm{mg\,mL^{-1}}$. Therefore, the overall presence of iodine in concentrations of $\geq 0.5\,\mathrm{mg\,mL^{-1}}$ is feasible using the investigated dual-layer CT scanner. This finding constitutes an important result by itself, since most other state-of-the-art dual-energy systems yield residual concentrations of iodine in the background between $0.1\,\mathrm{mg\,mL^{-1}}$ and $0.2\,\mathrm{mg\,mL^{-1}}$ that might even extend into negative concentrations [Li2015], making a reliable detection of low iodine concentrations typically a challenging task.

The dependency of the bias on the phantom size is investigated in table 4.2. Here, the root-mean-squared (RMS) values of both the absolute concentration errors and the of the associated relative bias were calculated. All iodine concentrations and exposure levels were averaged in the RMS values. An increase corresponding to the phantom size is observed for both error measures. The relative bias increases from $2.2\,\%$ in the small configuration to $5.7\,\%$ in the large phantom.

The observed bias increase towards larger phantom sizes corresponds well to other findings of patient size-dependent iodine accuracy reported in the literature [Koonce2014, Marin2015].

Phantom size	**RMS abs. error**	**RMS rel. bias**
S: $250 \times 200\,\mathrm{mm}^2$	$0.05\,\mathrm{mg\,mL}^{-1}$	$2.2\,\%$
M: $300 \times 350\,\mathrm{mm}^2$	$0.15\,\mathrm{mg\,mL}^{-1}$	$5.0\,\%$
L: $300 \times 400\,\mathrm{mm}^2$	$0.27\,\mathrm{mg\,mL}^{-1}$	$5.7\,\%$

Table 4.2: **Dependency of the iodine quantification RMS errors on the phantom size.** The values have been averaged over all exposure levels.

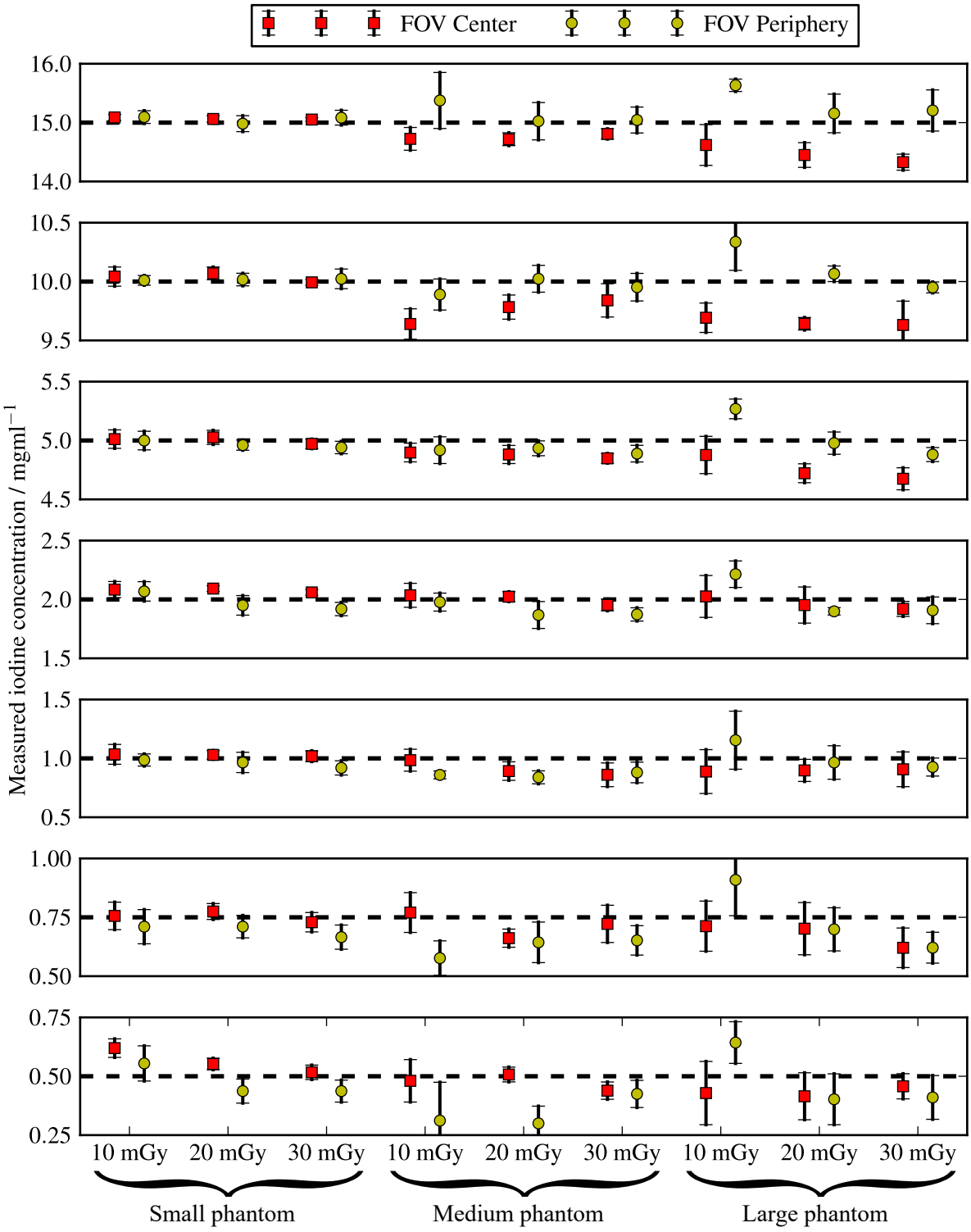

Figure 4.7: **Accuracy of measured iodine concentrations at different dose levels and phantom sizes.** Each panel shows the distribution of the measured values in the FOV's center and periphery around the nominal values (indicated by the dashed black lines). The largest differences between measured and nominal values are in the order of $0.25\,\mathrm{mg\,mL^{-1}}$.

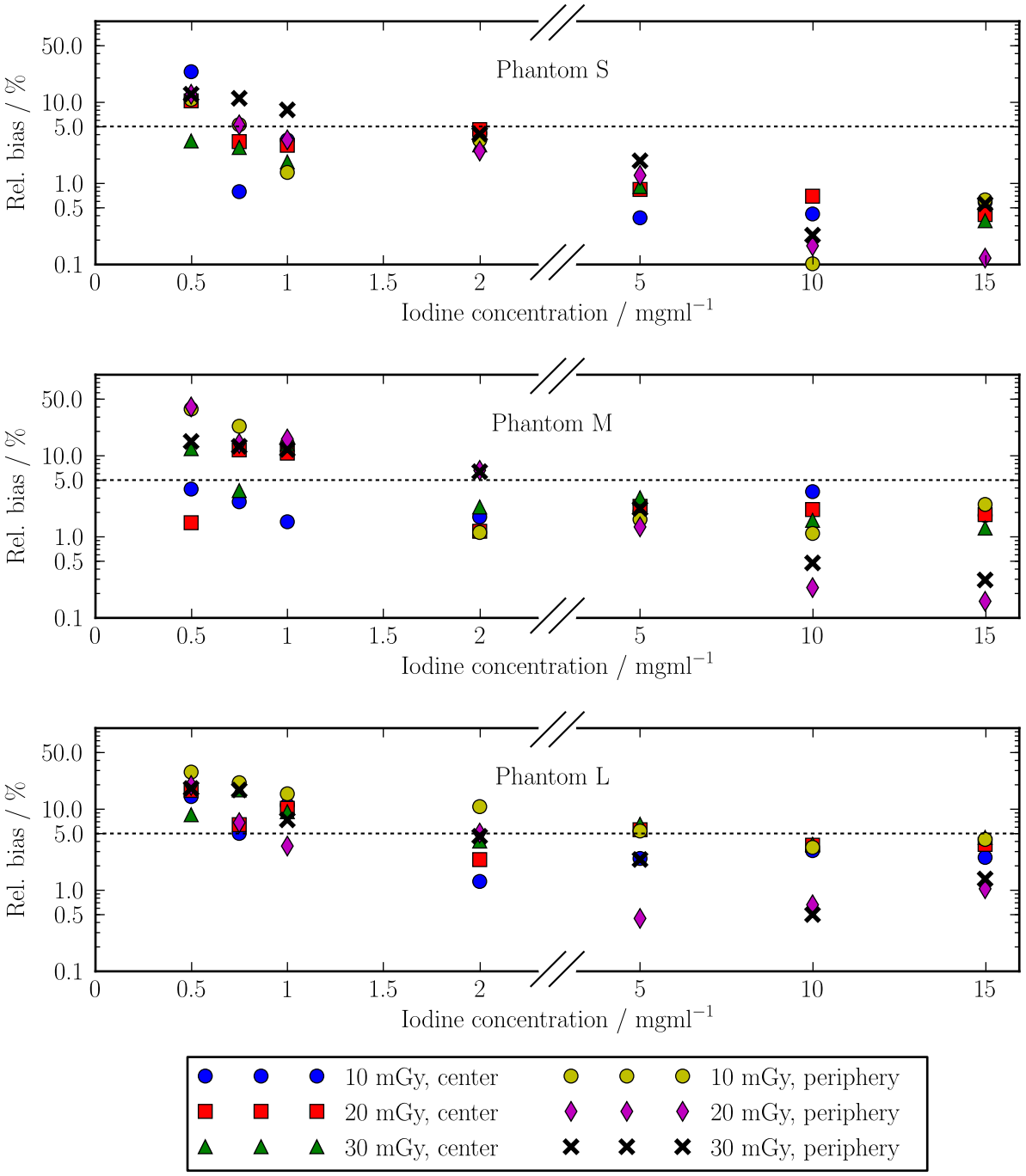

Figure 4.8: **Relative bias of iodine quantification at different dose levels and phantom sizes.** From top to bottom, each panel shows the bias of the measured iodine concentration in the small, medium and large phantom normalized to the respective nominal values according to equation 4.3. For concentrations of 1 mg mL^{-1} and above, the relative bias is typically peaks at around 5 % and is considerably smaller than that for most cases.

Quantification of effective atomic numbers

Effective atomic numbers Z_{eff} are used for the characterization of the radiation response of compound materials containing multiple chemical elements. The most wide-spread definition of Z_{eff} is given by [Murty1965, Bonnin2014]

$$\begin{aligned} Z_{\text{eff}} &= \sqrt[2.94]{\sum_i f_i Z_i^{2.94}}, \\ f_i &= \frac{n_i Z_i}{\sum_i n_i Z_i}, \end{aligned} \tag{4.4}$$

where i indicates each chemical element in the compound with its atomic number Z_i while n_i is the number of atoms of each chemical element. Therefore, f_i gives the relative amount of electrons contributed by element i. Z_{eff} can for example be calculated directly from a material decomposition into photoelectric and Compton basis images. Using the definitions for the photoelectric and Compton basis images, a_{ph} and a_{C}, one obtains

$$Z_{\text{eff}} = \sqrt[3.2]{\frac{1}{\text{C}_\text{p}} \frac{a_{\text{ph}}}{a_{\text{C}}}}. \tag{4.5}$$

Z_{eff} was measured for the inserts equivalent to the materials water, liver, muscle, adipose tissue and bone (200 mg mL^{-1} HA). Iodine was not included in the study since the exact elemental composition of the samples could not be determined by the manufacturer. The values were measured in ROIs located in the FOV center of the medium-sized phantom ($350 \times 250\,\text{mm}^2$). Figure 4.9 shows the results obtained from the scanner's effective-Z map. The errorbars in the left panel correspond to the 3σ - interval of the five individual measurements at every x-ray exposure level. For all tissue surrogates except for the adipose-like material the relative bias is in the range of $1\,\%$ or less. Therefore, a generally very good quantitative performance of the spectral forward-model can be observed. Therefore, the larger errors in the adipose sample can be explained by assuming small errors in the reported elemental composition.

Insert	Nominal Z_{eff}	Relative bias / %		
		10 mGy	20 mGy	30 mGy
H_2O	7.21	0.1	0.4	0.4
Liver	7.32	0.1	0.9	1.1
Muscle	7.31	0.4	0.6	0.6
Adipose	5.65	8.2	6.8	6.8
HA 200	9.76	0.4	0.6	0.8

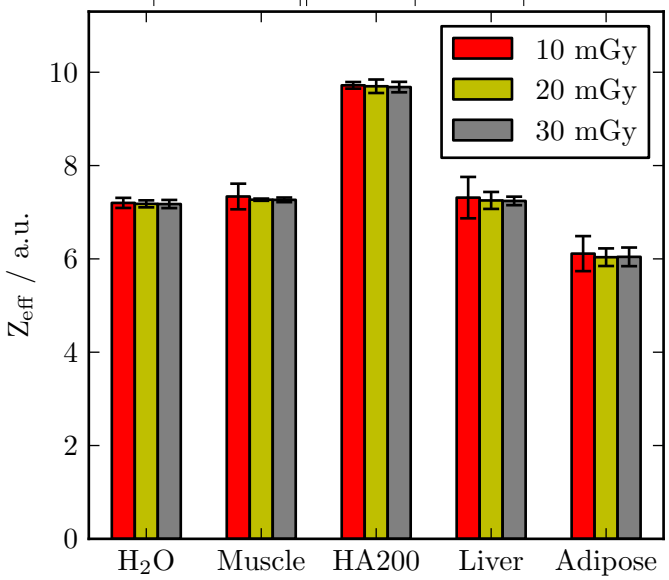

Figure 4.9: **Quantitative accuracy of effective atomic numbers from different tissue surrogates at the three investigated exposure levels.** All relative bias values are in the range of 1 % or less with the exception of adipose-like material. Backed by the high accuracy of the other samples, the larger bias in this case indicates a potentially wrong assumption of the elemental composition.

4.7 Discussion

During the investigation of the spectral imaging performance of the newly available dual-layer detector-based spectral CT scanner, we have found a very good overall quantitative accuracy of the spectrally derived images [Ehn2017]. Especially the strongly increased CNR in VMIs towards lower energies and the high accuracy in quantification of iodine concentrations within only a few percent of the true values open up several new possibilities in clinical practice to reduce radiation exposure and improve diagnostic accuracy [Pache2010, Takahashi2010, Bamberg2011, Yuan2012, McCollough2015]. One key advantage of the dual-layer concept is the detector-based acquisition of the spectral data. Therefore,

energy-resolved projections are nearly perfectly registered in the spatial and temporal domain, which is not the case for any other commercially available dual-energy scanner at the moment.
Due to an effective reduction of basis material image noise, the noise in calculated VMIs can be kept at a nearly constant value below the conventional reference value. Only towards lower energies a small increase of the noise level is observed. A strong increase of CNR for some material pairs could be obtained consequently, cf. section 4.4. To the best of our knowledge, the discussed behavior of the CNR in VMIs was first observed in this study. Until now, general literature on dual-energy imaging and CNR curves of VMIs reports a global maximum at a distinct energy level which is unique for a specific pair of contrasting materials [Yu2011, Pomerantz2013]. The observed CNR of the negative contrast features in the phantom yields roughly flat energy-dependent curves that are also nearly parallel for all negative features. Due to the generally reduced noise level in VMI the CNR of these features is higher compared to the conventional image in a vast majority of measurements however the relative increase is much smaller than found in the positive features. A possible explanation for this observation is that the negative contrast features and the background all consist of the same basic material where different attenuation is effectively due to varying mass densities of the features. This assumption was later confirmed by the phantom's manufacturer where different amounts of air inclusions are used to reduce the mass density of negative features with respect to the background. For actually different materials a much stronger CNR increase should be obtained similar to the analogous contrast features.

However, also the dual-layer scanner suffers from the basic limitations of a dual-energy system which arise due to the simple modeling of x-ray attenuation using only two spectral basis functions. One example of such limitations is the reduced accuracy of spectral HUs in low-energy VMIs, cf. section 4.5. Especially for materials with higher atomic numbers such as calcium and iodine, coherent scattering becomes increasingly important and might not be neglectable at lower energies. As a rough estimate of the importance of this process, it should be noted that for iodine, the point of equality between coherent and incoherent scattering lies approximately at $104\,\mathrm{keV}$ and therefore the coherent scattering process dominates over the largest portion of the diagnostic energy window. Using three or more energy-channels and material basis functions could therefore potentially improve the quantitative accuracy of spectral CT images even further, especially towards lower energies. In this context, contrast agents form a special group of materials. Their principle of operation is based on the high absorption of x-rays thanks to k-edges present in the used energy range. Since k-edges would in principle also require a dedicated spectral basis function, the quantification of iodine content in a dual-energy system relies on the fact that the spectrum which arrives at the detector is sufficiently hard enough that the minimum energies lie above the absorption edge. As this is not typically the case for clinical CT tube spectra[5] the additional absorption of x-rays by the patient is essential to achieve this constraint. Even then, numerical

[5] Given an acceleration voltage of $120\,\mathrm{kVp}$ and a filtration with $4 - 5\,\mathrm{mm}$ Al

corrections are often applied to compensate for the effects of lower energies in the vicinity of the k-edge which can still be present for average of smaller patient sizes. This might also be a factor causing the increased bias of iodine concentrations in larger object sizes. When the diameter of the attenuating object becomes sufficiently large, virtually all photons next to the k-edge are eliminated from the x-ray spectrum. In this case, the aforementioned spectral corrections would not be required anymore and could in turn decrease the quantitative accuracy.

Given these limitations, the use of PCDs with a larger number of energy channels can overcome some of the issues discussed so far. As an example, the possibility to distinguish two different contrast agents from other body tissues typically requires at least four energy bins and would open up some new clinical applications [Schlomka2008, Schirra2014, Muenzel2016]. Last but not least, the exact measurement of Poisson-distributed photon count numbers without electronic noise facilitated by PCDs will also help to reduce radiation exposure and contrast media volumes further. Therefore, most of the remaining part of this thesis will focus on the investigation of PCDs applied to spectral CT imaging.

5 A python framework for simulation of spectral photon-counting image acquisition

In the previous chapter, some of the possible benefits of spectral imaging applied to the field of clinical CT have been demonstrated for a dual-energy approach based on a dual-layer integrating detector. The potential benefits promised by the use of PCDs can further improve image quality and add the capability to discriminate more than two energy bins and materials. As briefly outlined in section 3.2, equal weighting of all photons and the wide dynamic range down to zero photons can contribute to improved SNR is the images. Nevertheless, the higher amount of spectral information and the special signal properties of PCD-based systems typically require specialized material decomposition techniques and post-processing schemes with very active research in this area. Additionally, imperfections and performance drifts in PCDs are substantially different from the behavior known from integrating devices and therefore also need detailed investigation. Unfortunately, the commercial or academic availability of PCDs is still limited today, especially when equipped with a high-Z sensor with a FOV suited for x-ray imaging applications of larger objects at high energies. Therefore, the use of simulation studies in developing new data processing methods and to study the implications of spectral distortions introduced by the detector is still essential. In this context, a simple but nearly full-featured simulation framework for spectral imaging tasks based on PCDs was developed for various research applications within the Chair for Biomedical Physics. its basic structure will be presented in the next section followed by the demonstration of some applications of the framework.

5.1 Structure of the simulation framework

The simulation package for PCDs is implemented in `python`-code. The class diagram of the package showing the general structure of the framework with all its member variables and methods is given in

figure 5.1. The central component is the `PcDetector` class which implements all essential functions and characteristics of the detector, e.g. the shape of the pixel matrix, the number and position of the used energy thresholds (THLs) and information about the spectral response of the system. Besides the basic variables responsible for the detector behavior and performance, it features methods that emulate the basic functionality of a PCD detector, from which the most essential one is simulating images dependent on a specific phantom and a source spectrum.

Additional information about the performance can be obtained by calculation of spectral separation or the CRLB. A `PcDetector` object is further split into objects describing the properties of the x-ray sensor through the `XraySensor` class and a module that controls the spectral response of the detector thresholds using the `EnergyResponse` class.

The basic `PcDetector` object is created using the following lines of code:

```
1 from PCDSimulation import *
2 myDetector = PcDetector(shape=(64, 1536), energyResponse='ideal',
    ↪ thl=[20.] , thlSampling=1., thlDistributionSigma=0.,
    ↪ sensorMaterial='CdTe', sensorThickness=2.)
```

Listing 1: Creation of a `PcDetector` object.

The constructor in listing 1 contains the most basic properties needed to determine the behavior of the simulated detector:

- `shape`:
  The number of lines and columns in the pixel matrix of the detector, expressed as python tuple.

- `energyResponse`:
  The basic form of the energy response function.
  Valid parameters are `'ideal'`, `'noise_escape'` and `'realistic'`. The properties of the energy response functions are discussed in more detail later.

- `thl`:
  A list with the positions of all used energy thresholds in keV.

- `thlSampling`:
  The sampling of the spectral parameters such as energy response or quantum efficiency in keV.

- `thlDistributionSigma`:
  The standard deviation of the threshold distribution across individual detector pixels in keV. Individual thresholds are Gaussian random variables centered around the values determined by the `thl` parameter.

- `sensorMaterial`:
  The material of the x-ray sensor. Available sensors are `'CdTe'`, `'GaAs'` and `'Si'`.

- `sensorThickness`:
  The thickness of the x-ray sensor in mm.

Implementation of the spectral behavior

The spectral performance of the detector is primarily dominated by two components: The quantum efficiency of the x-ray sensor and the energy response of the complete detector system.

According to section 3.2.1 the quantum efficiency $\mathrm{Q}(E)$ describes the fractions of incident photons that are absorbed in the sensor layer as function of energy. It can be calculated as

$$\mathrm{Q}(E) = 1 - e^{-\mu_\mathrm{S}(E) d_\mathrm{S}}, \tag{5.1}$$

where $\mu_\mathrm{S}(E)$ and d_S are the sensor's absorption coefficient and thickness.

The used detector's energy response function $\mathrm{R}(E, E')$ is implemented according to the model suggested in [Schlomka2008] and describes the fraction of incident photons with the energy E being counted at a detector threshold E'. It contains terms for the primary photon peaks as well as possible escape and fluorescence peaks and spectral distortions due to charge-sharing in the radiation sensor:

$$\mathrm{R}(E, E') = N(E) \left(e^{-\frac{(E'-E)^2}{2\sigma^2}} + c_\mathrm{e} e^{-\frac{(E'-E_\mathrm{e}-E)^2}{2\sigma_\mathrm{e}^2}} + c_\mathrm{f} e^{-\frac{(E-E_\mathrm{e})^2}{2\sigma_\mathrm{e}^2}} + B(E, E') \right). \tag{5.2}$$

In this notation, E is the incident photon energy, E' is the threshold energy at which the photon is finally registered and $N(E)$ is a normalization constant used to preserve the incident flux at each energy. The first term inside the brackets describes the primary photo-peak where the incident photons are registered

exactly at the threshold corresponding to their energy. The photo-peaks have finite width dependent on the detector electronics in the pre-amp and shaper and are therefore modeled as Gaussian with standard deviation σ. Additionally, escape and fluorescence peaks can be observed for high-Z sensor materials which are described by the 2nd and 3rd terms. In here, E_e denotes the average energy of a fluorescence photon emitted by the sensor. For example in cadmium-telluride (CdTe) this is $E_\mathrm{e} \simeq 25\,\mathrm{keV}$. The constants c_e and c_f control the intensities of escape and fluorescence events. Finally, charge-sharing is modeled by a constant background contribution of $B(E, E')$ which depends on the incident energy and drops to zeros for $E' \geq E$.

The spectral bin sensitivity of a PCD which is used in equation 2.24 can be expressed by

$$S_i(E) = \int_{E_i}^{E_{i+1}} R(E, E')\mathrm{d}E', \quad i = 1...N, \tag{5.3}$$

using the detector's spectral response function $R(E, E')$ introduced above.

Using this model, three pre-defined response types are available when creating a `PcDetector` object, see figure 5.2:

- `'ideal'`:
  In this case, thresholds are modeled effectively as delta-distributions by setting $c_\mathrm{e} = c_\mathrm{f} = B(E, E') = 0$ and considering $\lim_{\sigma\to 0} \mathrm{R}(E, E')$. Such a response would characterize an ideal PCD that does not introduce spectral distortions of any kind to the incident spectrum.

- `'noise_escape'`:
  This model acknowledges finite energy resolution of the thresholds and also features escape and fluorescence events. However, no charge-sharing is assumed by setting $B(E, E') = 0$. Such a response function may be used to study PCDs with intrinsic charge-sharing correction.

- `'realistic'`:
  Adds a finite charge-sharing term to the response function.

In the `PcDetector` implementation, the response is sampled at discrete energy intervals $\Delta E'$ controlled by the `thlSampling` variable. The bin sensitivity functions $\mathrm{S}(E)$ associated with these response function models can then be obtained by a discrete sum of the energy response over the detector

threshold:

$$\mathrm{S}(E) = \sum_{E'_{\mathrm{L}}}^{E'_{\mathrm{H}}} \mathrm{R}_{E,E'} \cdot \Delta E'. \tag{5.4}$$

In order to incorporate pulse pile-up effects, the total flux seen by each detector pixel must also be known. Therefore, pile-up does not only depend on the incident spectrum and the threshold's energy response function but also depends strongly on the composition and spatial dimension of the sample that is subject to the imaging application. As a consequence, correct treatment of pile-up must be performed after simulation of spectral photon-counting data with a specific phantom and can for example be realized by the use of so called pile-up matrices [Roessl2012].

Finally, the combination of the discussed effects allows the definition of effective spectra $\Phi_{\mathrm{eff}}(E)$ that are registered by a specific energy bin i of the PCD:

$$\Phi_{\mathrm{eff},\,i}(E) = \Phi_0(E) Q(E) S_i(E), \tag{5.5}$$

in which $\Phi_0(E)$ is the incident spectrum emitted by the x-ray source, $Q(E)$ describes the quantum efficiency of the sensor and $S_i(E)$ the bin sensitivity determined according to equation 5.4.

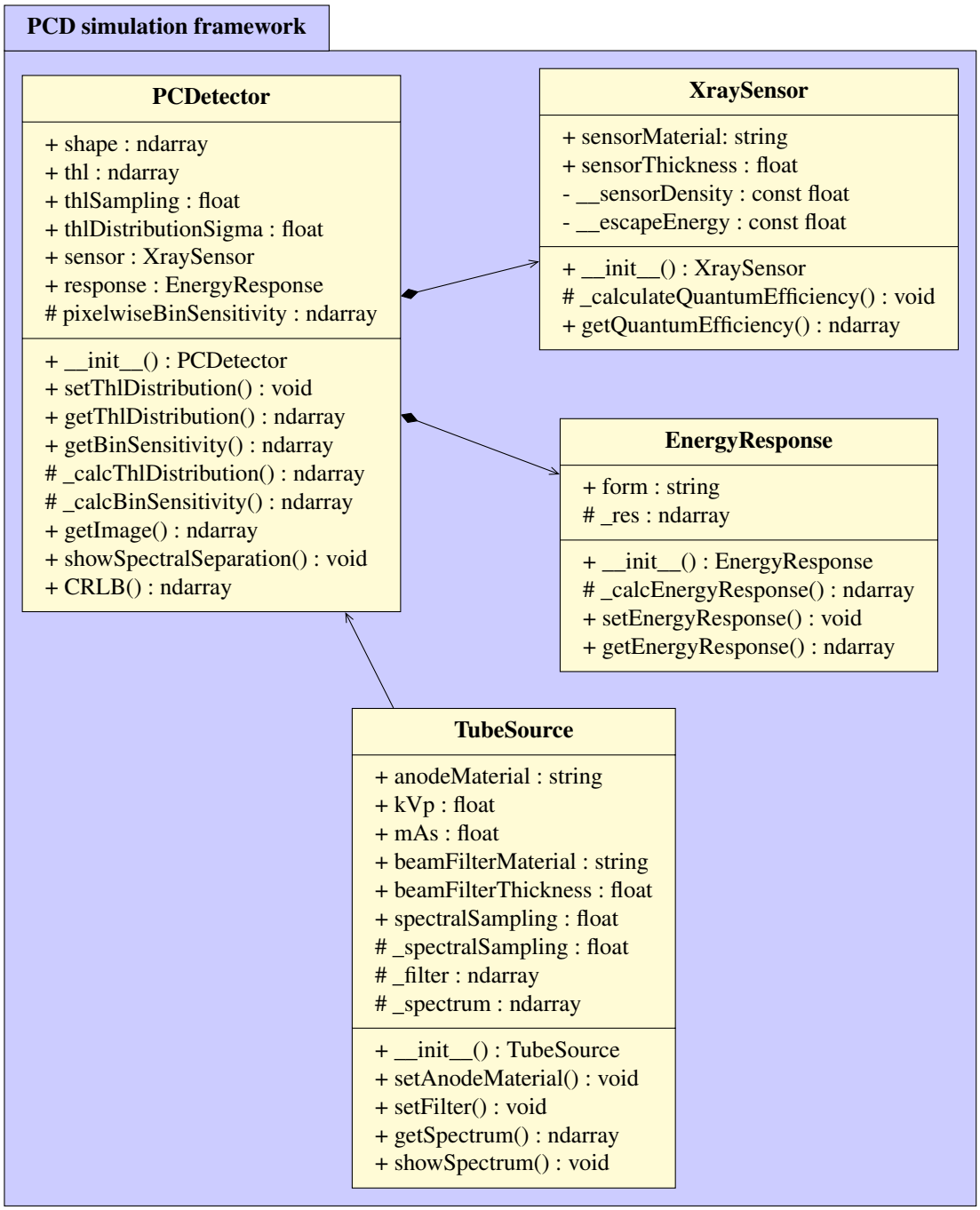

Figure 5.1: **Class diagram of the PCD simulation framework.** The boxes inside the framework list all classes used by the simulation. Following the UML standard, the sections below the class names list all available public and private variables along with their datatype. In the last section of each class, the implemented methods are listed with the datatype of their return values.

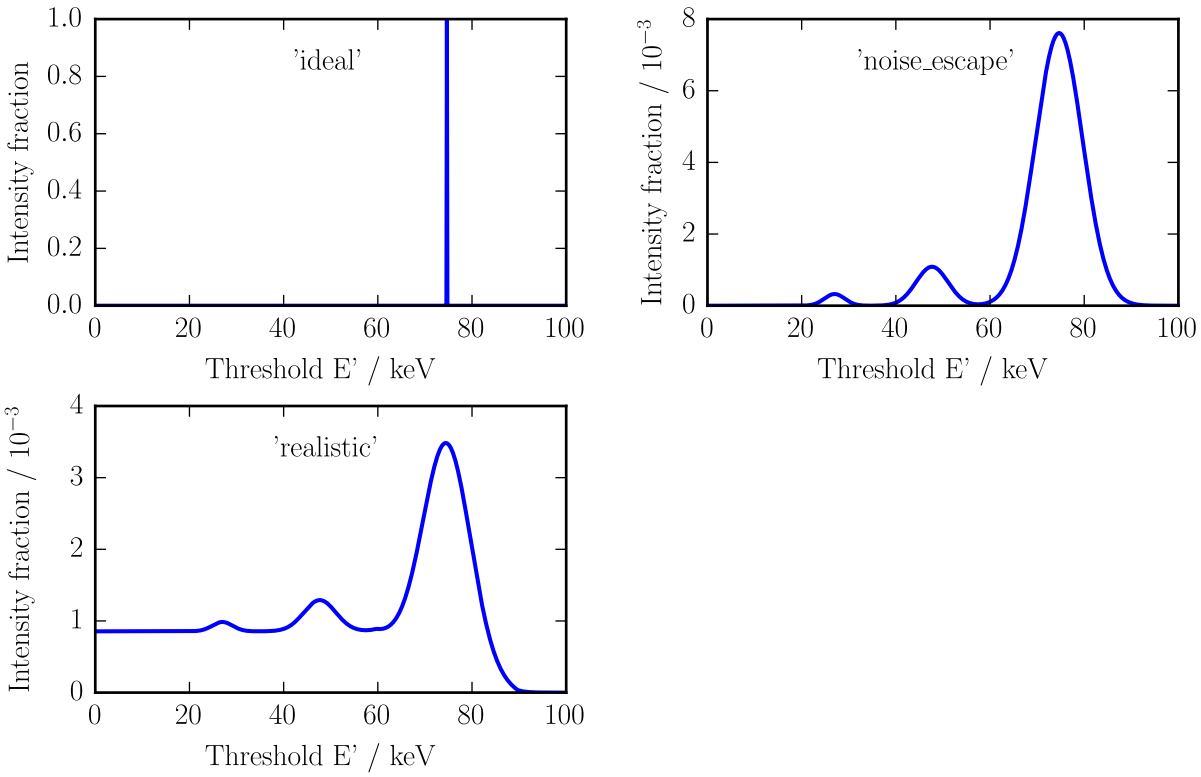

Figure 5.2: **Available types of energy response function in the PCD simulation framework.** The three different types are identified by names that are given to the `PcDetector` object constructor. The plots show the detector response to a beam of monochromatic photons with an energy of 70 keV.

Implementation of an x-ray source

Basic simulations of emitted x-ray spectra can be carried out using the class `TubeSource`. It implements the TASMIP and MASMIP algorithms [Boone1997, Boone1997a]. Therefore, tungsten (W) and molybdenum (Mo) are available as anode materials. Additional filtration can be added using the `beamFilterMaterial` and `beamFilterThickness` variables. The initial output of the TASMIP algorithms is sampled at energy intervals of 1 keV. To obtain a finer energy grid, the output is linearly interpolated to an energy grid of ΔE controlled by the `spectralSampling` variable. The total flux is conserved during this step. The final output is a photon number spectrum of the form $\frac{\text{number of photons}}{\Delta E \text{ mm}^2 \text{ s}}$ at a source-to-detector distance of 1 m. Geometrical parameters effecting the number of photons per detector pixel, i.e. the pixel size and the specific source-to-detector distance, must be regarded separately in the `PcDetector` simulation. Listing 2 shows the basic commands used to generate a tungsten spectrum that is used in the simulations discussed in the subsequent sections.

```
# acquisition geometry:
SID = 1 # source-to-detector distance in meter
pixelSize = 0.1 # in mm

eSampling = 1.0 # spectral sampling of the energy domain in keV
E = np.arange(0., 150.+e_sampling, e_sampling)

t = tubeSource(spectralSampling=eSampling, kVp=120., mAs=5.,
 ↪  beamFilterMaterial='Al', beamFilterThickness=4.0)
s = t.getSpectrum()

# incorporate geometry:
s *= (1./SID)**2 * pixelSize**2
```

Listing 2: Definition of the source properties for the presented simulations.

5.2 Applications to spectral imaging

Investigation of the spectral separation in the energy bins

In various sections throughout this thesis spectral distortions introduced by the PCD components, particularly the x-ray sensor and the readout ASIC, have been discussed (c.f. sections 3.3 and 5.1). Especially

charge-sharing and pulse pile-up effects but also the presence of escape/fluorescence peaks and finite energy resolution of the detection thresholds may lead to considerable overlap between the x-ray spectra that are effectively registered in each energy bin of a PCD. Additionally, the energy-dependent quantum efficiency of the x-ray sensor also alters the spectrum seen by the detector compared to the emitted spectrum, however does not introduce spectral overlapping between adjacent energy bins. The `PcDetector` class also implements the functionality to investigate and plot the spectral separation for a given combination of incident spectrum emitted by the source and a PCD detector with a specific setting of energy bins.

The code in listing 3 was used to determine the bin sensitivity functions and the separation of the effective spectra for a PCD with a 2 mm CdTe sensor and a realistic energy response function as defined in figure 5.2. In this study, a 120 kVp source spectrum was assumed and four THLs were equidistantly distributed between 25 keV and 85 keV.

```
1        res = 'realistic'
2        dSens = 2.
3        thls=[25, 45, 65, 85]
4
5        det = PcDetector(energyResponse=res, thl=thls, thlSampling=eSampling,
          ↪  sensorThickness=dSens)
6        det.showSpectralSepapration(s, normalizeSpectra=False)
```

Listing 3: Calculation and plotting of the spectral separation of a given source-detector combination.

Figure 5.3 shows the result of the calculation of bin sensitivities and effective spectra for the set-up of listing 3. The first plots show the response of the detector to photons carrying the exact energy of the THLs. From the energy response function, the bin sensitivity curves are calculated as defined in equation 5.4. Considerable overlap between each of the four bins can already be appreciated in these plots. Typically, each bin is extended towards energies higher than its upper threshold through the combined effects of charge-sharing and escape photons. The energy level at which the escape photons' energy becomes low enough to be registered in a specific bin can be seen as a slight step in the high energy tails of the sensitivity curves. Within the energy window defined by the thresholds which are associated with each bin, the curves exhibit a decreased sensitivity towards lower energies. This behavior is also due to fluorescence emission where now the energy of the escape photon is smaller than the lower threshold. The finite width of the photo-peaks can directly be seen at the energy bin boundaries where it leads to a blurring of the thresholds.

Comparing the effective energy spectra that result from these bin sensitivities, one immediately finds the spectral overlap between the bins. As indicated by the sensitivity functions, the overlap is especially pronounced in lower bins that are extend towards higher energies. This observation is significant for PCD-based systems suffering from charge-sharing and escape photons. In contrast, the lower energy channel in dual-source based CT measurements is typically well delimited by the cut-off energy at the respective acceleration voltage limit while the high energy bin reaches towards low-energy potions of the spectrum. Furthermore, the effective spectra in figure 5.3 show large differences in their overall intensities. This might lead to problems in material decomposition applications, especially since the presence of any sample will shift the spectra additionally.

This implies that the optimal choice of energy bins is highly task-dependent and the equidistant spacing of THLs discussed here is commonly not well-suited for spectral imaging tasks. Therefore, a procedure to optimize the position of energy bins will be discussed in the following section.

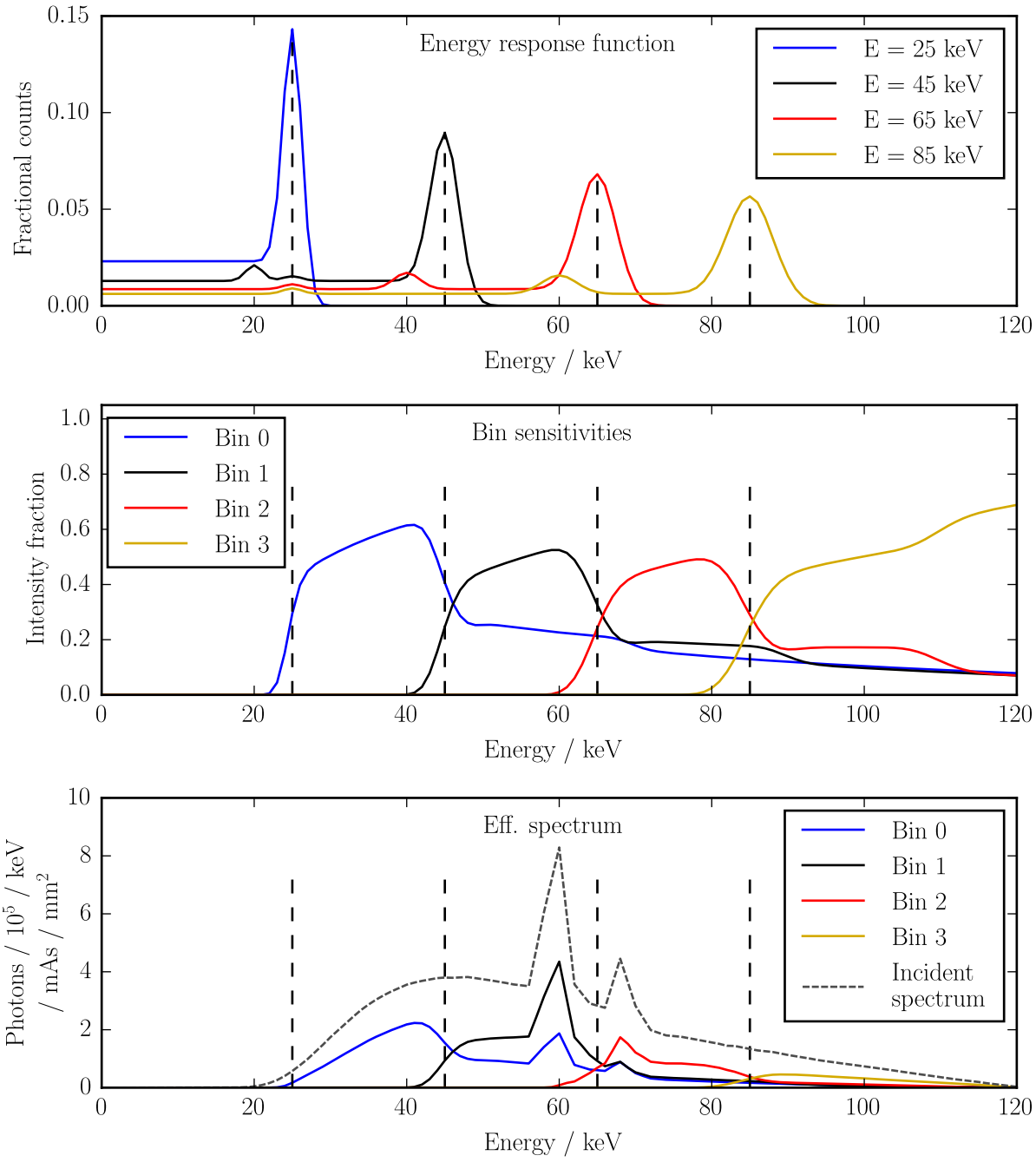

Figure 5.3: **Spectral separation simulated for a detector with realistic energy response function.** In this case, the incident spectrum coming from a W anode was characterized by a 120 kV acceleration voltage and 4 mm Al filtration. The PCD had four energy thresholds which were equidistantly spaced and marked by the vertical dashed lines. Note that both the bin sensitivities and effective spectra seen by the detector exhibit a considerable overlap at the energy bins boundaries.

Determination of optimal location for energy thresholds

According to the equations presented in section 2.3, material decomposition in spectral x-ray imaging can be treated as parameter estimation problem. During parameter estimation of statistical distributions using a limited sample collective, statistical errors in the used sample collective will propagate into the values of the estimate. Therefore, the estimated parameter will also be distributed with a variance that depends on the input data. For unbiased estimators there exists a theoretical lower limit for the variance of the estimated variable which is described by the CRLB, equation 2.33. Applied to spectral x-ray imaging, the use of the CRLB was suggested in the literature as a measure of basis material noise in the decomposition [Roessl2006]. Optimal spectral separation by a proper choice of THLs will result in a minimized CRLB. Thereby, the CRLB depends on the incident spectrum, the spectral characteristics of the used detector system and also significantly changes for various object compositions and sizes.

The `PcDetector` class offers a basic algorithm that uses the CRLB to optimize the number and positions of thresholds for a PCD. First, an incident x-ray spectrum needs to be selected. Then, a choice of spectral basis functions is made and the magnitude of the line-integrals is set to the values that are relevant for the imaging application. Then, the algorithm iterates over possible combinations of threshold settings and calculates the CRLB for the defined line-integrals. Since the CRLB is equal to the variance of the line-integrals it can vary by several orders of magnitude between different basis materials, especially when using a photoelectric effect and Compton effect basis. Therefore, the average of the relative basis material noise is calculated in each threshold configuration:

$$\overline{\mathrm{CRLB}}_{\mathrm{rel}} = \left\langle \frac{\sqrt{\mathrm{CRLB}_a}}{a} \right\rangle_A , \quad a \in A. \tag{5.6}$$

In this notation, A is the complete set of basis material line-integrals that are of interest for the specific imaging task and $\langle \cdots \rangle_A$ denotes the average over all discrete values $a \in A$. The changes in order of magnitudes are mitigated by taking the square root of the CRLB and normalizing to the line-integral values. The remaining task is to optimize $\overline{\mathrm{CRLB}}_{\mathrm{rel}}$ with respect to the set of all possible energy thresholds thl of the detector:

$$\mathrm{THL}_{\mathrm{opt}} = \arg\min_{thl} \overline{\mathrm{CRLB}}_{\mathrm{rel}}. \tag{5.7}$$

Since the square root of the variance is the standard deviation, the relative CRLB from equation 5.6 corresponds directly to the observed SNR in basis material images. Equation 5.7 therefore maximizes the SNR.

Listing 4 shows the code for the `PcDetector` framework used to optimize a two-bin PCD imaging system. The chosen range of line-integrals spans a range of $5-30$ cm PMMA and $2-8$ cm PVC which are then converted to values in a photoelectric effect / Comptpon effect basis. For reasons of simplicity and to underline the general approach used by the framework, the lower threshold is kept fixed at 20 keV where only the higher threshold is varied.

```
1         res = 'realistic'
2
3         # Basis material calibration range:
4         dPmmaCal = np.linspace(5.,30., 5, True)[:,np.newaxis]
5         dPvcCal = np.linspace(2., 8., 5, True)[:,np.newaxis]
6         lineIntegrals = np.array([calc_A_PC(d_pmma_cal,
           ↪  d_pvc_cal)]).reshape((2,)+d_pvc_cal.shape).round(2)
7         f = np.array([f_ph(E), f_c(E)])
8
9         th0  = 20.
10        crlb = []
11        TH   = []
12        for th1 in np.arange(th0+10., 101., 1.):
13            TH.append([th0,th1])
14            det = PcDetector(energyResponse=res, thl=[th0, th1],
               ↪  thlSampling=eSampling, sensorThickness=dSens)
15            crlb.append((np.sqrt(det.CRLB(s, lineIntegrals,
               ↪  f))/lineIntegrals).mean(axis=(1,2)))
```

Listing 4: Example of CRLB calculation for a specific range of basis material line-integrals in a two-bin PCD system. The lower threshold is fixed at 20 keV while the upper threshold is varied.

Therefore, the resulting values of $\overline{\mathrm{CRLB}}_{\mathrm{rel}}$ represent a function that only depends on the high threshold. These curves are plotted in figure 5.4 for the two spectral basis functions. An ideal energy response and a realistic one with charge-sharing and escape are investigated separately. On each of the curves the cross sign marks the position of the optimal upper threshold. To achieve optimal spectral separation, the required position of the upper THL changes from 68 keV to 73 keV. Overall, a trend towards larger basis material noise is observed for the realistic response function which is generally true for PCDs affected by charge-sharing and other spectral distortions. The spectral overlap in these cases is significantly

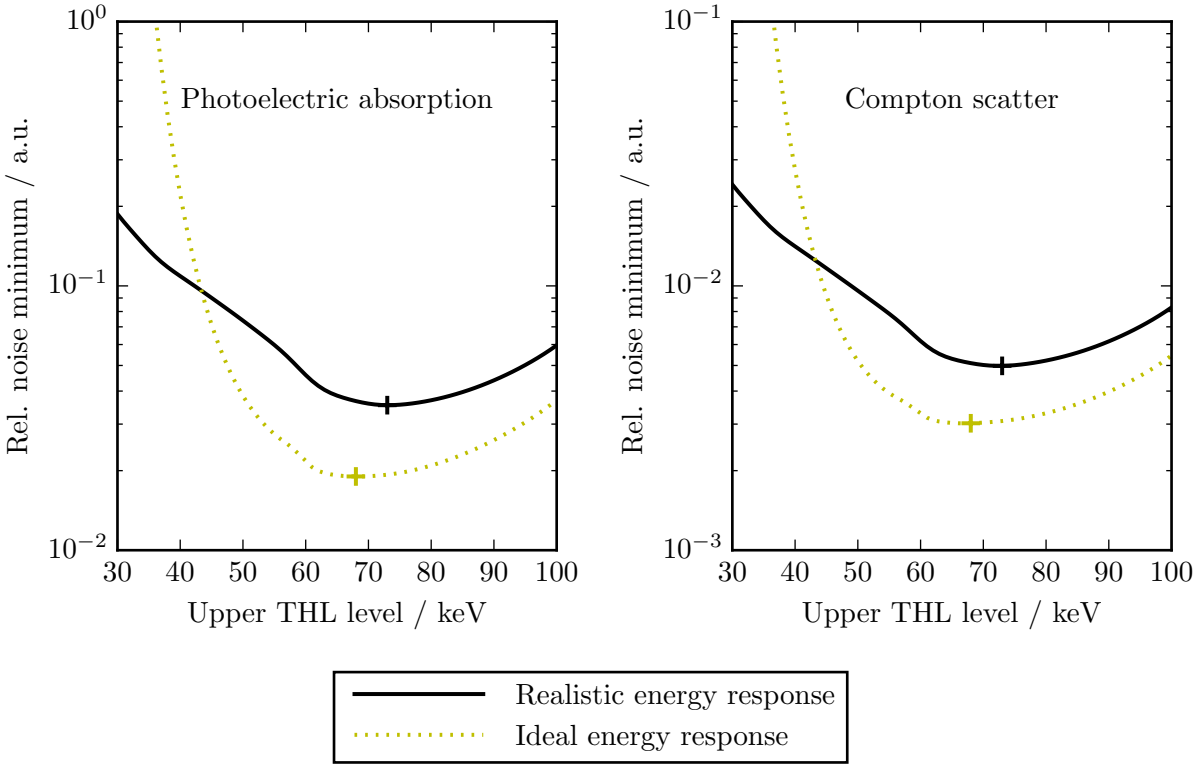

Figure 5.4: **Determination of optimal energy threshold location using the CRLB.** The graphs show the minimum statistical noise to be expected over the complete range of basis material line-integrals for an ideal and a realistic energy response function. For simplicity, a PCD system with two thresholds was considered in this case where the location of lower threshold was fixed at 20 keV. In both basis materials and response functions, the optimal position of the upper thresholds is marked by the cross along the curves. This example directly shows that the optimal choice of energy bins strongly depends on the behavior of the imaging system.

greater than in idealized cases, leading to a larger amount of statistical noise in the basis material images. Only when the upper thresholds approaches the lower one and the width of the energy bin becomes very narrow, charge sharing seems to improve the noise performance. This result can be explained by noticing that for the chosen magnitude of line-integrals, almost no primary photons will be left in the low energy bin and therefore an ideal detector will have virtually no spectral information to perform the decomposition and the basis material noise rises quickly. With charge-sharing present, the counting statistic in the low bin is considerably larger since some of the high-energy photons are registered in the low bin. In such extreme cases, better counting statistic can outweigh poor spectral separation and result in reduced basis material noise.

During the further course of this thesis, this approach has been used several times to optimize the settings

for both simulation as well as experimental studies. Since the details of the performed simulations and the available experimental set-ups vary strongly, the appropriate parameters and results of the threshold optimization will be discussed briefly in the sections where they have been performed.

Simulation of PCD images using digital phantoms

Besides a model for the spectral response of PCDs and its application to optimizing spectral separation, the simulation framework also needs to implement functionality to obtain photon-count images of digital phantoms. This feature is realized by the `getImage` method of the `PcDetector` class. Figure 5.5 shows a flow chart of the `getImage` method to outline the basic principle how the photon-count image data is simulated within the presented framework. Prior to calling `getImage`, the line-integrals for each basis material contained in the phantom have to be calculated for each pixel of the virtual PCD. This can be done for instance using a 3D phantom and a tomographic forward projection to simulate a CT acquisition. The first step of the image simulation is then to calculate the energy-dependent transmission of x-rays through the phantom on a pixel-by-pixel basis using the supplied set of spectral basis materials and line-integrals. The following steps are performed for each energy bin of the `PcDetector` object separately. Using the source spectrum together with the bin sensitivity function the effective spectra are calculated as explained in section 5.1.

Applying the pixelwise transmission values to the effective spectra and summing over all energies contained in the spectrum, the expectation value of the photon counts is obtained for each pixel. In the case of a PCD, summing is valid to calculate the expected signal strength since every photon registered by the detector is equally weighted due to the energy discrimination process (c.f. section 3.2.2). The last step consists of drawing a Poisson random variable for each pixel using the expectation value for each pixel. Note that other systematic effects (threshold distribution, drift, ...) that result in different photon count numbers per pixel are regarded by the pixel-specific bin sensitivity function.

Following this recipe, the two most striking features of PCDs are implemented by the simulation framework, namely equal weighting of all photon within an energy bin regardless of their energy and a Poisson noise distribution.

Sample code for the simulation of images using a human radiographic thorax phantom is shown in listing 5. The parameters for the source spectrum are the same as defined under listing 2. The sample application compares images obtained with a detector having an uniform threshold distribution over the complete pixel matrix compared to a finite distribution around a mean value of $40\,\mathrm{keV}$. Both detectors

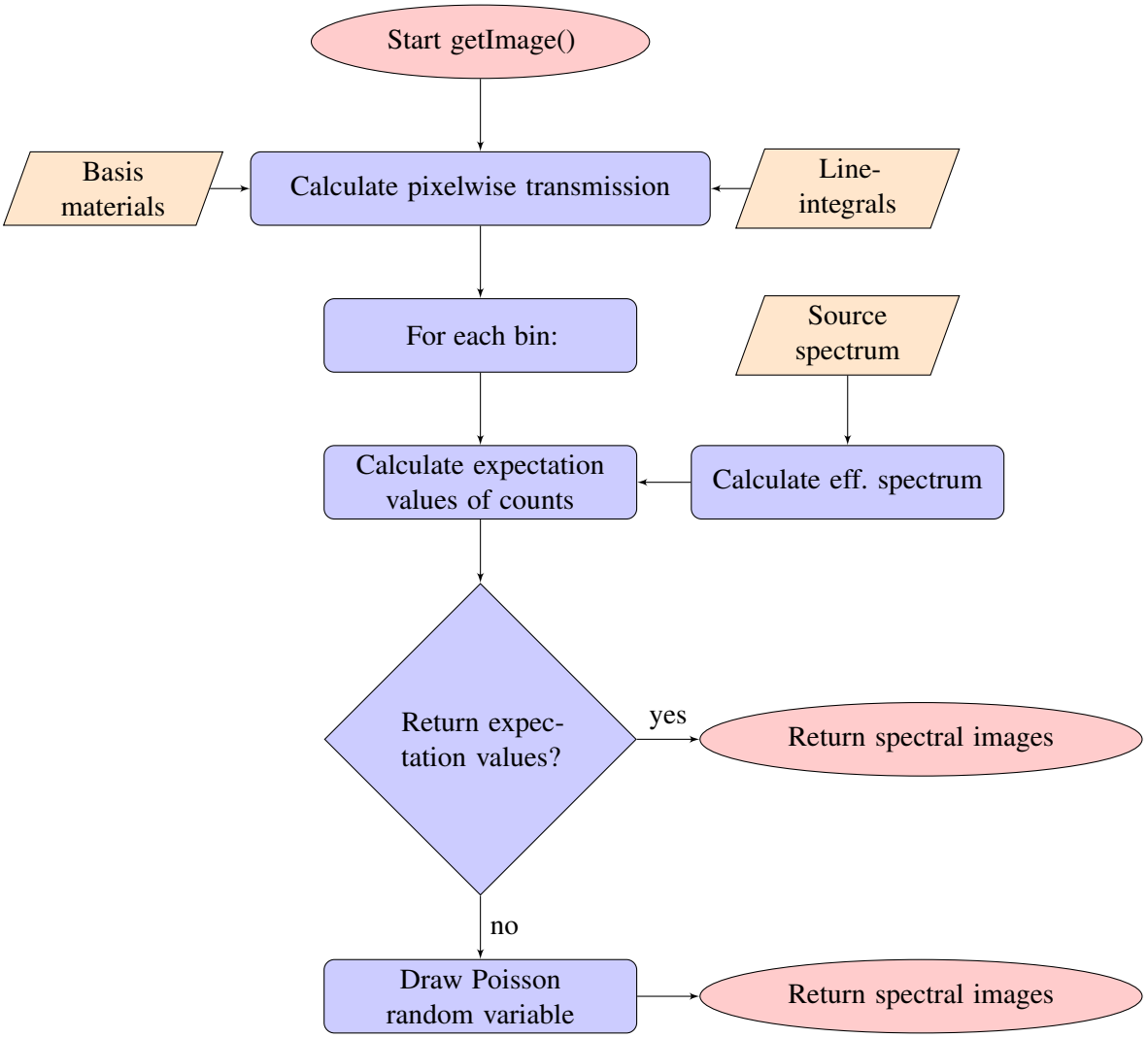

Figure 5.5: **Flow chart of the `getImage` method from the simulation framework.** In a first step, the energy-dependent transmission of the phantom is calculated using the user-supplied basis-materials and line-integrals. Subsequently, an effective spectrum is calculated for each energy bin using the assumed source spectrum and the detector's spectral properties. Combination of the effective spectra and transmission values according to eq. 2.24 yields expectation values for the spectral counts in each pixel. To facilitate Monte-Carlo simulations, Poisson random variables may be drawn and returned using these expectation values.

are assumed to be subject to charge-sharing and escape photons. Besides the number of counts in the presence of the phantom, flat-field images to normalize the data are also simulated.

Figure 5.6 shows the negative logarithm of the simulated images after flat-field correction. Increased

```
f = np.array([mu_bone, mu_tissue]) # spectral basis functions
A = chest_phantom()    # basis material line-integrals
A0 = np.zeros_like(A) # zero-valued line-integrals for flat-fields

det = PcDetector(shape=A[0].shape, energyResponse='realistic',
 ↪  sensorThickness=2., thl=np.array([40.,]), thlDistributionSigma=0.,
 ↪  thlSampling=eSampling)

cts_ref = det.getImage(s, A, f)[:,:,0] # counts registered with phantom
ff_ref = det.getImage(s, A0, f)[:,:,0] # counts registered in flat-fields
img_ref = -np.log(cts_ref.astype(np.float)/ff_ref)

det = PcDetector(shape=A[0].shape, energyResponse='realistic',
 ↪  sensorThickness=2., thl=np.array([40.,]), thlDistributionSigma=10.,
 ↪  thlSampling=eSampling)

cts = det.getImage(s, A, f)[:,:,0]
ff = det.getImage(s, A0, f)[:,:,0]
img = -np.log(cts.astype(np.float)/ff)
```

Listing 5: Simulation of PCD images using a pre-defined description of the phantom line-integrals and a `PcDetector` object. The code generates photon counts for both flat-field and object measurements.

image noise can be observed in (B). This observation is typical for PCDs with a finite threshold distribution. Different to energy-integrating detectors, the varying thresholds lead to additional changes in the effective spectra detected by each pixel. These variations can be interpreted as different absorption caused by the sample and therefore different intensity would be obtained in each pixel even with a perfectly homogeneous sample. Since normally no energy thresholding exists in energy-integrating detectors, every pixel sees the same spectrum in the flat-field. In such detectors inter-pixel differences in the detector signal mainly arise due to gain variations of the ADC. Therefore, a single flat-field[1] is usually enough when using integrating detectors to compensate these effects and results in uniform images.

When operating PCDs, a simple flat-field correction typically yields sub-optimal results. Different effective spectra in the flat field and the object image are not accounted for in this way and often result in pronounced systematic signal differences between pixels. This manifests itself e.g. in strong rings artifacts after CT reconstruction. Hence, several approaches to compensate the threshold distribution in

[1] Also called 'gain-correction'. This approach is only exactly valid in the linear regime of the dose-response curve.

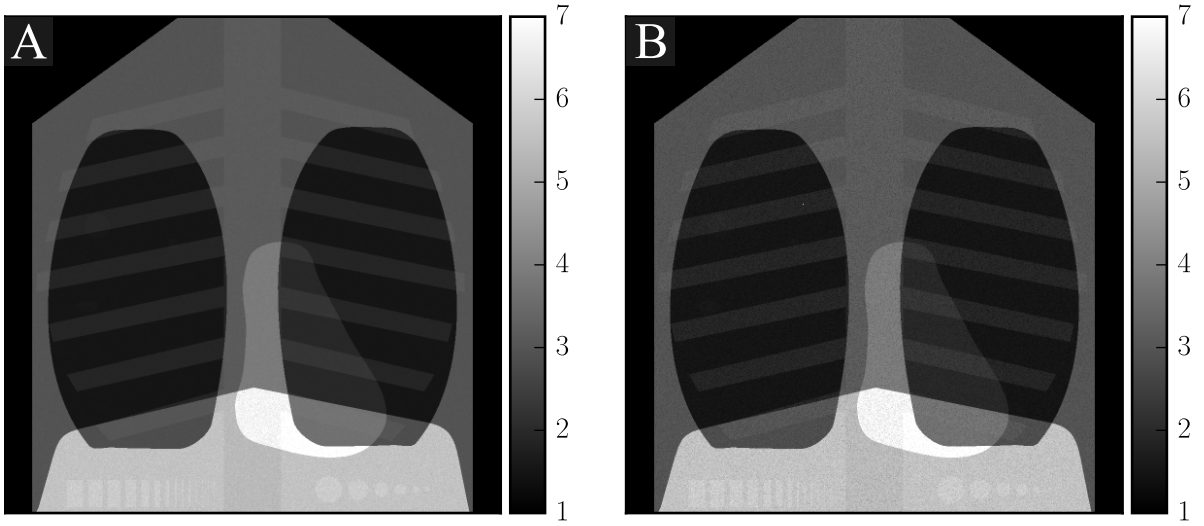

Figure 5.6: **Simulated PCD images of a thorax radiography phantom.** Image (A) shows the thorax phantom obtained with a strictly uniform energy threshold of 40 keV across all pixels. Thus, the noise in the image is exclusively due to the Poisson distribution of the registered photons. In contrast, (B) shows the impact of a spatially varying threshold distribution across the detector pixels. Therefore, each pixel effectively sees a slightly different spectrum resulting in additional noise contributions.

PCD-based imaging applications have been suggested and investigated in the literature [Jakubek2007, Vavrik2011, Persson2012]. Another elegant way to tackle this problem is making use of spectral material decomposition on a pixel-by-pixel basis. This approach will be discussed in the following chapters.

6 Development of a semi-empirical forward-model for material decomposition using spectral photon-counting data

In chapter 2 the basic physical principles and methods of spectral x-ray imaging have been introduced. Especially if the emitted source spectrum and the energy response of the detector are well known, decomposition into an arbitrary set of spectral basis materials is possible. The number and choice of basis materials is then only limited by the available number of energy bins on the PCD. However, measurements of spectral characteristics are typically very cumbersome and time-consuming. Even further, the behavior of the x-ray source and the detector system are subject to change over time due to external influences like temperature or aging of the device components. Therefore, these quantities need to be measured again periodically. Especially for medical applications in clinical routine, periodic re-calibration of the complete imaging system becomes a very challenging task.

A set of empirical methods has been developed to circumvent the requirement of exact knowledge of all spectral quantities. The two most widely used and investigated methods relying on experimental calibration measurements are discussed in section 2.3 of the theory part. Drawbacks of these methods comprise an excessive amount of noise in basis material images when used in over-determined systems[1] or a huge amount of required calibration measurements[2]. Accordingly, an estimator for the basis material composition of the investigated object should be compatible to MLE-based methods to guarantee optimal noise performance and should require a minimum of calibration effort.

During this thesis, a new spectral forward-model based on a simplified yet accurate model for the expected number of photon counts in the presence of beam-hardening was developed and implemented within a MLE [Ehn2017]. The goal was to develop a semi-empirical forward-model based on physical model of x-ray attenuation to minimize calibration efforts to a small number of calibration measure-

[1] Using polynomial-based methods with a larger number of energy bins than basis materials.
[2] For the so-called A-table method, this often amounts to more than 1000 measurements per calibration.

ments[3] that can be used on a regular basis in research set-ups as well as in a clinical environment. Pre-clinical research and material science can also benefit as the operating parameters (e.g. tube voltage/loading, geometry, ...) are varied a lot between different studies and therefore a fast and reliable calibration of the systems is necessary. The following sections will first describe the general concept of the forward-model and then investigate the performance of the estimator in a two-material decomposition with respect to its bias and variance. Simulations of a CT acquisition of a human phantom will also be shown.

6.1 Derivation of the Polychromatic Beer-Lambert forward-model

With knowledge of all spectral parameters, the exact number of photon counts transmitted through a sample of known composition and registered in energy bin i can be calculated from equation 2.24. In case of a polychromatic spectrum, attempts are often made to define a mean energy $\overline{E_i}$ describing the absorption in a specific measurement:

$$\overline{E_i} = \frac{\int_0^\infty \Phi_{\text{eff},\,i}(E) E \mathrm{d}E}{\int_0^\infty \Phi_{\text{eff},\,i}(E) \mathrm{d}E}, \quad i = 1...N. \tag{6.1}$$

For small object sizes[4] and high energies, the logarithm of the number of photon counts $\mathcal{C}_i$ approximately shows linear dependency on the basis material line-integrals A_α:

$$\ln \mathcal{C}_i \sim \sum_\alpha f_\alpha(\overline{E_i}) A_\alpha, \quad i = 1...N. \tag{6.2}$$

This can be written as the well-known Beer-Lambert law for x-ray attenuation considering the limit of a monochromatic beam. When the object size becomes smaller and the x-ray spectrum broadens especially with the presence of low energies in the primary beam, deviations from the linear behavior of $\ln(\mathcal{C}_i)$ become more prominent and equation 6.2 no longer holds true. The non-linearities give rise to beam-hardening effects in radiography and especially in CT. Unfortunately, a fully analytic treatment of this process is difficult to accomplish. In the available literature on beam-hardening it was shown

[3] Typically requiring considerably less than 100 measurements

[4] Or more general for objects with low x-ray absorption in the relevant part of the spectrum

that the attenuation properties of the sample can be described by the sum of two separate exponential functions [VandeCasteele2002, Alles2007] with a modified Beer-Lambert expression of the form

$$\mathcal{C}_i \sim A\mathrm{e}^{-\mu_i d} + B\mathrm{e}^{-\tilde{\mu}_i d}, \;\; i = 1...N, \tag{6.3}$$

where A, B are constants to describe the photon flux, d denotes the basis-material line-integrals, μ_i describes the attenuation in the near-linear regime (cf. eq. 6.2) and $\tilde{\mu}_i$ is a correction that incorporates beam-hardening occurring in energy bin i. Incorporating this approach, we presented an estimator in [Ehn2017] that uses a series of multiple exponential terms with correction coefficients for each spectral basis material.

Further generalizing this idea, instead of using a single mean energy $\overline{E_i}$, it is possible to describe the polychromatic spectrum as discrete sum of a finite and small number K of dominant energies $\hat{E}_{i,\,k}$ rather than a continuous function of photon energy:

$$\Phi_{\mathrm{eff},\,i}(E) = \sum_{k=1}^{K} \Phi_{i,\,k}\, \delta(E - \hat{E}_{i,\,k}), \; i = 1...N, \tag{6.4}$$

where $\delta(E)$ is the Dirac δ-distribution and $\Phi_{i,\,k}$ is the intensity attributed to each of the dominant energy levels. The quantity $\Phi_{i,\,k}$ needs to be chosen in a way that conserves the total photon flux arriving at the detector. Inserting a spectrum of this form into equation 2.24 we obtain the proposed forward-model for the number of photon counts $\mathcal{C}_i$ in each energy bin i:

$$\mathcal{C}_i = \sum_{k=1}^{K} \Phi_{i,\,k} \cdot \mathrm{e}^{-\sum_{\alpha=1}^{M} A_\alpha f_\alpha(\hat{E}_{i,\,k})}, \; i = 1...N, \tag{6.5}$$

where A_α is the line-integral of the coefficient of basis material α and f_α is the associated basis function. Depending on the sample size and composition as well as on the incident x-ray beam quality, usually a small number of $K \leq 4$ energy terms can be chosen. Only for very strongly attenuating objects which might also contain high-Z elements, a larger number of terms in the equations 6.4 and 6.5 needs to be regarded. The relation between K and the achieved quantitative accuracy of the forward-model predicting the number of recorded photon counts will be investigated in a later section.

The system parameters for each energy bin i are contained int the set $p_i = \{\Phi_{i,k}\,,\ \hat{E}_{i,k}\}$ consisting of a number $s = 2\,K$ elements. Since $s \leq 10$ is valid in most cases, the forward-model can easily be calibrated with the use of simple phantom measurements. A calibration procedure for the decomposition into a photoelectric effect and Compton scattering basis will be discussed in the following section.

For the remainder of this thesis we will refer to model 6.5 as the PLB approximation. It has already been summarized in section 2.3 how a forward-model of this type can be numerically inverted by means of a MLE in order to yield the basis material line-integrals. Therefore the number of available energy bins must be at least equal to or greater than the number of basis materials, i.e. $N \geq M$.

6.2 Calibration of system parameters for decomposition into photoelectric and Compton basis

At least s calibration measurements are needed to calibrate the system parameters in the model function prior to basis material decomposition. In principle, any combination of basis materials may be chosen as long as they are linearly independent [Lehmann1981]. In the absence of heavy elements for example in body tissues without contrast agents, a set of two basis functions is mostly sufficient to describe the measured attenuation. In principle, the dimensionality of the attenuation basis would be 3 even for such cases where absorption edges can be neglected since three interaction processes have to be accounted for[5]. However, in almost all clinical applications with the exception of mammography and many NDT applications, the x-ray spectrum is pre-filtered to contain only energies above 30 keV to reduce radiation exposure and minimize beam-hardening artifacts. At these energy levels the contribution of coherent scattering to the total attenuation can be mostly be neglected as a two-material basis is capable of parameterizing the attenuation with sufficient accuracy[6]. For a two-material decomposition, common choices for the basis are either a combination of distinct materials, e.g. acrylic plastic (PMMA) and aluminum (Al) to mimic the absorption of soft tissue and bone respectively [Lehmann1981, Alvarez2011], or direct decomposition into contributions due to photoelectric absorption and Compton scattering [Roessl2007, Schlomka2008].

Besides being the natural basis from a physical point-of-view, the photoelectric/Compton basis is considered relevant as it enables direct quantitative evaluation of the object's composition in the form of electron density and effective atomic number. In medial applications this information can be used to

[5] Photoelectric absorption, incoherent (Compton) scattering and coherent (Rayleigh) scattering, cf. section 2.1.

[6] The accuracy is acceptable when the effects of noise inherent to all x-ray imaging applications outweigh the model bias.

characterize different pathological processes such as kidney stones or atherosclerotic plaque, perform lung perfusion tests and is also important in planning of radiation treatment. Besides that, any other material basis of interest can easily be derived from these values. We will therefore focus on how a direct decomposition into these two basis functions can be accomplished using the PLB model. This can be achieved using a calibration procedure that is routinely practicable in a clinical environment.

Most conveniently, calibration is done using polymer materials of exactly known elemental composition and mass density such as PMMA and PVC as reference materials. Therefore, the line-integrals of the photoelectric and Compton coefficients can be calculated as

$$\begin{aligned} A_{\mathrm{C}}^{\mathrm{cal}} &= \sum_{\alpha} N_{\alpha}^{\mathrm{eff}} \rho_{\alpha} d_{\alpha}, \\ A_{\mathrm{Ph}}^{\mathrm{cal}} &= \sum_{\alpha} C_{\mathrm{Ph}} N_{\alpha}^{\mathrm{eff}} (Z_{\alpha}^{\mathrm{eff}})^{3.8} \rho_{\alpha} d_{\alpha}, \\ \alpha &= \mathrm{PMMA},\ \mathrm{PVC}, \end{aligned} \tag{6.6}$$

where ρ_α and d_α are the mass density and thickness of material α. In fig. 6.1 (a), the black dots show a calibration scheme with 10×10 steps using PMMA from $0...35$ cm and PVC from $0...5$ cm. After the transformation of these points into their photoelectric and Compton coefficients according to eq. 6.6, the appropriate values $A_{\mathrm{C}}^{\mathrm{cal}}$ and $A_{\mathrm{Ph}}^{\mathrm{cal}}$ used to calibrate the system parameters in eq. 6.5 are obtained as indicated by the black dots in fig. 6.1 (b).

To perform the calibration of bin i, the NLL function in eq. 2.27 is rearranged to become a function of the system parameters p_i. Subsequently, the parameters were determined using a MLE. In order to increase numerical stability in the determination of p_i and to assure physically plausible solutions, several constraints on the p_i were incorporated to regularize the cost functions:

$$\begin{aligned} \hat{E}_{i,\,k} &> 0 \\ \Phi_{i,\,k} &\geq 0 \\ \sum_{k=1}^{K} \Phi_{i,\,k} &= c_{\mathrm{i}}(A_{\mathrm{Ph}} = 0, A_{\mathrm{C}} = 0) \end{aligned} \tag{6.7}$$

The first constraint makes sure that the model assumes reasonable energies, while the last two conditions conserve the incident photon flux.

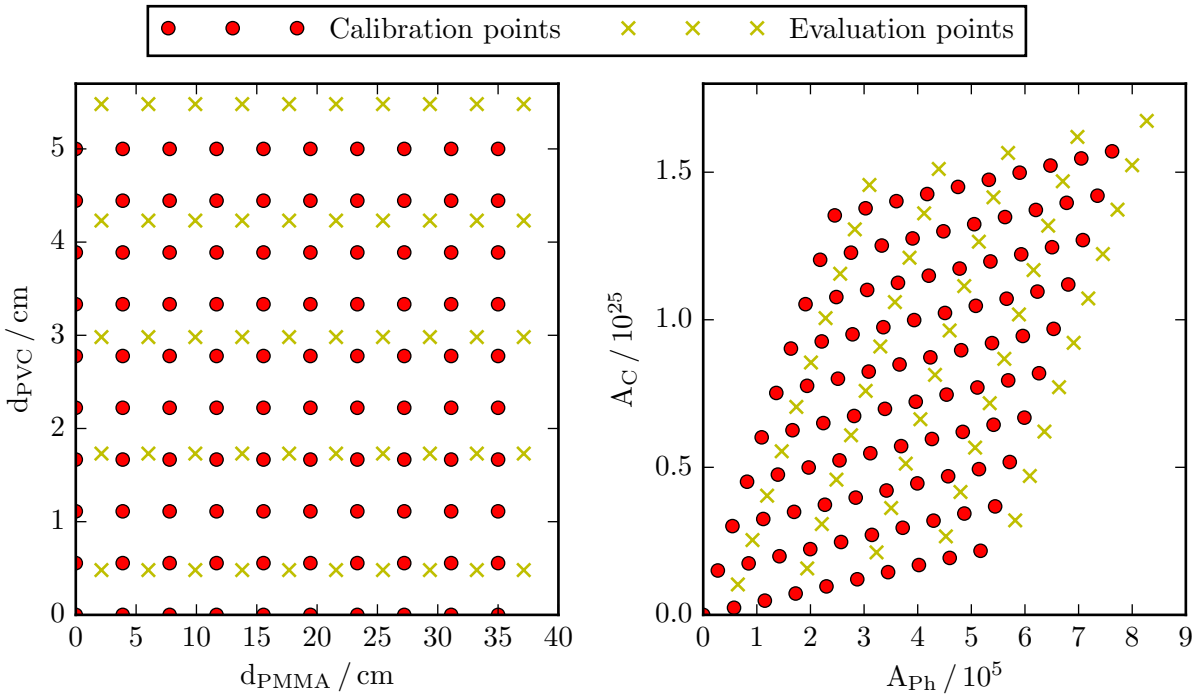

Figure 6.1: **Position and distribution of the line-integrals used for calibration and evaluation of the material decomposition performance.** Calibration points used to determine the system parameters of the PLB equation 6.5 are marked by red dots. The performance of the material decomposition was tested for line-integrals marked by the crosses that do not coincide with calibration data. A calibration with 10×10 steps of PMMA from $0...35$ cm and PVC from $0...5$ cm is shown in the left panel. To enable direct Photoeffect/Compton decomposition, the calibration points are transformed using eq. 6.6 as indicated in the right panel.

6.3 Performance evaluation of the forward-model

The performance of the proposed PLB forward-model was evaluated using Monte-Carlo simulations of calibration measurements and CT acquisitions based on the PCD simulation framework introduced in chapter 5.

The quantum efficiency of the PCD was modeled by the absorption of a 2 mm CdTe sensor. A realistic energy response function (cf. section 5.1) including spectral distortions due to charge-sharing, escape photons and finite energy resolution was used. Gain and offset dispersion across the pixel matrix were neglected since the typically used performance metrics such as the CRLB depend on the effective spectrum and thus can not be evaluated for spatially varying THLs. The CRLB was also used to determine the optimal arrangement of the energy bins as outlined in section 5.2. Therefore, all line-integrals located

on the yellow grid in figure 6.1 were used and the thresholds were varied in order to find the optimal arrangement minimizing the CRLB. A 120 kVp tungsten spectrum with additional filtration of 2 mm Cu was assumed. The obtained settings for a two-bin and a four-bin PCD are given in table 6.1.

2-bin PCD		**4-bin PCD**			
THL 1	THL 2	THL 1	THL 2	THL 3	THL 4
15 keV	66 keV	15 keV	52 keV	64 keV	79 keV

Table 6.1: **Optimal energy threshold settings for the simulated acquisitions in a two-bin (left part) and four-bin (right part) PCD.**

Monte-Carlo-type simulations were realized by calculating a Poisson random variable for the recorded number of photons hitting the virtual PCD detector. Scattered radiation produced by the phantom was neglected for the quantitative evaluation of the forward-model itself.

In this section a base-line for the quantitative performance of the proposed estimator is established. We will first focus on the photon count numbers predicted by the PLB forward-model and then investigate the quantitative accuracy of basis material decomposition based on the PLB approximation. This section will be concluded by presenting simulations of spectral CT acquisitions of a clinical phantom.

Accuracy evaluation of the polychromatic Beer-Lambert model

In a first step, the quantitative accuracy of the PLB forward-model itself is investigated. This was done simulating the attenuation of soft tissue with a composition as defined in report number 44 of the ICRU. Using the PCD simulation tools, photon counts after transmission through up to 40 cm of soft tissue were simulated as reference values to benchmark the forward-model. The parameters for the assumed x-ray tube are summarized in table 6.2. A single energy threshold located at 15 keV was assumed since beam-hardening effects are to be expected especially for spectra covering a wide energy range. Such effects typically lead to deviations from the linear behavior of the counts on a logarithmic scale.

Anode	Peak Energy	Filter	Total flux
W	120 kVp	0.2 mm Cu	1×10^5 photons/pixel /exposure

Table 6.2: **Imaging parameters used for quantifying the estimator performance**

The expected number of counts predicted by the PLB model was calculated according to eq. 6.5 with different numbers K of exponential terms. For $K = 1$ the PLB equation reduces simply to Beer-Lambert's law which is also included in the evaluation. The accuracy of the proposed forward-model was quantified using the relative bias of the predictions normalized to the simulated reference values:

$$\text{Rel. bias} = \left| \frac{\mathcal{C}_i^{\text{GT}} - \mathcal{C}_i}{\mathcal{C}_i^{\text{GT}}} \right|, \tag{6.8}$$

where $\mathcal{C}_i^{\text{GT}}$ is the ground-truth for the number of photon counts as defined by equation 2.24 in section 2.3.

Figure 6.2 shows that the developed PLB forward-model is able to predict the expected number of photon counts within an accuracy in the order of 0.1 % even for larger object sizes where beam-hardening effects become more prominent. A simple monochromatic Beer-Lambert model would lead to deviations of up to 30 % in the investigated scenario. Towards smaller values of the line-integrals, the bias decreases further and is at a minimum when no object is in the beam. This is also a result of the regularization incorporated into the fit of the system parameters according to equation 6.7.

Acceptable results with accuracy better than 1 % are already obtained using only two exponential terms. However, due to spectral distortions like charge-sharing and pile-up the effective spectra measured by each energy bin will eventually cover the complete energy range emitted by the x-ray source. For such cases, the accuracy can be largely increased by taking more energy terms into account as indicated by the curves in right panel of figure 6.2. In turn, to guarantee numerical stability of the fitting process and to minimize the required number of calibration measurements it is beneficial to keep the number of terms in the PLB model as low as reasonably possible. For this scenario, $K = 3$ terms were therefore selected and all subsequent simulation studies presented in this chapter have been performed using this setting.

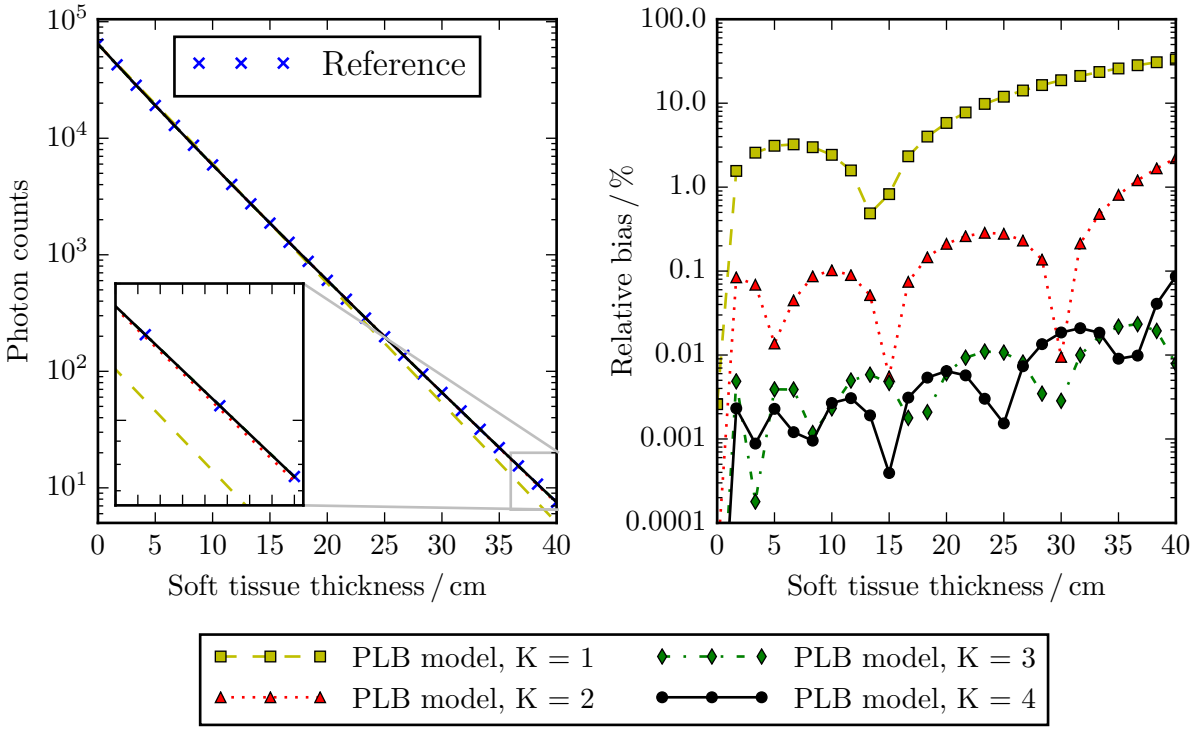

Figure 6.2: **Quantitative accuracy of the PLB forward-model predicting the transmission of photons through soft tissue (ICRU44).** In the left panel the ground truth for the photon counts according to eq. 2.24 is shown by black dots along with the expected numbers using the proposed model with varying numbers of exponential terms. The right panel shows the relative bias calculated via eq. 6.8. The proposed model is capable of predicting the photon count numbers in the presence of beam-hardening with a deviation of less than $0.1\,\%$ from the expected value. A number of $K = 3$ energy terms is usually sufficient to achieve this high accuracy.

Bias and noise performance in PLB-based material decomposition

The quantitative accuracy of a material decomposition into a photoelectric effect / Compton scattering basis obtained by combining the PLB forward-model with a MLE-based determination of basis material line-integrals was investigated under a realistic imaging scenario. Thereby, simulated measurements of line-integrals corresponding to the data points marked by the yellow grid in figure 6.1 were obtained and decomposed. Prior to decomposition, the model was calibrated using simulated calibration measurements covering a range of $0\,\text{cm}$ to $35\,\text{cm}$ PMMA and $0\,\text{cm}$ to $5\,\text{cm}$ PVC with different number of calibration steps per material as discussed below. The line-integrals used during the calibration process and the decomposition were deliberately chosen not to coincide with each other. Besides that, the

evaluation range in the photoelectric / Compton space was extended slightly with respect to the initial calibration range to assess the extrapolation properties of the PLB model. For the incident spectrum the same values given in table 6.2 have been used where only the total photon flux was increased to 1×10^6 photons/pixel /exposure.

Statistical information about the MLE performance was obtained by simulating and decomposing each point 1×10^4 times. From this set of measurements the relative bias and the variance were calculated. In this case the relative bias was defined as

$$\text{Rel. bias} = \left| \frac{\langle A_{\text{PLB}} \rangle - A_\alpha}{A_\alpha} \right|, \tag{6.9}$$

with the mean decomposition result $\langle A_{\text{PLB}} \rangle$ yielded by the PLB estimator over the 10×10^4 trials and the true values A_α.

One of the most important assets of the PLB forward-model is the small number of calibration measurements required. Therefore, figure 6.3 investigates the quantitative performance of the proposed method calibrated with only nine (3×3) measurements of known basis material line-integrals. A typical scenario of a four-bin PCD was considered. The x-axis indicated the position of each line-integral in the A-plane shown in figure 6.1. The PMMA components of the decomposed samples repeat with a period of ten measurements, while the PVC component was kept constant for each series of 10 points and increased consecutively. The detector images were simulated with the given PVC/PMMA composition and the decomposition into photoeffect/Compton components was done subsequently. The curves for the bias demonstrate that the bias for both materials does only slightly exceed $0.1\,\%$ of the true values. This is also true for line-integrals that lie outside of the initial calibration range. The statistical noise introduced during the decomposition exceeds the bias nearly throughout the complete range of line-integrals. For larger line-integrals, the bias is smaller by at least one order of magnitude compared to the noise. Note that the statistical noise also behaves according to the CRLB as expected for an asymptotically unbiased MLE-based estimator. This observation is also in good agreement with the results published for other MLE-based decomposition methods [Roessl2009, Alvarez2011].

The small-scale oscillations seen in the bias can be understood when compared to the root-mean-squared error of the photon counts predicted by the forward-model (figure 6.3, black dashed line). The local minima and maxima seen in the bias curves tend to follow the inaccuracies of the predicted photon counts which are propagated into the decomposed basis-material line-integrals. However, even the largest fluctuations that are observed are only in the order of $0.1\,\%$ and can therefore safely be neglected

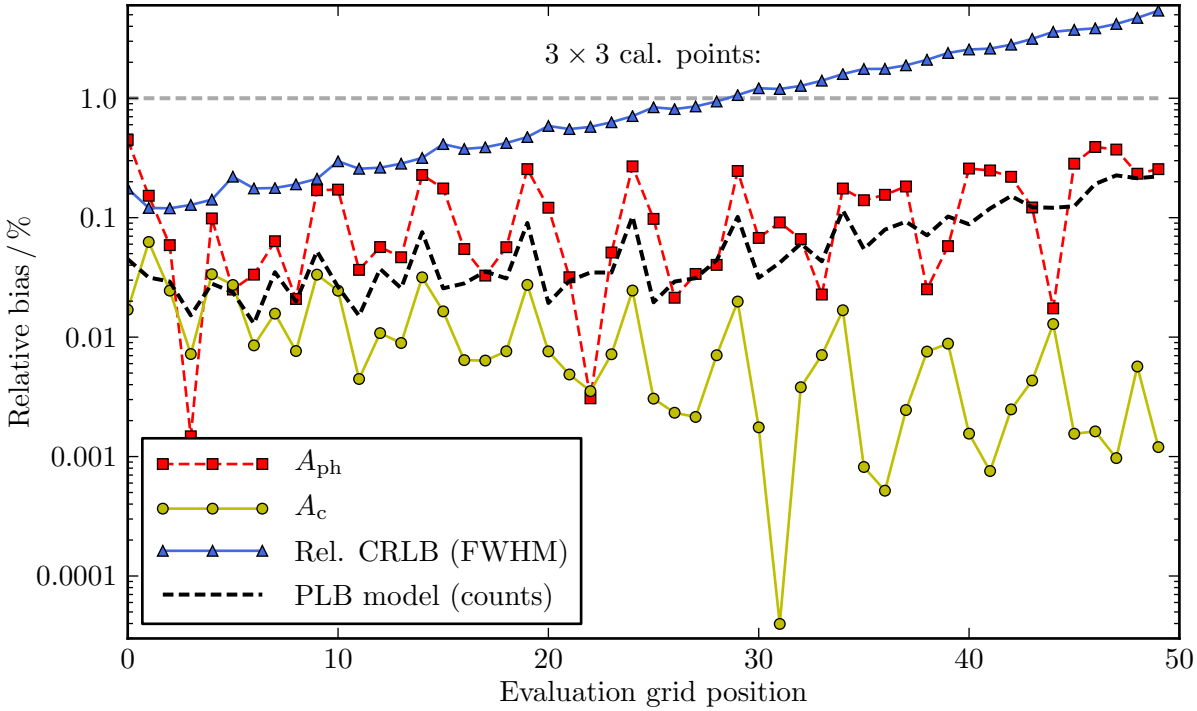

Figure 6.3: **Relative bias and variance of the PLB estimator calibrated with 9 measurements and four PCD energy bins.** Even for this small number of calibration measurements, the maximum bias observed in the photoelectric component is only slightly above 0.1 %. Compared to this, the influence of the statistical error produced by the estimator is approximately one order of magnitude larger. The statistical error here refers to the FWHM of noise in basis material images as predicted by the CRLB. Note that the small-scale fluctuations of the bias correspond to the accuracy of the photon count numbers obtained from the PLB forward-model (black dashed line, averaged over all four energy bins).

for any practical application. Hence, these considerations show that the developed PLB model yields an effectively unbiased and efficient estimator already for a very small number of calibration points.

Figure 6.4 compares the performance of PLB-based material decomposition in various imaging scenarios regarding the number of calibration measurements and the available energy bins of the PCD. The plot in (A) compares the RMS bias over all line-integrals on the evaluation grid after calibration with an increasing number of measurements. First, the bias of the photoelectric component lies constantly above the corresponding value for the Compton component. This might be explained in part by the fact that the assumption of a two-material basis is an approximation and is only valid when coherent scattering can be completely neglected (c.f. section 2.1). Strictly speaking this assumption is not completely fulfilled considering than e. g. in the case of PMMA, the ration between coherent and incoherent scattering is approximately $1/5$ at an x-ray energy of 40 keV and shifts towards the coherent part when considering

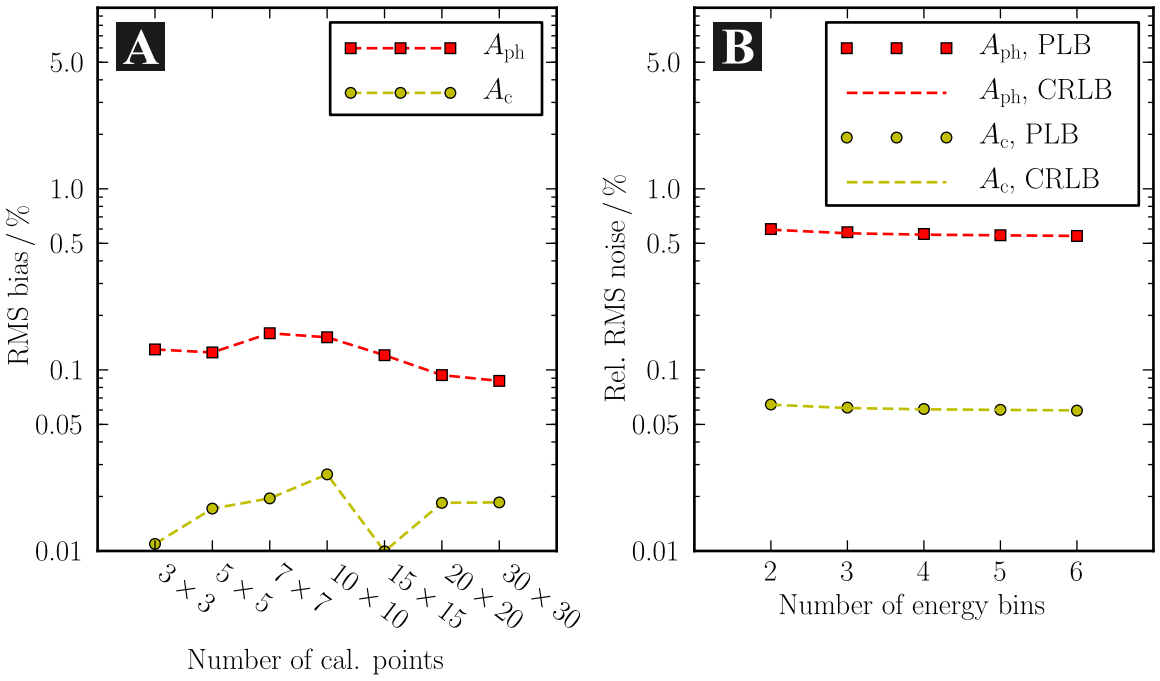

Figure 6.4: **Bias, variance and CRLB in PLB-based two-material decomposition.** (A) shows the bias of both basis material images in dependency on the number of calibration measurements in a four-bin system. Generally, the bias is considerably below 1 % for all investigated cases. Only small improvements are observed for the photoelectric component when the number of calibration points increases. (B) shows the obtained RMS noise averaged over the complete range of investigated line-integrals for different numbers of available energy bins. The forward-model was calibrated with 5×5 steps. In all scenarios, the noise in the PLB estimator achieves the CRLB limit. Note that the values of the bias are significantly lower than the statistical noise.

lower energies or higher chemical elements present in PVC. In such cases, the exponent in the energy dependency of the photoelectric effect can be tuned to include the behavior of coherent scattering[7]. However, as discussed above the bias is still at a reasonably low level in the order of 0.1 % even in the case of the photoelectric basis function. No clear trend can be observed for the bias values when increasing the number of calibration measurements. Both curves show fluctuations in the regions of $0.01\,\% - 0.03\,\%$. Since these values are significantly low, this behavior might well be an artificial effect of a statistical bias when the size of the sample set (10^4) was not large enough yielding a slightly false estimate for the RMS bias.

[7]The value of -3.2 typically stated for the exponent is chosen to fit the photoelectric part only and results in slightly biased parameterization of x-ray attenuation in presence of Rayleigh scattering.

In part (B) of figure 6.4, we present the dependency of statistical noise in basis material images on the number of available energy bins and a calibration using a medium number of 5×5 measurements. The statistical error here refers to the FWHM of noise measured in the basis material images. Additionally, the dashed lines mark the theoretical limit as predicted by the CRLB. The obtained measurements of the noise are essentially equal to the CRLB indicating again that the used estimator is in fact unbiased and effective. The magnitude of noise is only reduced slightly by increasing the number of energy bins. For the photoelectric component, the relative RMS noise was reduced from approximately $0.6\,\%$ for a two-bin detector to $0.55\,\%$ in a 6-bin system. Other work in the literature seems to suggest larger improvements dependent on the number of bins [Alvarez2011, Roessl2006]. However the authors of those studies used idealized energy response functions resulting in well-separated energy bins. In our study we chose a realistic model for the PCD including charge-sharing and other spectral distortions. In this case, overlap between the energy bins diminished the effect of more spectral information.

Phantom simulation study

To demonstrate the potential of the proposed estimator in a clinically relevant imaging task, a polychromatic simulation of an adapted FORBILD phantom [Forbild2016] and subsequent decomposition into the photoelectric and Compton basis was performed. The assumed x-ray exposure parameters are summarized in table 6.3.

Anode	Peak Energy	Filter	Tube loading
W	120 kVp	0.2 mm Cu	160 mA s

Table 6.3: **Tube parameters used for the phantom simulation.**

For the CT simulations, the FORBILD thorax phantom was used [Forbild2016]. The phantom description was modified such that it accounts for the energy-dependent attenuation properties of the various body tissues involved. Therefore, the absorption coefficients were calculated using the composition of body tissues from the reports of the ICRU and the XCOM database.

The acquisition geometry of the simulated fan-beam CT set-up is summarized in table 6.4. An inhouse-developed tomographic projector [Fehringer2014] was used to calculate the line-integrals of the phantoms for each projection angle as well as to perform the FBP reconstruction of the processed data.

For the projection simulation and decomposition, the two-bin PCD configuration from table 6.1 was used. The relevant parameters in the PLB forward-model were calibrated by simulating measurements of 3×3 steps of PVC ($0\,\text{cm} - 10\,\text{cm}$) and PMMA ($0\,\text{cm} - 30\,\text{cm}$), thus fully exploiting the compatibility

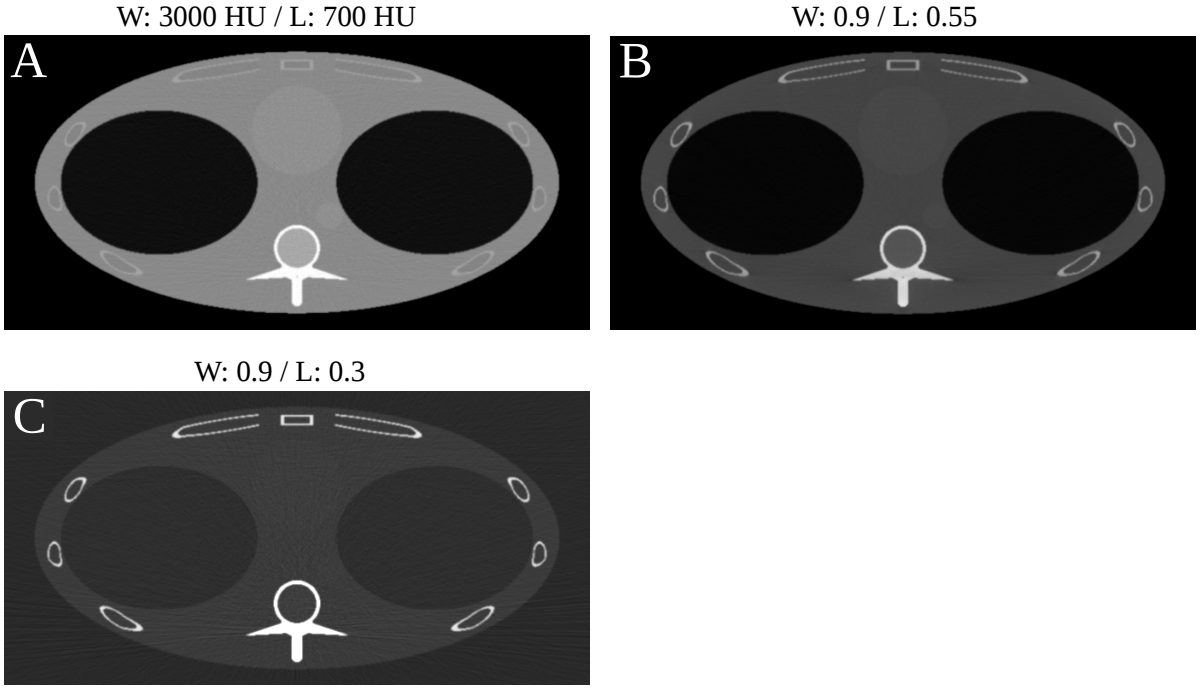

Figure 6.5: **CT reconstruction of the spectral FORBILD phantom.** The polychromatic image shows the reconstruction of the data from the lowest threshold of the photon-counting detector up to the peak energy (a) Window (W): 3000 HU / Level (L): 700 HU. The Compton component (b) and the photoelectric component (c) were reconstructed using the maximum-likelihood decomposition based on the proposed model in a two-threshold system. The Compton image is shown in a window/level setting of W: 1.0 / L: 0.55 relative to the maximum value and the photoelectric image at W: 1.0 / L: 0.3.

of PLB with small calibration efforts.

FOV	SID	SOD	pixel-size	projections per 360°
40 cm	50 cm	50 cm	250 µm	1280

Table 6.4: **CT geometry used for the phantom simulation.** The pixel size is given at the isocenter.

The reconstructed images of the simulation can be seen in fig. 6.5 where a polychromatic reconstruction of the lowest energy threshold data (15 keV) is shown (A) as well as the coefficients for the Compton (B) and the photoelectric basis functions (C). The images correspond to the raw output from the estimator and no post-processing of any kind was applied.

The quantitative accuracy of the proposed method can be seen by looking at the line plots through the photoelectric and Compton images as indicated in fig. 6.6. The result of the decomposed reconstructions

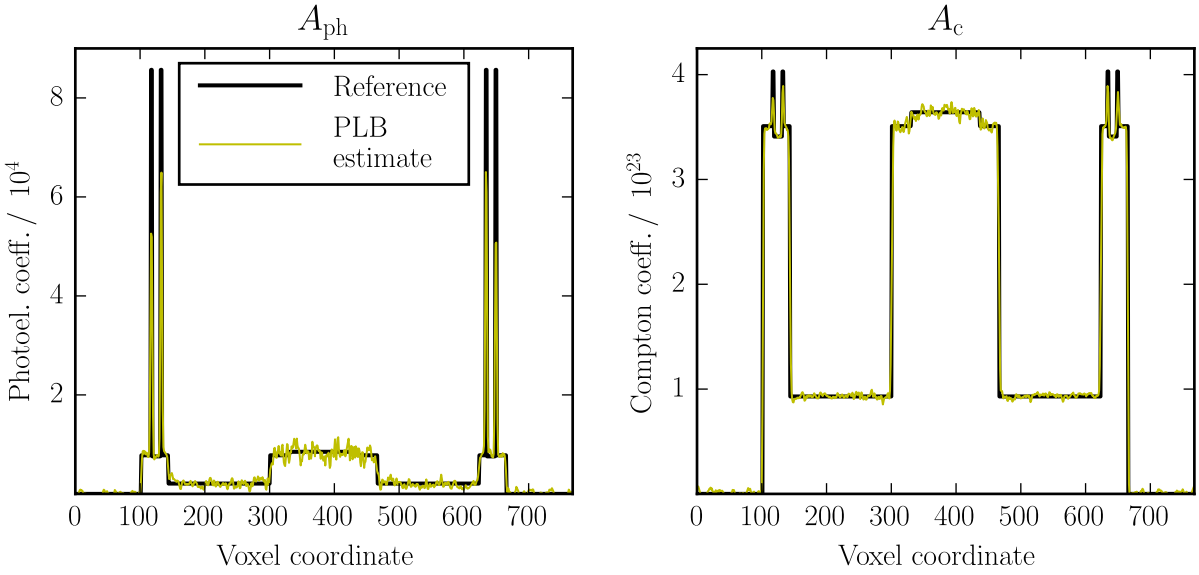

Figure 6.6: **Quantitative evaluation of the simulated and decomposed spectral FORBILD phantom data.** The curves show the values of reconstructed voxels across a line through the rudimentary heart in the phantom. The decomposed and reconstructed images yield good overall agreement with the expected values. Deviations at feature edges can be attributed to partial-volume effects arising in the imaging geometry.

is compared to the ground truth calculated directly from the implemented spectral phantom. In the flat regions of the phantom, the estimator is able to accurately obtain the basis material coefficients. Only at the edges, slight deviations occur due to partial-volume effects arising in the fan-beam geometry.

6.4 Limitations and extensions of the Polychromatic Beer-Lambert model

Although the PLB-based decomposition of spectral PCD data promises high quantitative accuracy with a minimum of required calibration measurements, there are a few limitations of this method that need to be discussed briefly.

Compared to the technique presented in [Roessl2007, Schlomka2008], which is principally compatible with any number of basis materials by its design[8], our proposed approach still relies on calibration measurements. It is to be expected that the surrogate energies $\hat{E}_{i,k}$ determined by the PLB model

[8] Full knowledge of x-ray spectrum and PCD energy response is assumed in these methods.

strongly depend on the materials and magnitude of the line-integrals used in the calibration process. Therefore, the choice of a specific set of basis functions for the decomposition needs to be made prior to the calibration or the imaging application.

Element-specific imaging has attracted a lot of attention in spectral imaging methods over the last few years. For example in a clinical context, the discrimination of various contrast agents based on heavy elements using unique k-edges of the photoelectric absorption opens up new possibilities for diagnosis [Muenzel2016]. Methods involving full knowledge of all system variables [Roessl2007, Schlomka2008] would be capable of decomposing into arbitrary basis functions at any time, whereas Alvarez recently published a generalization of the well-known A-table approach to accomplish a three material decomposition [Alvarez2015]. By its design, also the proposed PLB forward-model (equation 6.5) is able to handle the additional attenuation by one or several k-edge discontinuities. However, measurements of the used contrast agents must be incorporated explicitly into the calibration process.

Another aspect worth considering is the available range of line-integrals that can be decomposed with sufficient quantitative accuracy. From figure 6.3 we can see that the presented estimator is able to extrapolate the number of photon counts with high accuracy even if the sample line-integrals exceed the calibration range by approximately 10%. Although this results is only exactly valid for the specific, yet realistic case investigated in this work, it can be expected that a potential use of this method in a clinical setting will not be limited by the extrapolation properties of the estimator since the maximum range of line-integrals will be determined by the scanner's field-of-view.

7 Practical implementation of photon-counting based material decomposition

In the previous chapters 5 and 6 we have outlined the development of new concepts for PCD-based spectral x-ray imaging and examined some of their potential implications using simulation studies. This chapter will now focus on the practical implementation of these methods into a newly designed imaging set-up and investigate the performance for various experimental scenarios. An overview of the set-up will be shortly presented at the beginning, followed by a series of selected representative results.

7.1 The spectral CT set-up

To enable experimental characterization of the proposed methods, a dedicated spectral micro-CT set-up based on a PCD was assembled in the course of this work. The design of the set-up was aimed at providing a flexible imaging solution both for high-resolution CT of small objects as well as for general-purpose x-ray imaging of larger samples. Considering the main components, the set-up consists of a cone-beam micro-focus x-ray tube, a state-of-the-art PCD system suitable for high-energy measurements and several positioning devices mounted on an optical table. Figure 7.1 shows an overview photograph of the assembled devices.

X-ray source

The statically mounted x-ray tube (XWT-160-CT, X-Ray WorX GmbH, Garbsen, Germany) is a micro-focus tube with a tungsten reflection target and a 2 mm thick beryllium beam exit window. The tube can be operated with a peak acceleration voltage of up to 160 kVp and has a maximum continuous target

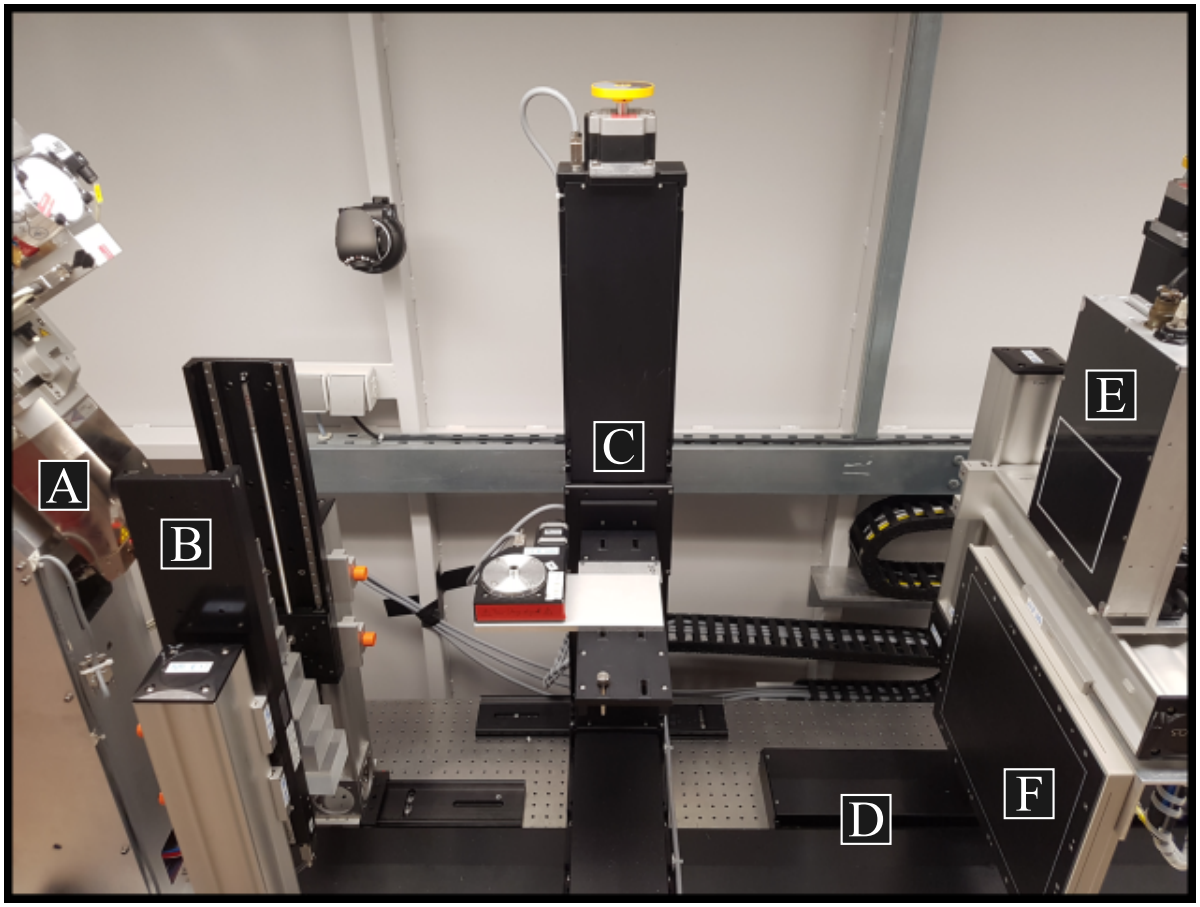

Figure 7.1: **Photograph of the assembled spectral micro-CT set-up.** This photograph shows all key components comprising a micro-focus x-ray source (A), phantoms to automatically calibrate the PLB parameters (B), mounting and positioning devices for the sample (C), automatic adjustment of magnification and voxel-size (D) and the PCD (E). Additionally, a standard flat-panel type EID is also available (F).

power output of 300 W. The peak target current is limited to 3 mA, giving a constraint for the achievable power at a given voltage. Further the size of the optical focal spot is dynamically adjusted depending on the electrical power delivered to the target. The minimum elliptical[1] spot size of $2.0 \times 3.0\,\mu m^2$ rises with increasing target power to its maximum of approximately $150 \times 300\,\mu m^2$ at a power of 300 W. The emitted cone-beam has an opening angle of approximately 30°. A collimator mounted directly in front of the exit window allows to adjust the beam shape to the current geometry and thus helps to avoid scattered radiation registered by the detector. Additional pre-filtration of the x-ray beam is enabled by inserting different filters in a slot between exit window and collimator. Frequently used filters comprise

[1] Due to the inclination of the target, the optical focal spot has the size of an ellipse, resulting in different spot sizes in the horizontal and vertical direction.

Cu or Al foils of various thickness between $100\,\mu m$ and $5\,mm$.

The PCD system

The used PCD system (XC-FLITE X1, XCounter AB, Danderyd, Sweden) features a $0.75\,mm$ CdTe sensor. The detector's active area consists of 1536×128 pixels with a native pixel size of $100\,\mu m$, arranged in a horizontal matrix of 12 readout ASICs with gaps of approx. one pixel between the modules. Thus, the complete FOV amounts to $15.4 \times 1.3\,cm^2$. The system is equipped with two separate energy thresholds offering 12 bit counting depth per pixel and provides on-chip real-time correction of charge-sharing. As mentioned in section 3.3, the used CdTe sensor is prone to polarization effects which are effectively mitigated using a fast periodic reset sequence of the sensor bias. Typical operating conditions of this detector in the course of this work were a frame-rate of $10\,fps$ and a bias reset after each frame. After energy calibration of the thresholds, the FWHM of the remaining threshold dispersion across pixels is between 4 – $5\,keV$.
Due to these features, the energy response of the *FLITE X1* PCD can be well characterized by the model introduced in section 5.1 regarding only photo-peak noise and fluorescence-escape peaks generated by the CdTe sensor. The settings for the energy threshold could therefore be optimized using the developed `PcDetector` framework as discussed exemplary in section 5.2. Since the obtained settings vary with the imaging task, the resulting threshold settings will be given in the sections discussing the individual experiments along with the underlying parameters for the incident spectrum and exposure.
In addition, the set-up offers the use of a standard flat-panel EID with a large FOV of $40 \times 30\,cm$ at a physical pixel size of $194\,\mu m$ (PaxScan 4030CB, Varex Imaging, Salt Lake City, USA). This detector can be used to obtain reference images using standard CT protocols and is employed in micro-CT studies of large objects.

Set-up geometry

The set-up is equipped with a sample positioning system allowing movement in the x-, y- and z-directions. Different mounting options are provided to accommodate various sample sizes ranging from a few millimeters up to $30\,cm$ and $25\,kg$. CT acquisitions are realized via rotation of the sample. Further, the detector system can be moved along the z-, and y-direction. Thus the set-up allows an entire and accurate geometric alignment of the imaging system, including arbitrary selection of the geometric magnification as well as the correct alignment of the sample and the detector to the center of the cone beam. The geometric magnification M resulting from a specific combination of source-to-object

distance (SOD) and source-to-image distance (SID) is given by

$$M = 1 + \frac{SID}{SOD} \tag{7.1}$$

At the used set-up, the constraints for the distances are $45\,\text{mm} \leq \text{SOD} \leq 1510\,\text{mm}$ when the collimator is in place and $810\,\text{mm} \leq \text{SID} \leq 2310\,\text{mm}$. Therefore, the theoretical lower limit for the CT voxel-size is $1.95\,\mu\text{m}$.

7.2 Calibration of the PLB forward-model and accuracy in real PCD applications

The basic procedure for calibration of the surrogate energies and intensities in the PLB model has been outlined previously in section 6.2. This section will now focus on its practical implementation and study the quantitative accuracy of the forward-model in real experimental settings. In the current set-up configuration we employ two staircase-shaped calibration phantoms of different materials with accurately known thicknesses to enable spectral decomposition into a two-material basis. The calibration phantoms are positioned between the x-ray tube and the sample holder using two additional linear-stages and can be moved separately enabling to cover the complete grid of calibration points (cf. figure 7.1 B). A convenient choice of materials is poly-vinyl chloride (PVC) and poly-methyl methacrylate (PMMA) which are then often converted into the contributions of photoelectric effect and Compton scattering basis.

Figure 7.2 shows a schematic representation of the calibration process. Due to the placement of the calibration phantoms in a cone-beam geometry, effects of the cone angle α across the detector lines need to be taken into account. In general, this leads to different calibration line-integrals on a pixel-by-pixel basis, since the path length of the x-ray beam through the object varies with the cone angle seen be each detector row. From the magnified view in figure 7.2 we obtain that this path length $|\vec{x}|$ is linked to the nominal thickness $|\vec{d}|$ of the calibration step via

$$|\vec{x}| = \frac{|\vec{d}|}{\cos(\alpha/2)} = \frac{|\vec{d}|}{\cos\left(\arctan\left(\frac{D/2}{SID}\right)\right)}, \tag{7.2}$$

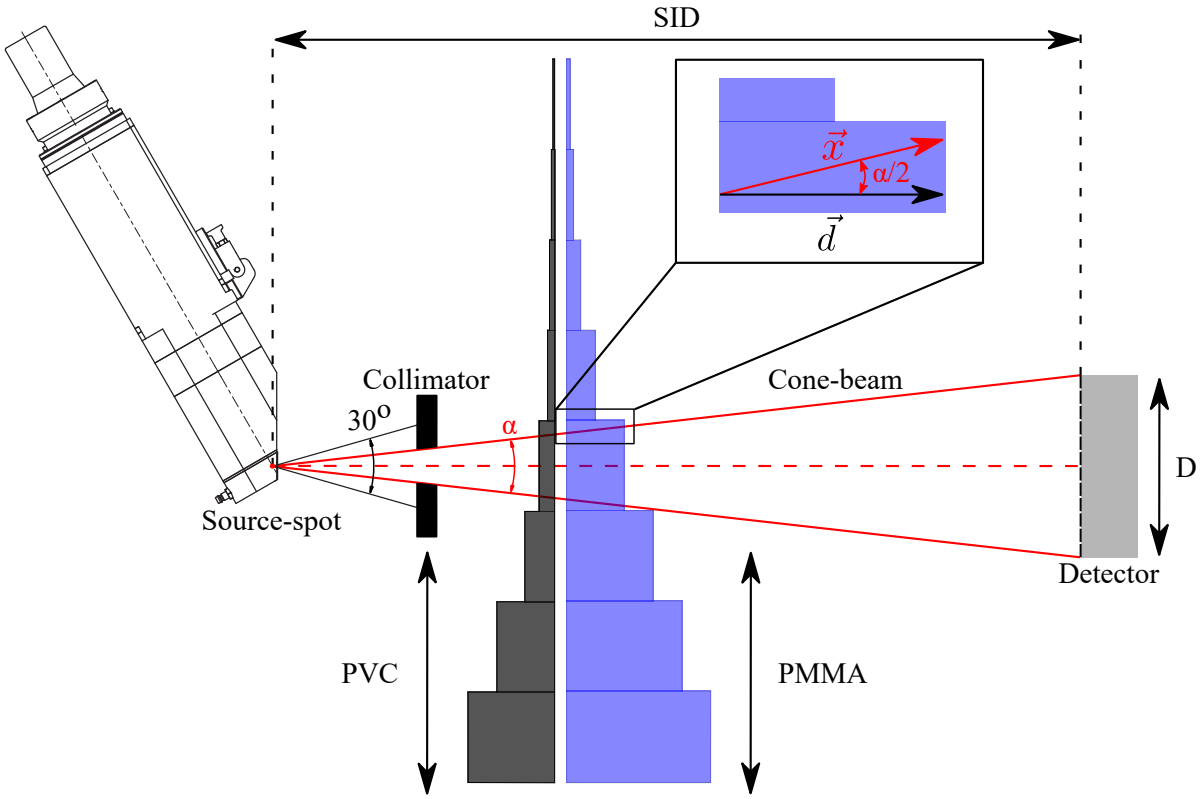

Figure 7.2: **Overview of the PLB model calibration process in the experimental set-up.** The schematic drawing summarizes the calibration process using PVC and PMMA staircase blocks and visualizes the geometric considerations required when determining pixel-by-pixel corrections for the cone-beam effects. The SID and other distances are not up to scale in this sketch.

where D is the height of the detector measured in the same units as the SID. An analog calculation is valid for the perpendicular direction, i. e. the detector columns along the fan angle β.

The currently available calibration phantoms offer up to eight steps per material. The maximum range for the calibration of the line-integrals is $80\,\text{mm}$ for PMMA and $48\,\text{mm}$ for PVC. Due to the benefits when working with a photoelectric effect and Compton scattering attenuation basis (cf. section 6.2), this grid of calibration points is typically converted into the associated line-integrals A_C and A_ph according to equation 6.6 which is visualized by figure 7.3. Since the attenuation of x-rays follows an exponential curve when the magnitude of line-integrals increases, the gradient of the expected number of photon counts is large for small line-integral values and decreases towards larger thickness. Therefore, the density of calibration points is higher at low line-integral values to make the parameter estimation process more robust in regions with large gradients. Furthermore, the number of frames acquired at

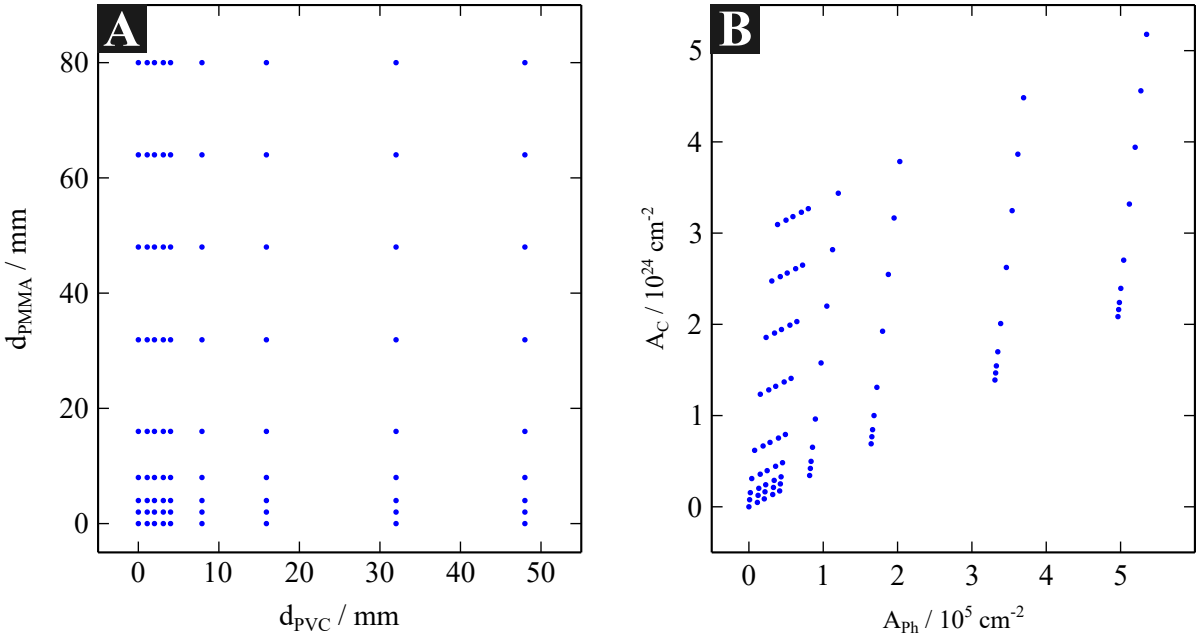

Figure 7.3: **Calibration range and distribution of points in the experimental set-up.** The current phantoms allow calibrations using up to eight steps for each material where the maximum thicknesses are 80 mm PMMA and 48 mm PVC (A). The corresponding conversion into coefficients of a photoelectric effect / Compton scattering basis are shown in plot B.

each combination of calibration steps is adjusted to keep the recorded photon statistic at a constant level for all calibration points. Therefore, a constant mean number N of photons is registered during the calibration measurement process for each energy bin and line-integral. Prior to the fitting of the parameters, the images for each calibration step were normalized using their respective frame numbers. In this way the effects of Poisson noise on the resulting PLB parameters were minimized, especially at larger line-integral values.

The experimental settings of the tube source and the detector for this study are summarized in table 7.1.

Peak voltage	Filtration	N	$\mathrm{THL_L}$	$\mathrm{THL_H}$	Frame rate
120 kVp	0.2 mm Cu	5×10^4	27 keV	52 keV	10 fps

Table 7.1: **Acquisition settings for the investigation of the forward-model accuracy.** The number N refers to the total number of photon counts seen be the low PCD threshold.

In order to allow the experimental set-up to reach a steady state of operation, the source and detector were given approximately one hour of settling time before the calibration process was started. In this way, temperature-induced drifts of the x-ray source emission or the detector thresholds were minimized.

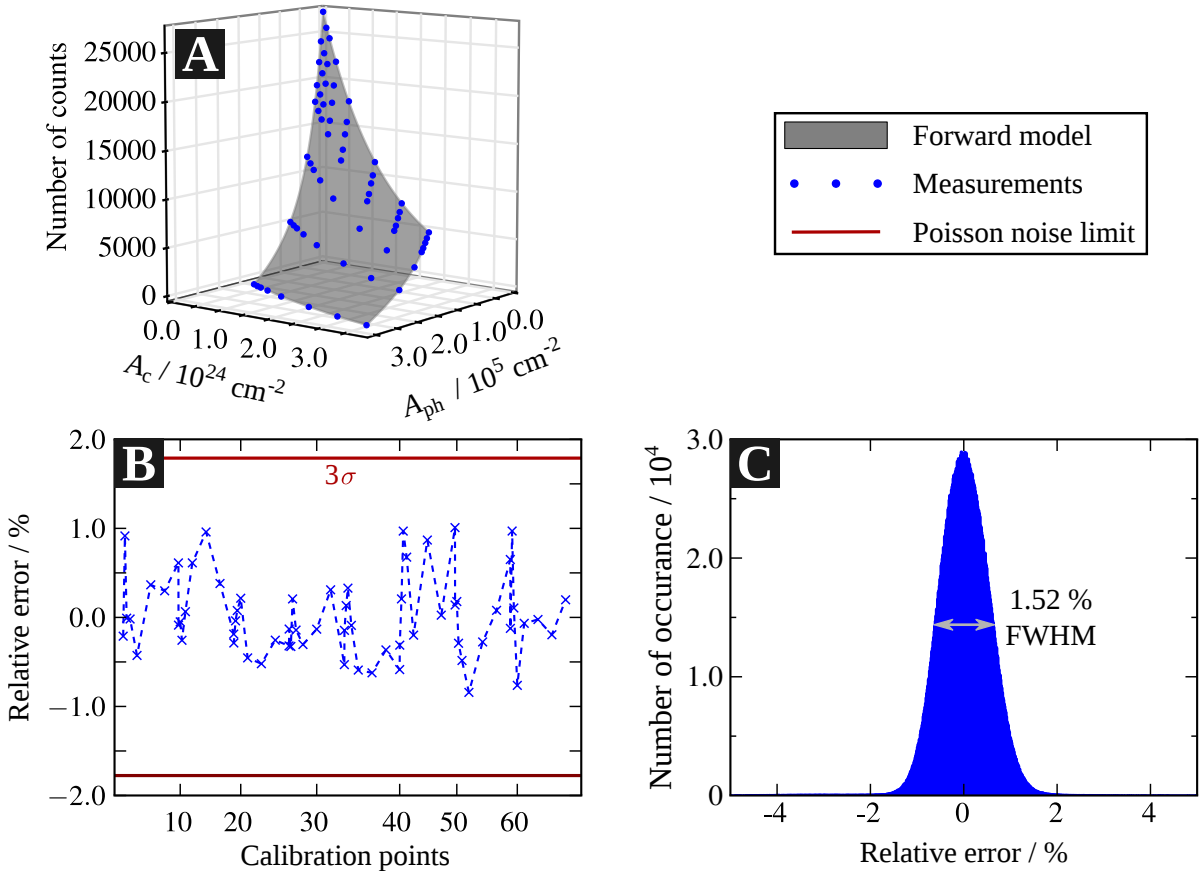

Figure 7.4: **Accuracy of the PLB forward-model in an experimental set-up.** The surface plot in (A) shows the global performance of the forward-model after fitting to the calibration data corresponding to the grid in figure 7.3. The relative bias of the predicted counts barely exceeds $1.5\,\%$ (B). An examination of the bias histogram for all pixels and calibration points (C) yields that nearly all values lie within a 3σ interval as determined by the Poisson statistic of the calibration measurement. The values in this figure are for the low PCD energy bin and the mean number of photons was $N_\mathrm{L} = 2.8 \times 10^4$ and $\sigma = \sqrt{N_\mathrm{L}}$.

A quantitative examination of the forward-model accuracy in the low energy bin is shown in figure 7.4. For an arbitrary detector pixel, the number of photon counts determined by the forward-model corresponds well to the experimental data. In part A of the figure, this is represented by a 2D surface dependent on the basis material line-integrals. Panel B shows the relative bias of the predicted counts for the same pixel over all 64 points in the calibration grid. Since all calibration points were effectively acquired under the same photon statistic, a global relative noise level can be attributed to all points. For the present study, the number of photons in the low energy bin was $N_\mathrm{L} = 2.8 \times 10^4$. Using $\sigma = \sqrt{N_\mathrm{L}}$ the relative amount of noise contained within a 3σ interval of the Poisson distribution was $1.8\,\%$. The experimentally observed bias values lie all within this interval. A statistic evaluation for all detector

pixels and all calibration points yields the bias histogram in figure 7.4 C. The behavior of the bias is characterized by a Gaussian distribution with mean value of zero and a FWHM corresponding to the uncertainty of count numbers ($\mathrm{FWHM} \approx 2.36\sigma$).
From this it becomes evident that the accuracy of the forward-model over the complete detector and range of line-integrals is governed by the photon statistics and can hence be treated as unbiased. The performance is seemingly not affected by effects present in real PCD system. The following sections will therefore focus on investigations of the quantitative accuracy and quality of material-decomposed images.

7.3 Quantitative material characterization in a phantom study

The quantitative accuracy of a MLE-based material decomposition using the PLB forward-model was evaluated using a CT scan of a cylindrical phantom. The phantom consists of a PMMA tube with $5\,\mathrm{cm}$ diameter and five cylindrical inserts with a diameter of $1\,\mathrm{cm}$ each. Four different polymers (PMMA, PVC, POM, PTFE) and aluminum have been used as insert materials. The space between the tube wall and the inserts has been filled with de-ionized water. In studies related to x-ray material characterization [Sarapata2014, Abbema2015], the electron density ρ_{el} is often used as a measure for quantitative accuracy. In a clinical context, precise knowledge of electron densities in different tissues is often required for planning of radiation therapy. In the case of spectral x-ray imaging, ρ_{el} of the phantom's materials can be determined directly from the basis material images according to equation 2.16 and serves as a quantitative measure for the decomposition accuracy. Reference values for ρ_{el} have been calculated from the chemical composition of the materials and tabulated mass densities.

For the acquisitions, the set-up geometry was set to yield a total FOV of $7.5\,\mathrm{cm}$ with an image voxel size of $100\,\mu\mathrm{m}$. The exposure parameters are listed in table 7.2:

Peak voltage	Filtration	mAs	$\mathrm{THL_L}$	$\mathrm{THL_H}$	Frame rate
110 kVp	0.1 mm Cu	4600	27 keV	52 keV	10 fps

Table 7.2: **Acquisition parameters for the quantitative measurements of electron densities in the material phantom.**

The calibration of the PLB parameters was performed as explained in the previous section 7.2. To minimize the impact of statistical noise, a very high total exposure level of $4600\,\mathrm{mA\,s}$ per was used during the CT scan, fractioned equally between 1400 angular views.

Figure 7.5 shows axial slices through the reconstructed volumes, comparing the polychromatic image

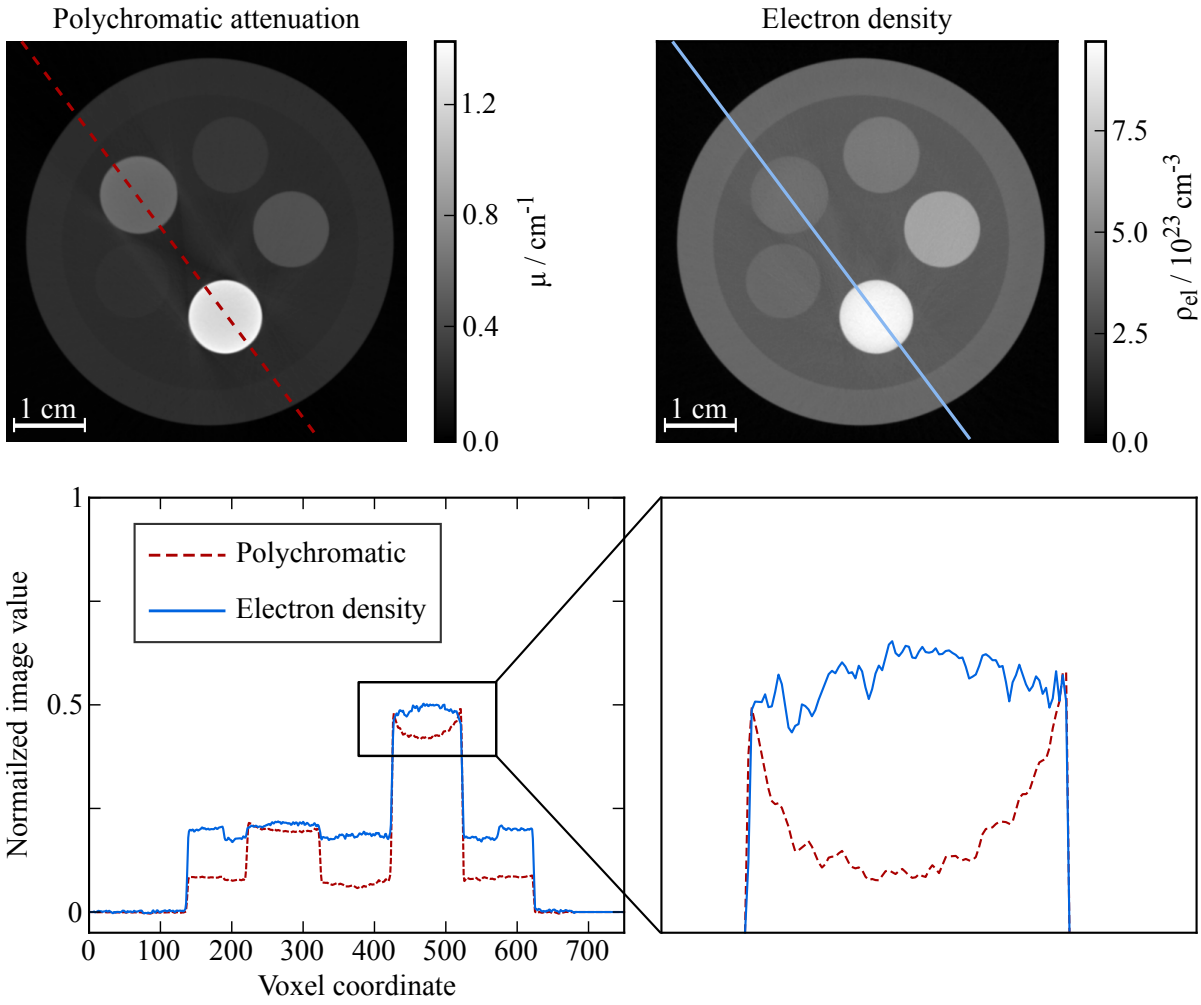

Figure 7.5: **Experimental phantom study to investigate the quantitative accuracy of electron densities.** The electron density image has been obtained directly from the decomposed Compton basis image. As shown by the plots of voxel values along the marked oblique lines, the projection-based material decomposition strongly reduces beam-hardening artifacts, therefore increasing quantitative accuracy. An overview over the measured electron densities for materials contained in the phantom is presented in table 7.3.

reconstructed from all photon counts registered above the low energy threshold to the electron density image.

A first investigation of the performance can be made by plotting lines through the PVC and Al insert in both images. Since the numeric values of both images differ by many orders of magnitude, the voxel values have been normalized to the maximum values in each volume. One can easily see that beam-hardening induced cupping artifacts in the inserts are strongly reduced by the spectral reconstruction.

Furthermore, typical streaks seen between strongly attenuating objects in polychromatic reconstructions are suppressed after the projection-based material decomposition. Therefore, the spectrally generated electron density image shows increases quantitative accuracy compared to the polychromatic estimation of the materials' linear attenuation coefficient. A closer examination of the curve for the electron density image reveals a slight inverse cupping. This feature arises from the anti-correlated behavior of noise and bias in basis material images and can not be attributed to beam-hardening effects. This observation may hint towards a slight shift of registered photon count numbers between calibration and actual measurement of the phantom. Such drifts can be attributed to two major phenomena: First, changes in the detector response function yield a time-dependent change of energy threshold values which are mostly associated with rising ambient temperature. Secondly, scattered radiation is emitted from the phantom and registered as background radiation by the detector. Since scattered radiation is not considered by the forward-model, it leads to a slight bias in the material decomposition. This explanation is contingent with the fact that photons which are Compton-scattered under a small angle with respect to their original path typically lose energy during the scattering process. Therefore, the ratio of photons registered in the low and high energy bins slightly shifts towards the low end of the spectrum. This effect is then accompanied by an under-estimation of the photoelectric absorption with a simultaneous over-estimation of the Compton component.

The obtained electron densities have been measured in circular ROIs located centrally in each polymer insert. The obtained values are compared to tabulated reference data in table 7.3 and the relative deviation of the measurements from the theoretical values is calculated. The mean bias of all investigated material samples was $1.04\,\%$.

Material	$\frac{\rho_{\mathrm{el}}}{10^{23}\ \mathrm{cm}^{-3}}$	$\frac{\rho_{\mathrm{el,measuresd}}}{10^{23}\ \mathrm{cm}^{-3}}$	$\frac{\text{Rel.error}}{\%}$
PMMA	3.87	3.92	1.3
PVC	4.21	4.16	1.2
POM	4.58	4.55	0.7
PTFE	6.26	6.22	0.6
H_2O	3.34	3.38	1.2

Table 7.3: **Quantitative accuracy of the measured electron densities in the material phantom.**

Therefore, the resulting bias is typically small, ranging in the order of $1\,\%$. This result corresponds well to the magnitude of bias present in the PLB forward-model, c f. section 7.2. Comparing the bias in table 7.3 obtained with our approach to values reported in other recent studies, the accuracy of PLB-based material decomposition fits in between results obtained with polychromatic x-ray phase-contrast measurements [Sarapata2014] (mean bias of $3.1\,\%$ for the same materials) and a recent method for dual-energy imaging based an accurate parameterization of all involved photon interactions [Abbema2015]

(mean bias of approximately $0.5\,\%$ for tissue-equivalent compounds). Especially in the latter study the bias improved due to correctly accounting for all involved interactions including coherent scattering. All in all the presented phantom measurements demonstrate that MLE-based material decomposition using the PLB forward-model yield accurate material parameters under realistic experimental conditions. Applications of this technique to produce various spectral images of different objects will subsequently be presented in the following sections.

7.4 Performance of PLB-based spectral imaging in a clinical context

Applications in clinical radiology or pre-clinical research are one of the most promising developments in this area and have driven many developments ranging from PCD technology to spectral data processing methods. Examples for clinical applications have been outlined at various stages in this thesis already. Here we will discuss two possible applications using measurements of biological samples that may have clinical relevance.

7.4.1 Soft-tissue and bone separation in clinical samples

Separation of the spectral attenuation data into contributions arising from soft-tissue and bone material can be of great diagnostic value in clinical radiology. Applications for this particular spectral basis cover the quantification of bone mineral content to diagnose osteopenia / osteoporosis, visualization of subtle bone lesions like bone edema and others [McCollough2015]. Soft-tissue images can for example help to identify lesions of collagen-rich tissue like tendons and ligaments [Mallinson2014]. In our case we used the photoelectric effect / Compton scattering basis and converted it to bone and tissue-equivalent images using their material properties as defined in the ICRU reports and XCOM database:

Material	ρ_{el}	Z_{eff}
Soft tissue	3.51×10^{23}	7.64
Cortical bone	5.95×10^{23}	13.84

Table 7.4: **Electron densities and effective atomic numbers of soft tissue and cortical bone.**

The line-integrals of soft tissue and bone $\begin{pmatrix} A_{\mathrm{s}} \\ A_{\mathrm{b}} \end{pmatrix}$ are calculated using the equation

$$\begin{pmatrix} A_\mathrm{s} \\ A_\mathrm{b} \end{pmatrix} = M^{-1} \begin{pmatrix} A_\mathrm{ph} \\ A_\mathrm{c} \end{pmatrix}, \qquad M = \begin{pmatrix} \rho_{\mathrm{el,\,s}} Z_{\mathrm{eff,\,s}}^{3.8} & \rho_{\mathrm{el,\,b}} Z_{\mathrm{eff,\,b}}^{3.8} \\ \rho_{\mathrm{el,\,s}} & \rho_{\mathrm{el,\,b}} \end{pmatrix}, \tag{7.3}$$

where M is the matrix to calculate the photoelectric / Compton coefficients for an object composed of soft tissue and bone with material parameters given in table 7.4. Consequently, the bone and soft tissue images depict the projected thickness and density of both materials.

Using our experimental set-up, a preserved specimen of a human hand was scanned. In order to cover the full height of the object with the available 128-slice PCD, a technique called time-delayed summation (TDS) [Nowak2012] was adopted. Thereby the detector continuously acquires frames while the objects is shifted a certain distance perpendicular to the rows from frame to frame. The final image is reconstructed by inserting each acquired frame into the position corresponding to the shift distance and summing up all relevant contributions.

The images in figure 7.6 show the results obtained with the PCD-based soft-tissue and bone separation. For comparison, a clinical radiograph was also acquired at the *Klinikum Rechts der Isar* following a routine imaging protocol with $55\,\mathrm{kVp}$ / $4\,\mathrm{mA\,s}$. The acquisition settings for the spectral images have been adapted to the PCD requirements (table 7.5).

Peak voltage	Filtration	mAs	$\mathrm{THL_L}$	$\mathrm{THL_H}$	Frame rate
110 kVp	0.1 mm Cu	3.5	23 keV	55 keV	10 fps

Table 7.5: **Acquisition parameters for the bone / soft tissue decomposition of a human hand.**

The standard clinical image exhibits the typical structural overlap of bones and soft tissue anatomy. These issues are almost completely eliminated in the spectral images, where a clean separation between bone and soft tissue anatomy is achieved. Therefore, the bone image shows increased contrast and a better delineation of e. g. joint spaces. In the soft-tissue images, bone structures are still visible as darker areas. This behavior is to be expected since the presence of bone in the beam path results in voids in the soft-tissue thickness.

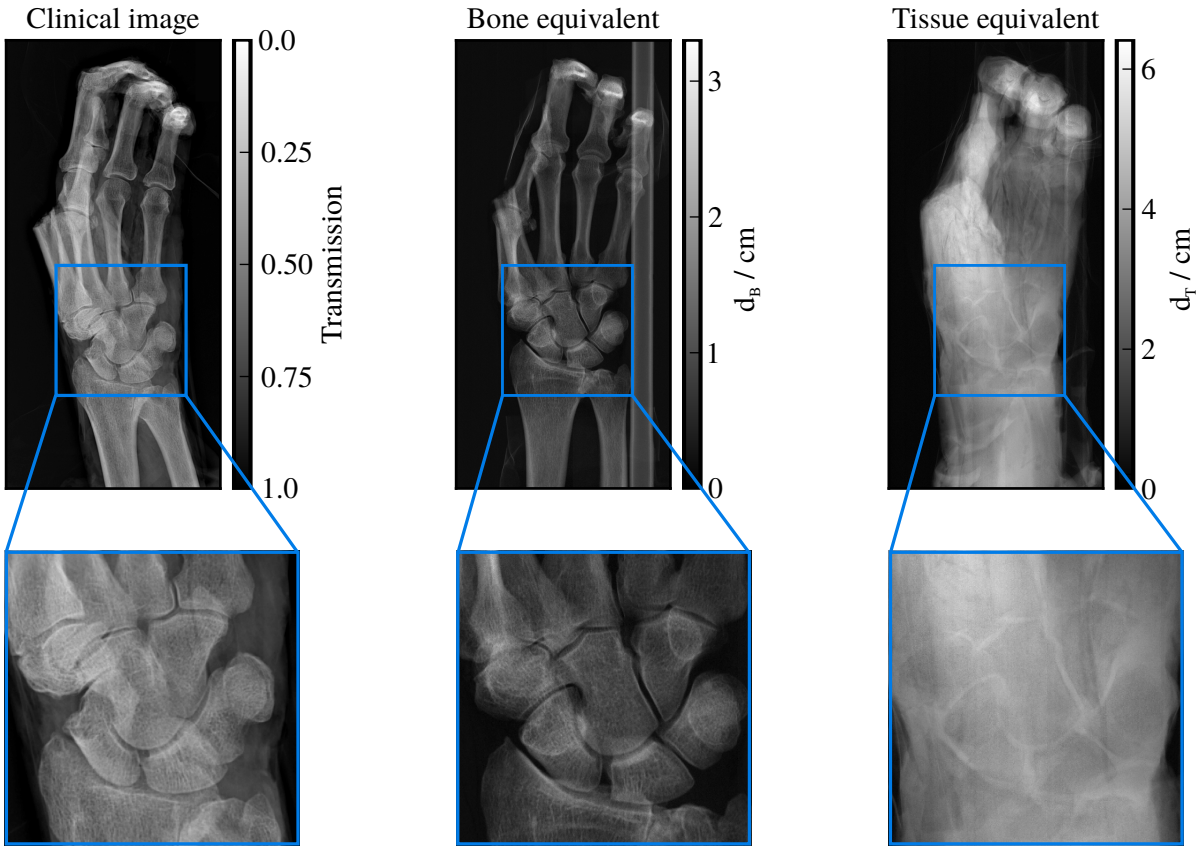

Figure 7.6: **Separation of a clinical radiograph into bone and soft-tissue equivalent images.** The clinical image was obtained using a clinical radiography system equipped with an EID following a routine protocol for distal extremities (55 kVp / 4 mA s). The bone and tissue-equivalent images have been calculated from a photoelectric effect / Compton effect attenuation basis as outlined in equation 7.3. Compared to the clinical reference image, the bone image shows increased contrast due to non-overlapping of structures. Note that the projection angle is slightly different for clinical and PCD images.

7.4.2 Effective separation of protein, lipid and water content in pre-clinical research applications

For some pre-clinical or clinical applications, a more detailed examination of the tissue composition might be of value. In this context, further classification and quantification of general soft tissue into protein, lipid, and water-equivalent content can help to determine the progression and prognosis in various diseases ranging from tumors [Tromberg2005] to liver pathologies [Schreuder2008]. Recently, a method for decomposition into protein, lipid and water utilizing x-ray phase contrast measurements was developed at the chair of biomedical physics of the TUM [Willner2016]. In this approach, attenuation

and phase Hounsfield units are employed to span the vector space in which the decomposition is accomplished. However, this method typically requires the use of low energies since the required separation of basic x-ray interaction mechanism is not guaranteed at energies of some 10 keV and more. While the phase-contrast image is always attributed to coherent scattering processes within the object and therefore reflects the electron density, the absorption image is principally a superposition of several interaction mechanisms including photoelectric absorption and scattering processes (cf. equation 2.20). Therefore, attenuation and phase images are no longer complementary at higher x-ray energies [Sarapata2015].

By utilizing PCD-based spectral x-ray imaging we sought to generalize the idea of a vector decomposition into the three tissue constituents and make it applicable to higher energies as used in clinical imaging modalities. Using the spectral basis of photoelectric attenuation and Compton scattering, one obtains two linear independent images that are independent of photon energy. In this 2D vector space, any material is identified by its vector $\begin{pmatrix} a_{\mathrm{ph}} \\ a_{\mathrm{c}} \end{pmatrix}$. The assumption that this material is exclusively composed of protein, lipid and water with mass fractions p, l and w is expressed by the constraint

$$w + p + l \stackrel{!}{=} 1. \tag{7.4}$$

The photoelectric and Compton coefficients of the pure materials water, protein and lipid can be calculated directly from the tabulated elemental composition of those materials [Woodard1986].

Similar to equation 7.3 we can use a matrix notation of the above relations to decompose the spectral basis images into protein, lipid and water volume fractions.

$$\begin{pmatrix} a_{\mathrm{ph}} \\ a_{\mathrm{c}} \\ 1 \end{pmatrix} = \underbrace{\begin{pmatrix} a_{\mathrm{ph,\,W}} & a_{\mathrm{ph,\,P}} & a_{\mathrm{ph,\,L}} \\ a_{\mathrm{c,\,W}} & a_{\mathrm{c,\,P}} & a_{\mathrm{c,\,L}} \\ 1 & 1 & 1 \end{pmatrix}}_{\boldsymbol{M}} \begin{pmatrix} w \\ p \\ l \end{pmatrix}, \tag{7.5}$$

$$\begin{pmatrix} w \\ p \\ l \end{pmatrix} = \boldsymbol{M}^{-1} \begin{pmatrix} a_{\mathrm{ph}} \\ a_{\mathrm{c}} \\ 1 \end{pmatrix}. \tag{7.6}$$

This approach was applied to spectral images of a formalin-fixated mouse. To demonstrate the ability to use higher energies, acquisition settings similar to clinical techniques were used despite the small object size:

Peak voltage	Filtration	mAs	$\mathrm{THL_L}$	$\mathrm{THL_H}$	Frame rate
120 kVp	0.2 mm Cu	200	23 keV	57 keV	10 fps

Table 7.6: **Acquisition parameters for the decomposition into protein, lipid and water fractions.**

In figure 7.7 the results of the decomposition is summarized. The first row shows the standard spectral basis images along with the polychromatic reconstruction. The second row shows the result of the vector decomposition into the three tissue components. To suppress excessive noise amplification, the spectral basis images have been post-processed using a de-noising algorithm that exploits properties of the spectral images, especially the anti-correlation of noise. The algorithm developed at the chair uses trained dictionaries and a low-noise guide image for structure determination [Mechlem2016]. Especially the lipid and water images depict complementary structures as fat-depositions in the body normally exclude water. Proteins can in turn be found in a variety of tissue types as they occur in connective tissue and the extra-cellular matrix.

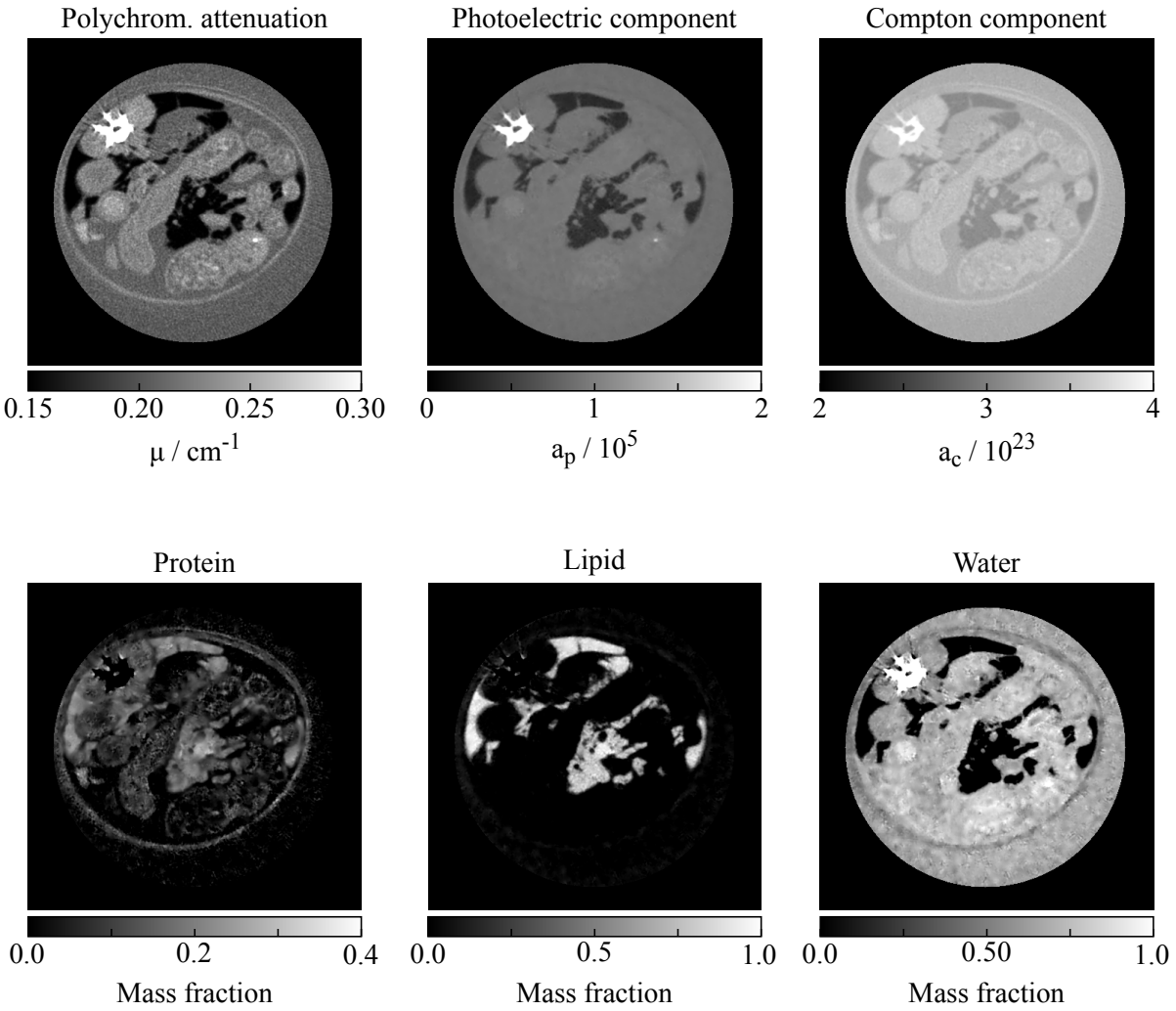

Figure 7.7: **Separation of protein, lipid and water fractions in biological tissues.** The spectral PCD data is first decomposed into a photoelectric effect / Compton scattering attenuation basis (first row). The basis material images are subsequently transformed into a protein and lipid attenuation basis. Using a conservation of volume constraint under the assumption that the sample contains water, a third basis image can be deduced for the water fraction in each voxel (second row).

7.5 Application of PCD-based spectral imaging for material-scientific applications

Until now, applications of spectral x-ray micro-CT in the field of material science and NDT have not yet attracted the same amount of interest as in clinical radiology. The available techniques are usually lim-

ited to simple 2D histogram-based analysis of dual-energy measurements or basic image-based material decomposition applications [Nachtrab2011, Guo2012, Fuchs2013, Bennett2014, Pauwels2015]. This can partly be attributed to the fact that many micro-CT systems utilize two separate scans to acquire spectral bins. Dual source concepts are difficult to realize in micro-CT due to various limitations such as geometric and economic constraints as well as physical aspects like cross-scattering of photons between the separate tube-detector pairs [Engel2008]. Additionally when using a single source to acquire the energy-selective images in separate scans, the time required to obtain the data strongly increases and data processing can be hampered by movement of the sample so that the low and high energy data are not registered to one another. This issues could be tackled by the use of a energy-discriminating PCD. However, publications in that direction are still limited [Bennett2014, He2013]. In this section, we will present some investigations on the use of projection-based MLE material decomposition utilizing spectral images obtained by a PCD. Sample applications for two major challenges in NDT and material science, namely reduction of beam-hardening artifacts and increased material contrast, will be discussed.

7.5.1 Metal artifact reduction in micro-CT of highly attenuating objects

In many cases, samples investigated for NDT and material scientific purposes include strongly attenuating objects like metals or other highly dense structures. Prominent streaks or cupping decrease the accuracy of quantitative imaging and complicate image analysis, for instance when performing feature segmentation [Prevrhal2004, Sriwayu2015, Jovanovic2013] and correction of such artifacts still widely relies on empirical methods. The simulations presented in chapter 6 show that the projection-based MLE of spectral basis materials using the PLB forward-model can handle beam-hardening effects in a wide range of line-integrals. To demonstrate this ability, a CT scan of a 9 V block battery was performed and decomposed using the acquisition settings in table 7.7.

FOV	SID	SOD	voxel size	projections per 360°
3 cm	120 cm	24 cm	40 µm	1400

Peak voltage	Filtration	mAs	$\mathrm{THL_L}$	$\mathrm{THL_H}$
140 kVp	0.2 mm Cu	1800	23 keV	55 keV

Table 7.7: **CT geometry and image parameters for the battery.** The voxel size and field-of-view are measured at the center of rotation. The tube loading was calculated for the total acquisition time of the measurement.

In figure 7.8 the images obtained after a conventional polychromatic reconstruction are compared to a

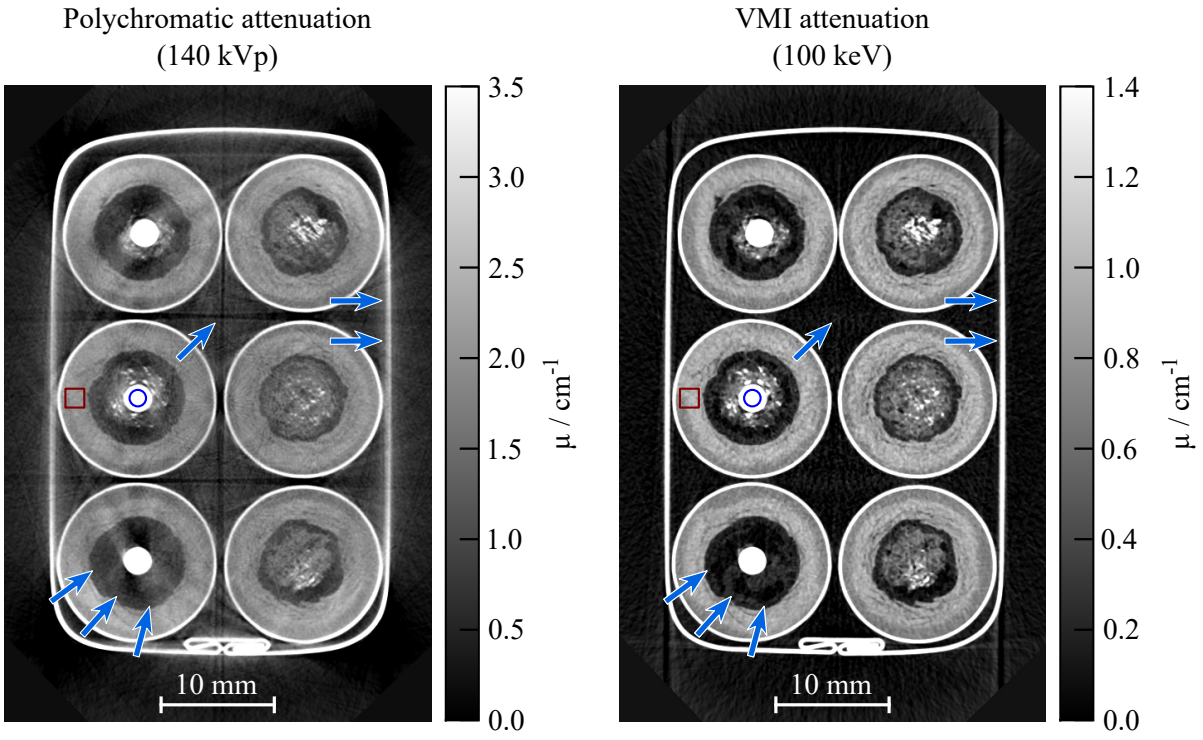

Figure 7.8: **Metal artifact reduction in NDT applications using PCDs.** Prominent beam-hardening artifacts like cupping and streaking are drastically reduced in virtual monochromatic images generated from the spectral basis images. This is particularly beneficial in NDT applications which often involve the investigation of samples containing metal parts. ROIs used to assess the CNR are marked by the circular and square indicators.

VMI at 80 keV generated from the photoelectric / Compton basis images. The VMI is calculated from the decomposition data by inserting the basis material reconstructions together with the desired energy into equation 2.15. To reduce the effects of propagation of anti-correlated basis-material noise into the VMI, the photoelectric / Compton images have been postprocessed using the inhouse-developed algorithm presented in [Mechlem2016]. Thereby, noise correlations are effectively reduced. The energy level for VMI in this example was chosen such that the observed artifacts were suppressed.

Despite the high beam energy and copper filtration, significant beam-hardening artifacts are observed in the conventional image. The arrows in the polychromatic reconstruction mark positions of beam-hardening streaks that can be attributed mostly to metal artifacts. Additionally, cupping is observed towards the center of the battery. In many cases these artifacts obstruct low-contrast details in the sample structure. Due to the suitable choice of the VMI energy level, the quantitative values of the obtained voxel attenuation is comparable to the polychromatic case. However, beam-hardening associated artifacts are strongly suppressed by utilizing the spectral data. As indicated by the arrows, various features of the

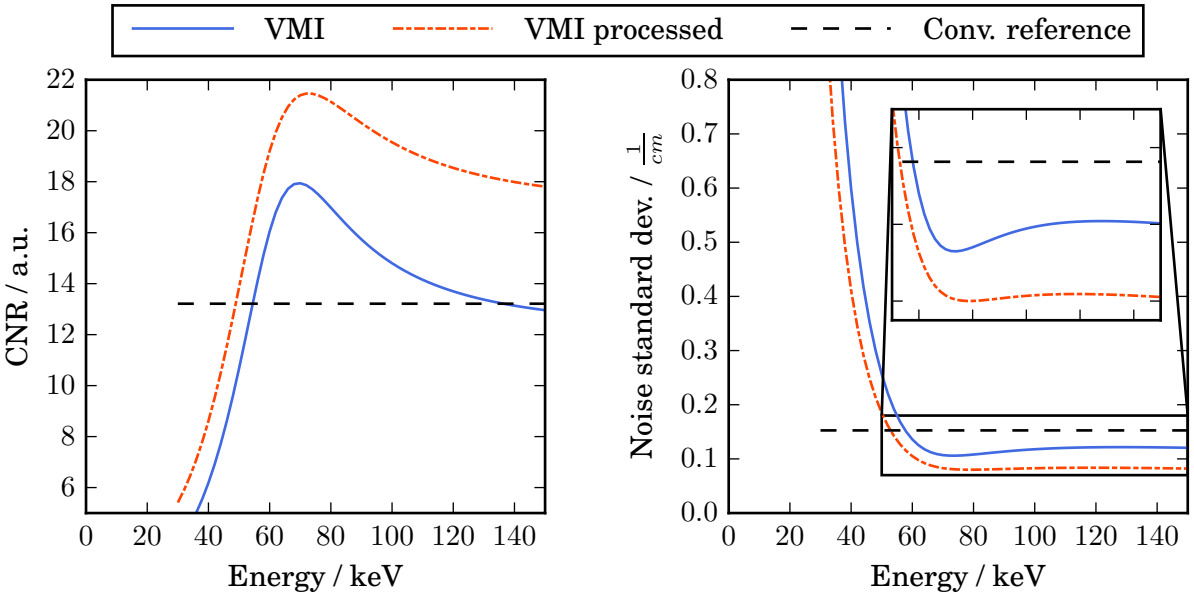

Figure 7.9: **CNR enhancement in the battery sample VMI.** Dependent on the VMI energy the CNR was evaluated for the ROIs shown in figure 7.8. Compared to the conventional image CNR was enhanced by up to 62 % in postprocessed VMI images. Especially the behavior of the noise where the dependency on the energy is very weak towards larger energies is a unique feature due to the projection-based material decomposition and reduction of anti-correlation.

object could be retrieved in the spectral reconstruction.

In addition, the CNR was evaluated between the marked ROIs. Values for the CNR have been calculated for different VMI energy levels between $30-150$ keV and for the conventional reference image. Besides the evaluation of post-processed spectral data, the CNR was also determined in VMIs created from the raw spectral basis images. The left panel in figure 7.9 shows the obtained curves dependent on the energy. Over a wide range of energies, both CNR curves exceed the reference value set by the conventional polychromatic image. In case of de-noised basis materials the CNR was enhanced by 62 % while using unprocessed VMIs still yields an improvement of 35 % compared to the reference value. However, the values from the raw VMIs show a stronger energy-dependence towards higher energies and the image quality eventually drops below the reference. Reducing the anti-correlated noise in the basis material images leads to a much flatter curve for image noise as seen in the right panel, allowing the selection of a higher energy level which reduces beam-hardening associated artifacts more effectively. These results can be compared to the results presented in section 4.4 for the CNR and noise in a commercial dual-layer CT scanner. Especially the behavior of the noise found there is a unique feature due to the projection-based material decomposition and reduction of anti-correlation. In the previous literature on virtual monochromatic imaging, noise was reported to have a strongly pronounced global minimum and

to increase for lower and higher energies [Yu2011, Pomerantz2013]. Furthermore, noise in VMIs was often found to be higher than in conventional images [Yu2011, Yamada2014]. Besides the discussed reduction of artifacts the results presented in this section, using our approach of combining PLB-based material decomposition with joint spectral de-noising exploiting anti-correlation, show strongly reduced noise compared to conventional images and a nearly constant noise level at higher energies.

Although the data presented in this section only shows a single application, the general ability of projection-based material decomposition to handle and correct beam-hardening associated artifacts in micro-CT is clearly demonstrated and encourages further refinement and application of this method.

7.5.2 Contrast enhancement and material identification in spectral micro-CT

One key task in material science and NDT is the recognition and identification of various materials contained within an object of interest. Since every material imprints its unique attenuation onto the x-ray beam, spectral imaging methods can help to accomplish material identification in micro-CT applications. For the purpose of demonstrating possible applications, a drill core from piece of concrete was examined with a relatively high resolution of 10 µm. Concrete was selected since it contains features of various materials and structure sizes that cover a wide range of spatial frequencies [Mehta1986]. Furthermore, properties of concrete and cement samples are frequently studied using x-ray micro-CT techniques.

The acquisition settings for the drill core are summarized in table 7.8.

FOV	SID	SOD	voxel size	projections per 360°
1.5 cm	100 cm	10 cm	10 µm	1700

Peak voltage	Filtration	mAs	$\mathrm{THL_L}$	$\mathrm{THL_H}$
120 kVp	n. A.	350	27 keV	52 keV

Table 7.8: **CT geometry and image parameters for the concrete drill-core.** The voxel size and field-of-view are measured at the center of rotation. The tube loading was calculated for the total acquisition time of the measurement.

The obtained spectral projection data was decomposed into the photoelectric / Compton basis line-integrals and reconstructed using FBP. Subsequently, de-noising using the dictionary-based algorithm from [Mechlem2016] was applied to the volumes. Figure 7.10 shows an axial slice of the obtained images. Besides the polychromatic attenuation, the figure depicts the basis-component images of the material decomposition.

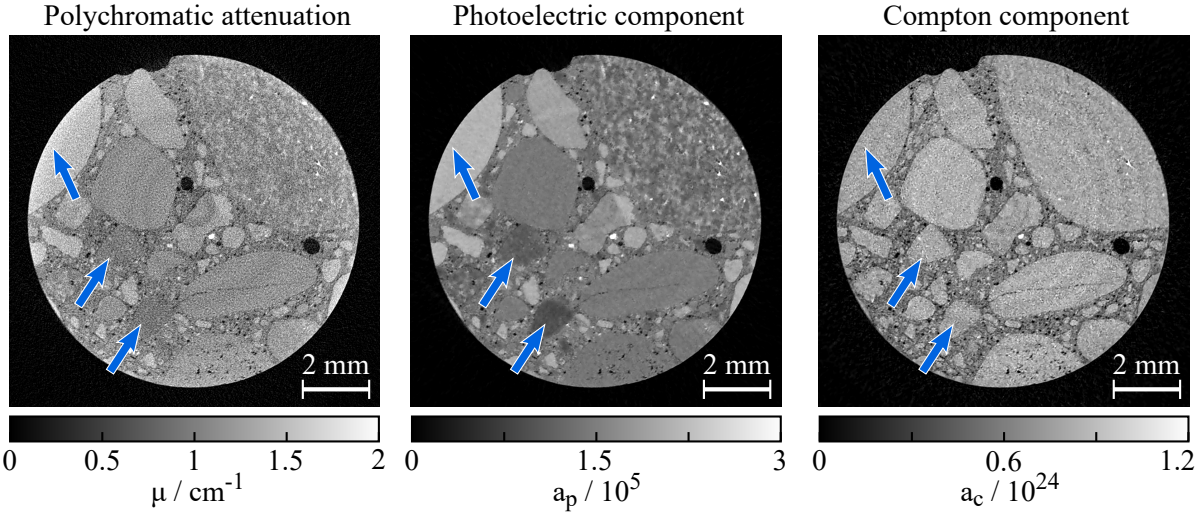

Figure 7.10: **Spectral micro-CT of a concrete drill core.** The sample with a diameter of 1 cm was reconstructed at a voxel size of 10 µm. In the photoelectric and Compton basis images, a reduction of beam-hardening induced cupping can be observed. Furthermore, an increased contrast between different constituents of the concrete is achieved via spectral decomposition.

Compared to the conventional attenuation image, the spectral basis-component images provide an enhancement of image contrast. The fine granulation of the concrete, which is barely visible for some features in the conventional polychromatic attenuation image, can be distinguished more easily in the spectral basis. The photoelectric component primarily yields enhanced contrast between materials with largely diverse atomic number while the Compton image pronounces the contrast between the aggregates and the cement. Apart from the improvement of the image contrast, the basis-component images again offer reduced beam-hardening artifacts mainly in the form of reduced cupping (cf. section 7.5.1).

A quantitative analysis of the spectral basis images also enables the identification of different materials contained in the concrete mixture. Therefore, the photoelectric effect / Compton scatter images are converted into the characteristic material properties, i. e. electron density and effective atomic numbers according to equations 2.16 and 4.5. The resulting values are visualized in a 2D histogram as shown in figure 7.11.

Thereby, the most common constituents and aggregates of concrete can be identified. Among those, quartz (SiO_2), magnesite ($Mg[CO_3]$) and dolomite ($CaMg[CO_3]_2$) could be identified, which are typical minerals found in concrete [Mehta1986]. The mineral's reference values were again calculated using tabulated data, yielding an effective atomic number of 11.75, 9.47 and 13.42, for quartz, magnesite and dolomite, respectively. The corresponding values for the electron density of the three minerals were

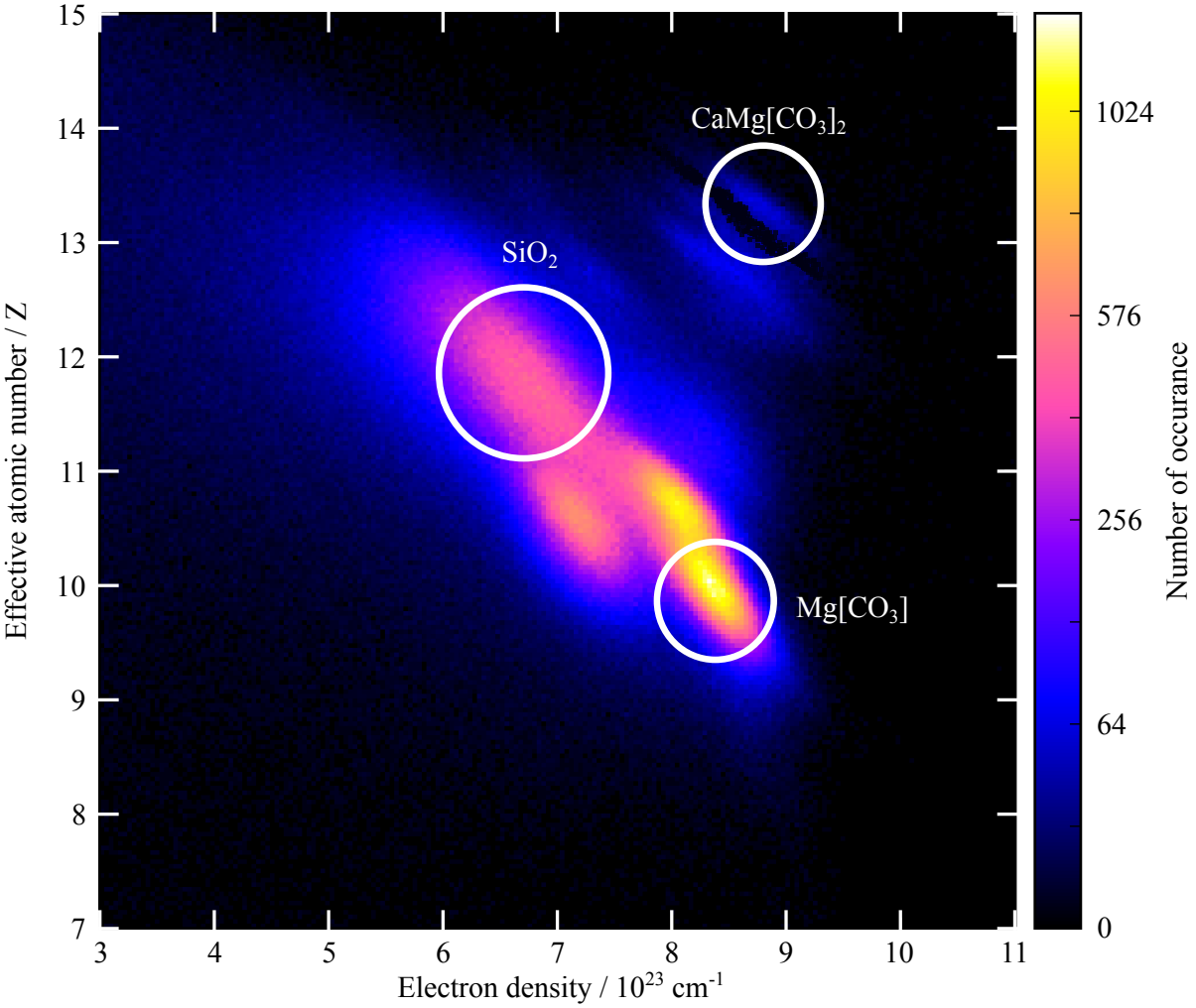

Figure 7.11: **2D histogram of material properties contained in the concrete drill core.** The electron density and effective atomic numbers have been calculated from the spectral basis images. The intensity in the image corresponds to the frequency of occurrence in all voxels of figure 7.10 in a logarithmic scale. The histogram allows the identification of the most common constituents of concrete.

$6.89 \times 10^{23}\,\mathrm{cm}^{-3}$, $8.87 \times 10^{23}\,\mathrm{cm}^{-3}$ and $8.64 \times 10^{23}\,\mathrm{cm}^{-3}$.
Calcite ($Z_{\mathrm{eff}} = 15.72$, $\rho_{\mathrm{e}} = 8.42 \times 10^{23}\,\mathrm{cm}^{-3}$) which is a further typical component of the aggregates in ordinary concrete could not be observed in this sample. The remaining histogram peaks probably arise from very fine granulation, which could not be resolved directly given the spatial resolution of the measurement. Therefore, partial volume effects are observed in many image voxels and the respective peaks in the 2D histogram emerge from mixtures of many different chemical elements. These can not be assigned to any particular mineral in the concrete.

8 Beyond spectral imaging: X-ray deconvolution microscopy using photon-counting detectors

Besides spectral sensitivity, PCDs offer other improvements compared to conventional EIDs, c.f. chapter 3. Among those, increased sharpness of the PSF and improved SNR close to the Poisson limit at very low count rates can be exploited to enhance x-ray imaging applications especially when very high spatial resolution is required.

Until now, x-ray microscopy methods are becoming increasingly important in various fields of applied research. Both life sciences and material sciences benefit from spatial resolution in the order of a few micrometers down to the nanometer range. Ultrahigh-resolution imaging at nanometer scale typically utilizes monochromatic synchrotron radiation and additional x-ray optical elements [Horowitz1972, Schmahl1980, Sakdinawat2010] to focus the x-ray beam down to diameters in the nanometer range. However, in typical laboratory-based x-ray microscopy applications, intermediate resolution in the range of a few micrometers is considered most important regarding the size of typical structures within such samples. The use of hard x-rays in the range of $20 - 100\,\mathrm{keV}$ is mostly required due to the size and chemical composition of the samples.

Laboratory-based high-resolution imaging is usually achieved using two distinct methods or by a combination of both: Either an optical lens is coupled to a CCD with very small pixel size to magnify the x-ray image projected onto a scintillator crystal [Flannery1987] or the direct magnification in a cone-beam geometry [Sasov1998] is exploited. Especially when both approaches are combined, resolution down to the sub-micrometer level can be achieved [Flannery1987]. High resolution x-ray imaging is regularly combined with CT techniques in order to obtain 3D information. Nevertheless, micro-CT suffers from the limited photon flux of the employed micro-focus x-ray sources due to the requirements of a very small focal spot size. This limitation leads to rather long exposure times, especially in tomography applications which makes rapid inspection of large numbers of samples difficult to achieve. Additionally

the geometric magnification limits the maximum sample size and the equipment for such microscopes tends to be rather cost intensive.

In this chapter, we demonstrate an approach to obtaining resolution in the range of $10\,\mu m$ making use of unique properties of a PCD system. The presented technique does neither require x-ray optical elements, nor microfocus-sources to yield high-resolution images. Instead we make use of the box-like PSF that is present in systems based on the *MEDIPIX3RX*[1] readout ASIC [Ballabriga2013]. PCDs based on this ASIC have the advantage of a small physical pixel-size of $p = 55\,\mu m$ combined with a real-time on-chip correction for charge-sharing effects, c.f. chapter 3. This particular mode of operation is called charge-summing mode (CSM) and results in an improved spectral response of the detector and yields a box-shaped PSF matching the detector pixel size.
In particular, the *LAMBDA* detector system[2] [Pennicard2013], which is based on the *MEDIPIX3RX*, was used throughout this work. The particular assembly is equipped with a $300\,\mu m$ thick Si sensor at $100\,V$ bias. The *LAMBDA* was operated an energy threshold of $8\,keV$ to cut off the electronic noise in CSM.

We will call the proposed method "XDM" [Ehn2016] in the following, where we refer to a similar approach in optical fluorescence microscopy [Sibarita2005]. The following sections will first highlight the basics of the developed method and then present a few examples of projection and micro-CT applications.

8.1 Description of the method

The fundamental principle is based on a common super-resolution technique, namely raster-scanning the sample in front of the detector with sub-pixel sized steps. In this context, super-resolution shall refer to methods for obtaining spatial resolution smaller than the physical size of a detector pixel (sub-pixel resolution). A schematic overview of our approach is illustrated in figure 8.1(A). The total scanning range equals exactly one pixel-pitch of the detector. Generally, translating the detector instead of the sample is equivalent. However, scanning the sample has the advantage that field inhomogeneities of the x-ray source are easily canceled out after a flat-field correction of the detector. Thereby, information about the sample structure on a sub-pixel scale can be obtained while the raster scanning actually constitutes an oversampling of the object in the spatial domain. The oversampled images are obtained after proper re-ordering of the raster-scanned images. As we have discussed in [Ehn2016], this oversampling and

[1] Developed within the Medipix3 collaboration based at CERN, Switzerland.
[2] Developed by DESY, Hamburg and Technische Universität München

re-ordering procedure can be treated as follows: $I^{\mathrm{D}}_{\mathrm{x,y}}$ denotes the intensity recorded by a PCD at the physical pixel coordinate (x, y) given in units of the pixel size p. An object $O(\xi, \upsilon)$ is to be imaged at super-resolution employing $\mathrm{M} \times \mathrm{N}$ raster steps in the x and y - direction. The resulting intensity $I^{\mathrm{SR}}_{\mathrm{Mx+m,Ny+n}}$ in the oversampled super-resolution image is constructed via

$$I^{\mathrm{SR}}_{\mathrm{Mx+m,\ Ny+n}} = I^{\mathrm{D}}_{\mathrm{x,y}} \left(\mathrm{T} \left(\frac{\mathrm{m} \cdot p}{\mathrm{M}}, \frac{\mathrm{n} \cdot p}{\mathrm{N}} \right) O(\xi, \upsilon) \right), \qquad m = 1 \ldots \mathrm{M},\ n = 1 \ldots \mathrm{N}, \tag{8.1}$$

where $\mathrm{T}(m,\ n)$ denotes the translation of the object by a given distance in the x and y - direction, figure 8.1 (B – D). However, the raster-scanning introduces a strong correlation between neighboring pixels depending both on the total number of steps and on the width of the initial detector PSF. If the PSF of an original pixel is known, one can estimate the PSF of the raster-scanned image and apply a deconvolution method, such as the Richardson - Lucy algorithm [Richardson1972, Lucy1974], to restore the latent image. In our notation, the iterative deconvolution process can be written as

$$I^{\mathrm{XDM}}_{n+1} = I^{\mathrm{XDM}}_{n} \cdot \left(\frac{I^{\mathrm{SR}}}{I^{\mathrm{XDM}}_{n} \otimes \mathrm{PSF}} \otimes \overline{\mathrm{PSF}} \right), \tag{8.2}$$

where I^{XDM}_{n} is the intensity in the XDM image after iteration n, $\overline{\mathrm{PSF}}(x,\ y) = \mathrm{PSF}(-x,\ -y)$ is the spatially flipped point-spread function and the operator $\otimes$ denotes a discrete convolution. For this studies, $n = 5$ iterations have been performed. Generally, with Richardson - Lucy deconvolution the number of iterations should be kept as small as reasonably possible in order to ensure sufficient resolution enhancement and to avoid amplification of noise.

To combine the XDM images with CT, a standard FBP algorithm with a Ram-Lak filter was used to reconstruct the 3D volume from the deconvolved images. In this case, FBP was chosen over state-of-the-art iterative reconstruction methods in order to demonstrate the raw performance of the proposed XDM method regardless of the choice of regularization parameters which may additionally affect the obtained resolution. A Ram-Lak reconstruction filter was chosen since it aims to preserve high-frequency image content.

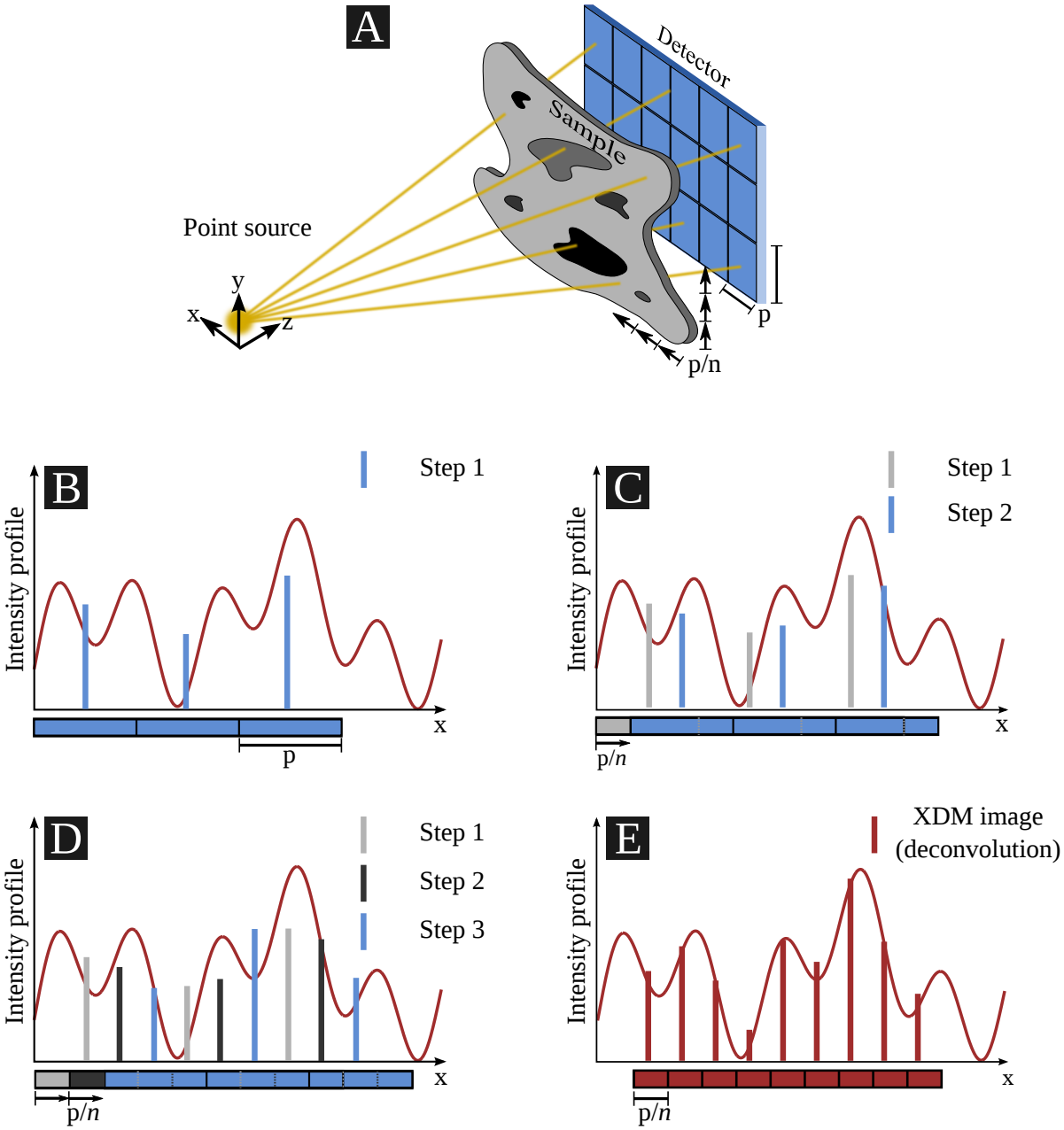

Figure 8.1: **Illustration of the XDM method.** (a) The sample is raster-scanned in front of the detector with n sub-pixel sized steps. (b) - (d) During the stepping process, the object's intensity profile (solid black curve) is sampled at various positions and integrated over one pixel size p. The vertical bars represent the intensity that is recorded in each detector pixel. After sorting of the recorded raster-stepping images an image is obtained with pixel size of p/n that can be described by spatially oversampling the sample structures with respect to the detector pixels. A Richardson-Lucy deconvolution step is performed to restore the latent XDM image (e).

8.2 Determination of the PSF in oversampled images

Considering the oversampling and the following deconvolution steps in XDM one needs to exactly know the underlying PSF of the imaging system. Despite the small physical pixel size $p = 55\ \mu\mathrm{m}$ the PSF of the used *MEDIPIX3RX*-based detector system can be shown to be sufficiently close to a box-function when operated in CSM. Due to the spatial symmetry of the detector pixels, the required PSF can be characterized by a single one-dimensional (1D) line-spread function (LSF), extending the along the detector rows and columns:

$$LSF(x) \cong \begin{cases} 1 & \text{if } |x| \leq p/2 \\ 0 & \text{otherwise,} \end{cases} \tag{8.3}$$

where x is the pixel coordinate on the detector. The resulting PSF is then described by a two-dimensional box function with symmetry in the x- and y-direction.

To verify the assumption of a box-like PSF obtained after the PCD-based charge-sharing correction, we have measured the LSF according to the widely used slanted-edge method [Samei1998]. We used a $0.5\,\mathrm{mm}$ thick Gd foil as edge device, placed directly in front of the detector at an angle of approx. 2° with respect to the detector columns. The edge images were processed following the procedure outlined in [Samei1998] to obtain the pre-sampling modulation-transfer function (MTF)[3]. The left plot in figure 8.2 shows the spatial extent of the observed line spread function along a detector row in units of the pixel size p. Comparing the experimental data to a fit of a box function, the assumption of a box-like PSF seems justified.

The shape and distribution of image noise in the reciprocal space given by the noise-power spectrum (NPS) can also be used to characterize the sharpness of the detector PSF. Therefore, the NPS was measured in a flat region of the images with no object present according to the method in [Garcia-Molla2011]. Any extent of the PSF across pixel borders would result in an effective blurring of the intensity detected in neighboring pixels. Therefore, short-range correlations in the vicinity of the Nyquist frequency $f_{\mathrm{Ny}} = \frac{1}{p}$ with pixel size p would be introduced that lead to a reduced noise density at the associated spatial frequencies. Accordingly, detectors with a broad PSF exhibit a drop-off of the NPS towards f_{Ny}.

[3] Pre-sampling refers to the theoretical MTF of the image prior to the sampling of the object with the physical detector pixels with finite pixel size. Thus, the obtained MTF is treated as continuous function and extends beyond the spatial frequencies associated with the pixel size.

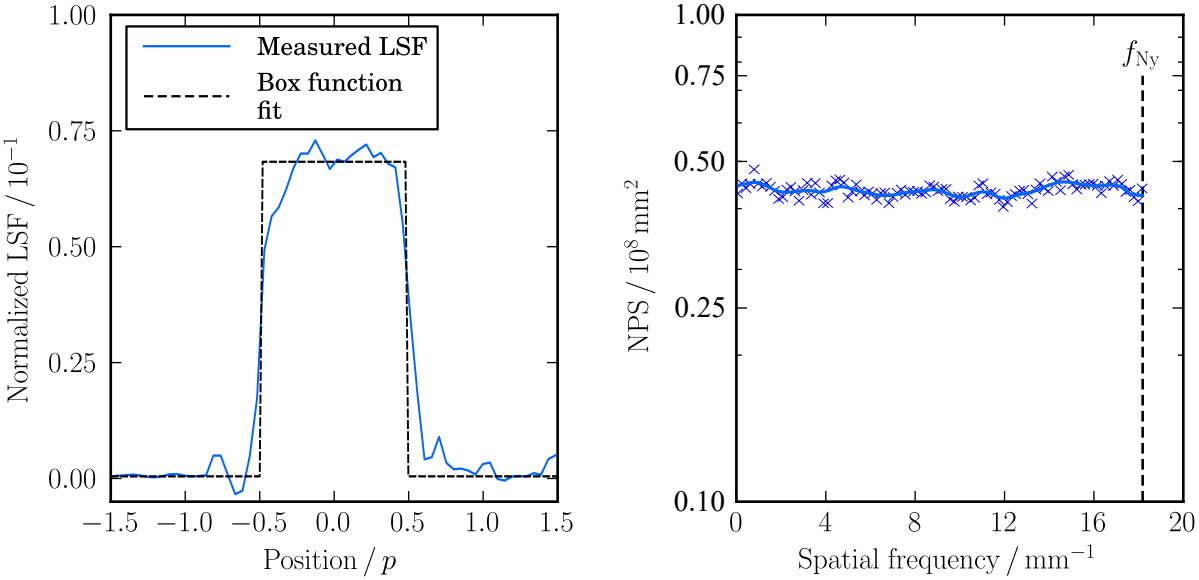

Figure 8.2: **Experimentally measured LSF and NPS of a *MEDIPIX3RX*-based PCD.** The left plot shows the determined LSF along the pixel columns of the *MEDIPIX3RX*-based *LAMBDA* detector in charge summing mode, assembled with a 300 µm thick Si sensor biased with 100 V (solid line). The LSF was obtained using the slanted-edge method. As a reference, the fit of the data to a box-like LSF with a width of one pixel is also shown (dashed line). Furthermore, the flat NPS shown in the right panel also indicates a box-like PSF since detector-caused blurring leads to an effective averaging between neighboring pixels. This would result in a drop-off of the NPS at higher spatial frequencies close to the Nyquist frequency f_{Ny}.

In the case of the used PCD with charge-sharing correction however, the obtained NPS is flat over the complete range of spatial frequencies. This behavior underlines again the box-like characteristics of the PSF.

Other studies have also been presented on the resolution characteristics of a *MEDIPIX3RX*-based PCD equipped with a GaAs x-ray sensor. There the authors have reported a MTF that appears not to be related to a box-like PSF [Hamann2015]. However, this result can be explained in part by the fact that GaAs sensors produce x-ray fluorescence which also degrades the spatial resolution and cannot be fully compensated by the CSM. Another issue affecting the obtained PSF in the aforementioned publications is the fact that a Gaussian model was employed to fit the measured PSF data to mitigate noise effects. This imposes a specific behavior on the resulting MTF curve, particularly a faster decay at higher spatial frequencies. For the investigations presented here, no a-priori assumptions were made and the PSF together with the resulting MTF have been directly obtained from the measured data.

To guarantee validity of these results the influence of the finite x-ray source size must be negligible. This influence can be described by the geometrical unsharpness Δ given by

$$\Delta = \frac{s \cdot d}{o} = (M-1) \cdot s \,, \tag{8.4}$$

where s is the source size, o the source-to-object distance, d the object-to-detector distance and M is the geometric magnification achieved by the set-up.The blurring that is introduced by the geometrical unsharpness should vanish within the noise floor of the detector images. In practice, the condition of sufficiently small Δ is realized by maximizing o and minimizing d. In the studies presented here, an x-ray tube with a geometrical source size of $0.4 \times 0.4\,\mathrm{mm}^2$ was used, operated constantly at $40\,\mathrm{kV}/30\,\mathrm{mA}$. The full length of the x-ray hutch was exploited placing the detector at a distance of 2.1 m from the source and the object 15 mm in front of the PCD. This geometry resulted in an unsharpness of $\Delta = 2.9\,\mu\mathrm{m}$ or $5.3\,\%$ of the pixel size and could therefore safely be neglected.

Now, the full PSF imposed on the raster-scanned super-resolution images can be determined. After n-fold raster-scanning, the pixel size in the XDM image becomes $p_{\mathrm{XDM}} = p/n$ and the LSF imposed on the latent XDM image is estimated to be again a box-function but with a width of n pixels in the XDM image space:

$$LSF_{XDM}(x) \cong \begin{cases} 1 & \text{if } |x| \leq n\mathrm{p}_{\mathrm{XDM}}/2 \\ 0 & \text{otherwise.} \end{cases} \tag{8.5}$$

To obtain a PSF in the raster-scanned images with the spatial extent of exactly $n\mathrm{p}_{\mathrm{XDM}}$ in both the x- and y-direction, it is crucial to ensure a sufficient positioning accuracy of the linear stages used to perform the raster-scanning. Equation 8.5 relies on a equidistant and reproducible raster-scanning of the sample. Any uncertainty in the positioning of the sample will result in a un-isotropic PSF and will therefore decrease the achievable resolution. If not properly accounted for, such inaccuracies may cause the deconvolution process to fail.

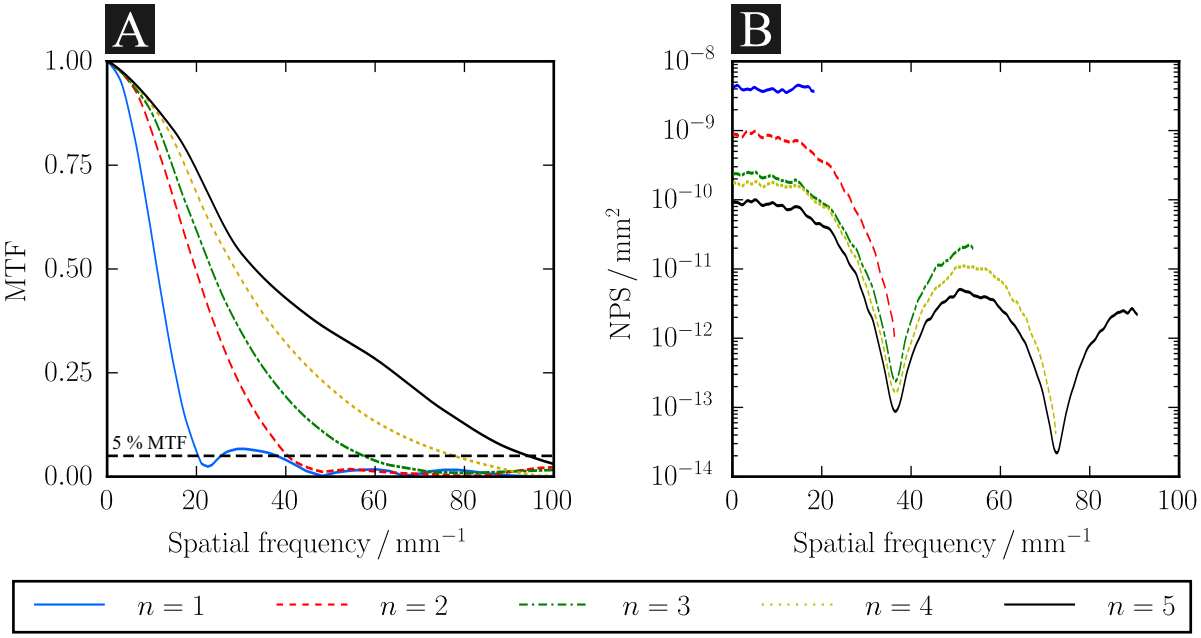

Figure 8.3: **MTF and NPS obtained with XDM at different scanning parameters n.** (A) Shows the measured MTF for different values of n. For larger n an increased contrast is observed for larger spatial frequencies indicating higher resolution. The dashed black line marks the limit of 5 % of the MTF used to quantify the resolution. The NPS associated with the images is shown in plot (B). For $n \geq 2$ the curves show oscillations that are imprinted to the noise spectrum during deconvolution by the box-like PSF.

8.3 Experimental characterization of x-ray deconvolution microscopy

Measurement of limit resolution in XDM images

XDM images of the slanted edge were acquired for $1 \leq n \leq 5$ with constant exposure time in each scanning step.

In figure 8.3 A, the measured MTF is shown for $n = 1, 2, \ldots, 5$. Only the MTF of the single-step image with $n = 1$ shows the typical behavior expected for a box-like PSF. Several oscillations following a $sinc(pf)$ curve with the pixel size p and the spatial frequency f can be observed in this case. The MTF associated with XDM images has a faster decay and the obtained contrast in the images is not completely equivalent to the case of a detector with box-like pixels of size p/n. This arises from the fact that the deconvolution step cannot perfectly restore the sub-pixel image due to the noise present in the recorded

images. The well known noise amplification that is inherent to most maximum-likelihood algorithms leads to mid-frequency noise[4] that degrades the MTF in the deconvolved images. Furthermore the performance of the deconvolution is examined by calculating the NPS for each number n of sampling steps (figure 8.3 B). The curves for each value of n end at the associated spatial Nyquist frequency $f_{\mathrm{Ny},n} = n/p$. The shape of the curve for $n = 1$ resembles a box-like detector pixel has already been discussed in section 8.2. In contrast, the NPS curves in XDM images are strongly non-linear with oscillations similar to the $sinc()$ behavior found in the MTF of a box-like pixel. This analogy can be understood by taking the actual decomposition process into account. In the Richardson-Lucy algorithm, a divison of the initial over-sampled but blurred image by the PSF that is obtained for suitable n using equation 8.5. Iteratively applying this process, the shape of the PSF is also imprinted onto the noise structure. To determine the NPS in the Fourier transform of the deconvolved XDM images is taken, leading to the oscillating behavior following the box boundaries. Additionally, the overall drop of the NPS observed for XDM suggests small-range correlations between neighboring XDM pixels consistent with the observations that we have described for the MTF.

The obtained resolution in terms of the smallest visible structure size R_{lim}, the 5% MTF criterion was applied to the measured curves of the XDM images. The observed MTF value should go to zero close to the frequency $\frac{n}{p}$ that corresponds to one XDM-pixel pitch. The resulting values are visualized in figure 8.4. Fitting the data with a hyperbolic function proves that in the given range, the parameter n clearly determines the achievable resolution R_{lim}:

$$R_{\mathrm{lim}} = p/n, \tag{8.6}$$

where p is the original pixel size and we expect this result to hold true even for larger n. Larger values of $n > 5$ could not be investigated using the particular experimental set-up since the used linear stages for raster-scanning[5] only guarantee a reproducible positioning accuracy in the rage of $12\ \mu\mathrm{m}$. Note that in figure 8.4 the resolution limit determined by the 5% MTF criterion is typically located below the Nyquist limit for the given pixel size. Hence, aliasing might already be seen in this frequency range, depending on the orientation and shape of the imaged pattern.

Additionally, the amount of noise present in the image was determined. For each n, an image region in the background excluding any objects was selected and the standard deviation of the intensities relative to the mean value in this region was measured and plotted as the bar chart in figure 8.4. In our study

[4] In the case of the Richardson-Lucy algorithm, several pixel wide speckles are often observed
[5] LTM 120-400, OWIS GmbH

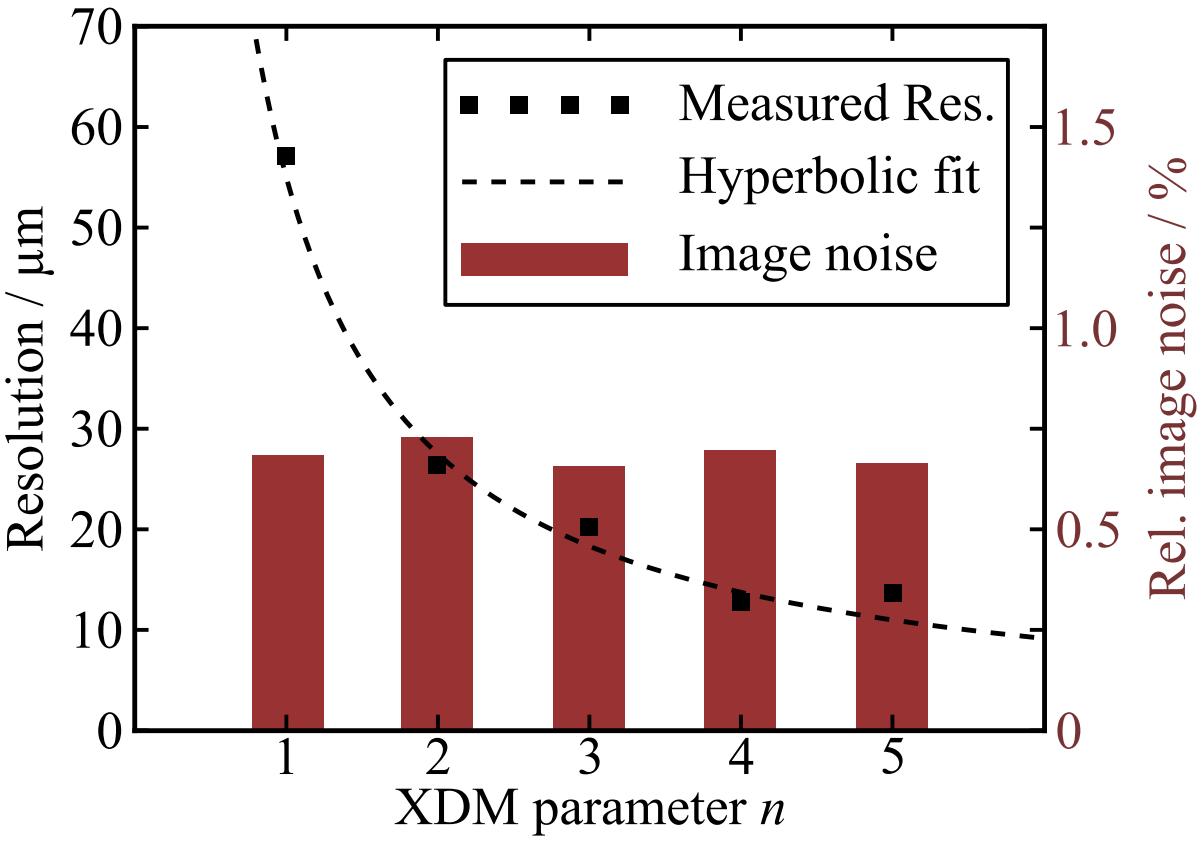

Figure 8.4: **Limit resolution and noise in XDM images.** The left axis in black shows the resolution limit obtained at 5% MTF. The red bars indicate the amount of noise relative to the background intensity (right axis), depending on n. The minimum feature size decreases hyperbolically with n, whereas the noise does not depend on the XDM parameter.

the overall level of noise did not depend on the XDM parameter but stayed constant at approximately $0.7\,\%$ of the background image intensity. Due to keeping the exposure time constant at each of the $n \times n$ scanning steps, the photon statistics in each 'pixel' of the XDM images did not change compared to the reference image. At the same time the total exposure time and x-ray dose to obtain a full XDM image increases with the same factor $n \times n$. The deconvolution step evidently does not introduce a bias to the overall noise level in flat image regions. However, the spatial structure of the noise pattern might be altered as discussed for the NPS curves.

Previous attempts to obtain sub-pixel resolution in x-ray imaging utilizing photon-counting or integrating detectors with sub-pixel raster-scanning yielded a much smaller increase of resolution as n becomes larger. Furthermore, saturation of achieved sub-pixel resolution at higher raster-scanning parameters has typically been reported until now. This is mostly due to the fact that previous implementations did not

model the spatial response of the used detector system and thus could not incorporate an appropriate deconvolution step [Bodensteiner2009, Thim2011]. Most detectors available today have a gaussian-shaped PSF which is significantly wider than one pixel arising mostly from charge sharing in directly converting sensors or lateral propagation of light in scintillators coupled to EIDs. In principle, the resulting PSF after the raster-scanning can also be deduced for such systems. However, deconvolution becomes more prone to noise amplification due to the higher number of iterations necessary for the algorithm to converge. In addition, the MTF associated with a gaussian PSF drops faster compared to PCDs with a box-like behavior. Therefore, information about high-frequency features in the object is preserved better in images obtained with a box-like PSF. Considering radiation exposure and the obtained CNR, the x-ray dose required to resolve such features therefore increases strongly in applications with a gaussian PSF, although the high-frequency structures can generally also be enhanced in such systems via deconvolution. This results in practical limitations when applying gaussian PSF detectors in high-resolution biomedical x-ray imaging where radiation exposure is a critical limiting factor. Hence, the nearly box-like PSF offered by some recent PCDs able to correct charge-sharing is one key feature for the XDM method since access to higher spatial frequencies becomes much more efficient.

Projection microscopy of a Siemens-star

The capability of the proposed XDM method to enable x-ray projection microscopy will be demonstrated using a Siemens star. Such an object consist of a radial pattern of strongly attenuating lines arranged on a circular path where the line-density increases towards the center of the circle. A photograph of the used Siemens star can be seen in figure 8.5. The object consists of a cut-out Pb foil with a thickness of $50\,\mu$m embedded between two $1\,$mm acrylic plates. Spatial frequencies ranging from $0.5\,$lp/mm to $11.5\,$lp/mm are available within the structure.

To resolve the line pattern down to the lowest present spacial frequency at the center of the object, the star was imaged with an raster-scanning factor of $n = 3$. Together with the used PCD this parameter choice yields an XDM pixel-size of approximately $18\,\mu$m and is sufficient to completely resolve a single line with a width of $43\,\mu$m at the star's center. Figure 8.6 provides an comparison of the images in the center region obtained from a standard radiography with pixel size $55\,\mu$m and $n = 1$ (A), a raster-scanned image without deconvolution (B) and the XDM image (C). Comparing the line patterns near the center of the star, XDM is able to easily resolve the complete structure in the image while aliasing is becomes visible in the standard image. The raster-scanning image without deconvolution already yields an improvement in terms of resolution, however it is still strongly affected by correlations between pixels and therefore suffers from lack of contrast.

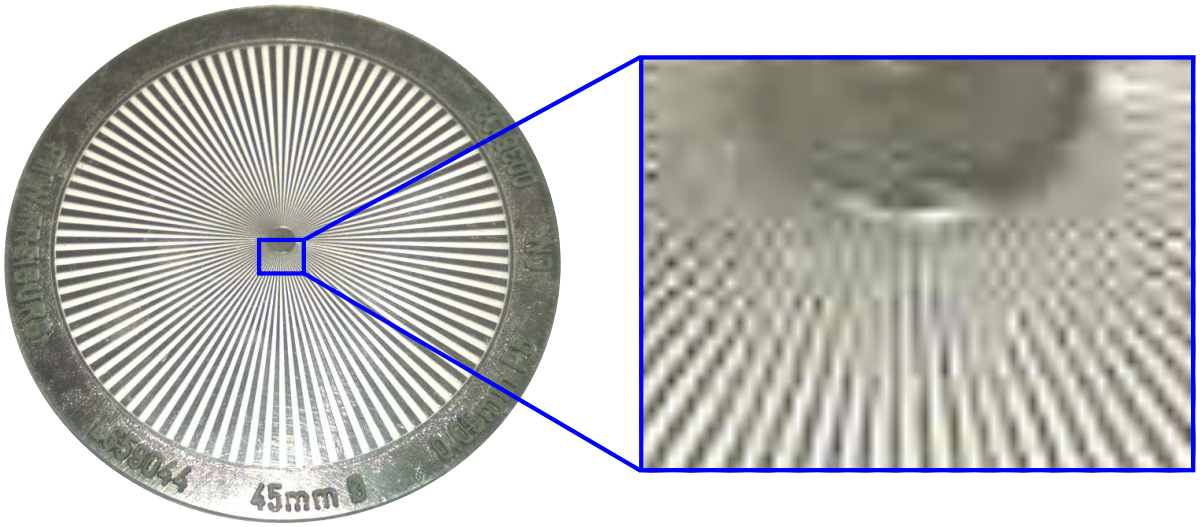

Figure 8.5: **Photograph of the Siemens star used to assess XDM projection microscopy.** The spatial frequencies of the radial line pattern range from 0.5 lp/mm at the edge to 11.5 lp/mm close to the center of the star. The magnified view of the center shows the region that was used to assess the image quality of the XDM images. Aliasing of the structures is already seen in the photography image in this figure.

To illustrate the effect of exploiting the complete XDM approach, the plot in figure 8.6 shows a comparison of the obtained patterns along the central segments of the marked lines in the three images. Spacial frequencies of the line-pattern are increasing towards the center of the line, reaching a value of 11.5 lp/mm. The XDM image shows significantly improved contrast over a wide range of frequencies. Especially for the higher frequencies, this results in a largely improved CNR and therefore, XDM has an improved resolution limit than the corresponding raster-scanned image without deconvolution or the standard radiography.

Micro-CT of a chicken bone

A chicken bone sample was imaged using XDM-CT with a 1D scanning factor of $n = 5$ perpendicular to the rotation axis. The total diameter of the bone sample was approximately $5.5 \times 7.5\,\mathrm{mm}^2$. According to the 1D raster-scanning the voxel size within a given CT slice is decreased to $11\,\mu$m while the slice thickness is kept at the original pixel size. In a step-and-shoot acquisition, the total measurement time amounted to approximately 12 hours while 1400 projections were recorded. The total exposure time was fractioned equally between each of the raster-scanning steps. By re-binning the raster-scanned images a reference image was reconstructed with resolution of the original pixel size $p = 55\,\mu$m and a 5-fold

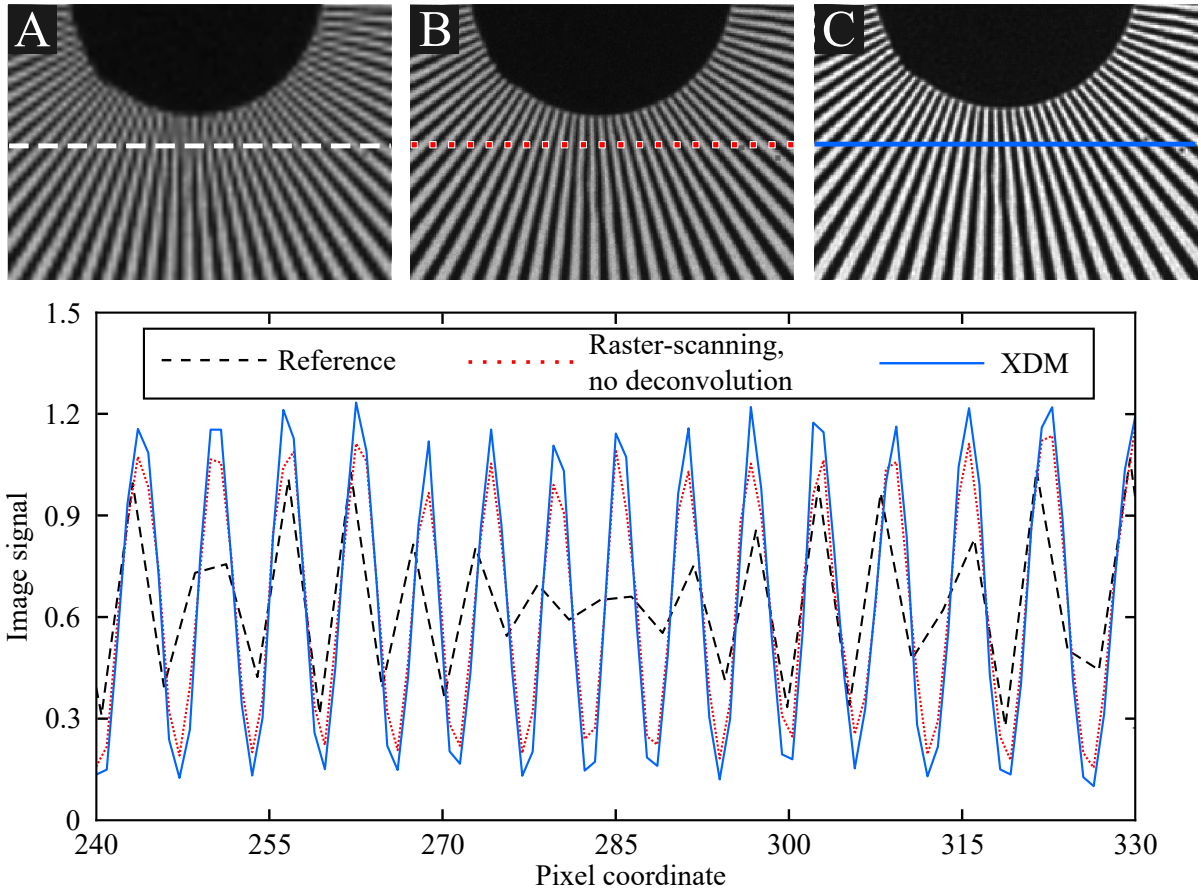

Figure 8.6: **Results of the super-resolution imaging of the Siemens-star phantom based on the XDM method.** The region at the center of the star is shown by means of a standard radiography image using $n = 1$ as reference (A), a raster-scanned image using $n = 3$ without deconvolution (B) and the complete XDM method (C). The plot below the images gives a quantitative comparison between the obtained amplitudes along the central parts of the marked line patterns in A – C. One feature of the XDM images is the superior contrast. In the standard image, structure aliasing is clearly visible, as the amplitude drops to zero for the highest spatial frequencies in the range of up to 11.5 lp/mm.

increased photon count statistic.

As figure 8.7 shows, the XDM image is again superior in terms of contrast-to-noise ratio and resolution regardless of the lower counting statistics in each scan step that contributed to the image.

Comparing our CT results to other work presented in the literature, it should be noted that an adapted pixel model in iterative CT reconstruction (detector supersampling) can produce super-resolved images at constant radiation exposure [VanAarle2014]. However, the algorithmic formulation of the super-

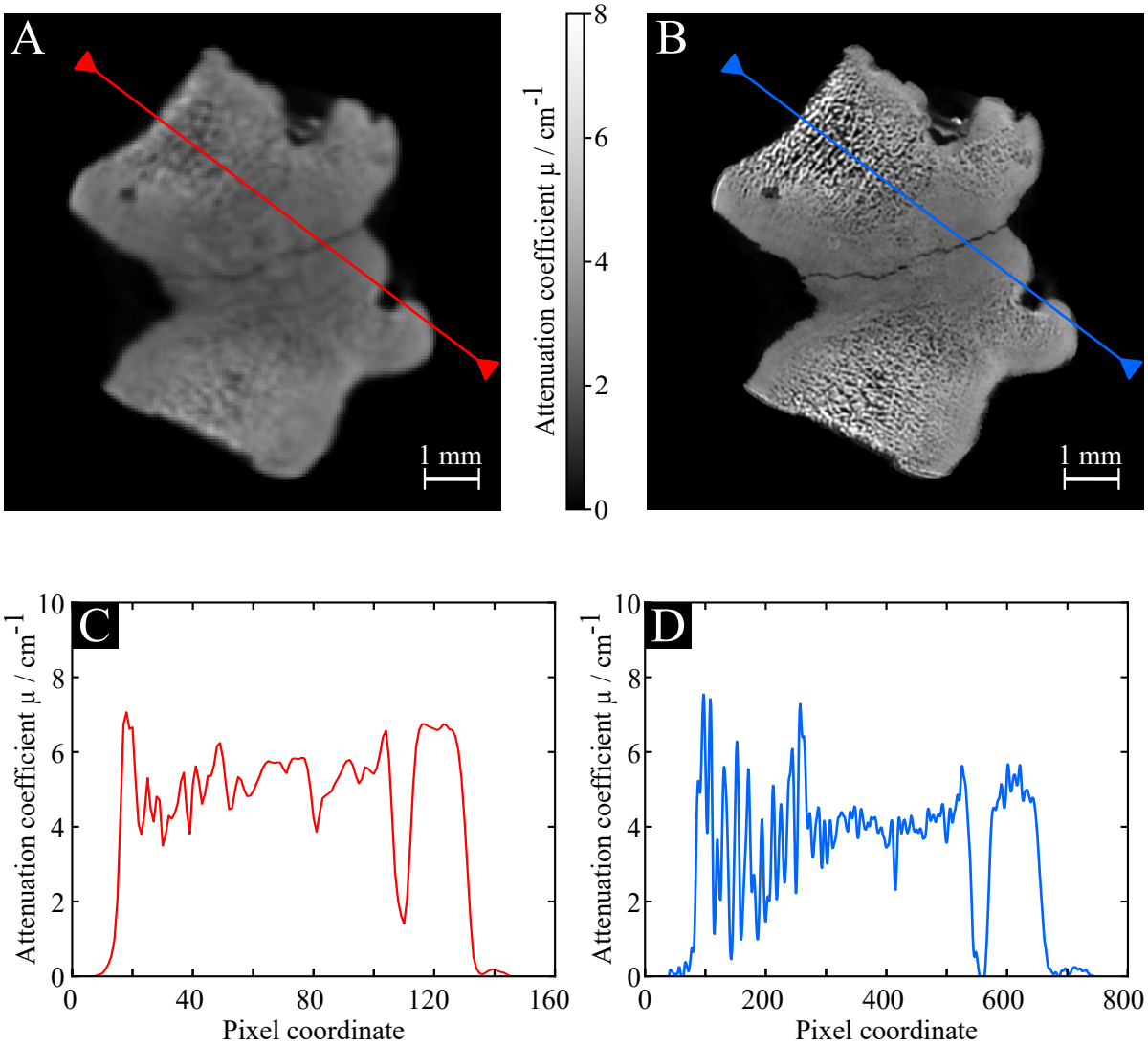

Figure 8.7: **XDM-CT images of a chicken bone sample obtained using** 40 kVp**.** A standard image ($n = 1$) with increased photon count statistic was reconstructed after re-binning of the raster-scans (A). The XDM image using $n = 5$ steps is shown in B. Despite the five-fold increase in photon counts per pixel, the standard image shows reduced feature resolution and contrast compared to the XDM image.

resolution reconstruction in [VanAarle2014] requires prior knowledge or assumptions about the sample composition or density and does not allow for great variations of this value across the sample. Therefore, this method can only be applied to the imaging of binary objects or at least objects consisting of homogeneous materials such as micro-CT of bone. For general-purpose CT images, the proposed XDM method is expected to yield improved results as is does not depend on any a-priori knowledge or

assumption about the object's composition.

8.4 Further improvements to the XDM method

As a generalization of the method, it would possible to combine XDM with the geometric magnification of a cone-beam geometry. This scenario could have two major implications:

First, to reach a given resolution in micro-CT a smaller geometric magnification factor is required in combination with XDM. The scanning FOV would be strongly increased especially in applications where the object's size limits the source-to-isocenter distance. As an example, a combination of a fairly moderate geometric magnification of $M = 5$ and an XDM parameter of $n = 4$ realized in a set-up using a PCD with a common pixel size in the order of $100\,\mu m$ would already be sufficient to obtain a resolution of $5\,\mu m$. In a conventional approach without employing XDM, at least a value of $M = 20$ would be required, which results in an unsharpness in the order of one or more detector pixels due to the source blurring and lowers the overall image contrast. Using XDM instead will result in much sharper images, since the inherent unsharpness is limited to a small fraction of the actual pixel size. Smaller geometric magnification would also relax the requirements on the x-ray source. This allows for the use of more robust and cheaper source technology in micro-CT equipment.

As a second scenario, a combination of a high geometric magnification and subsequent XDM with highly accurate steps using e.g. piezoelectric sample positioning equipment might provide resolution in the nanometer regime. Therefore however, the PSF no longer has a box shape and the blurring effect from the x-ray source also needs to be considered. However, if the exact form and size of the focal spot is known and the source is sufficiently stable, such effects might be incorporated into a more sophisticated super-resolution reconstruction algorithm.

9 Summary & Outlook

The focus of the presented work was set on the use of photon-counting detectors in spectral x-ray imaging techniques.

The theory of spectral imaging and photon counting detectors is briefly recapitulated in the chapters 2 and 3. From measurements in two or more energy bins, information about the underlying composition of the sample in terms of the basic physical interaction processes (photoelectric absorption, scattering) can be inferred. Thereby, spectral images tend to exhibit increased noise due to noise propagation and noise in different spectral basis images can be shown to be anti-correlated. Besides their ability to divide the incident x-ray spectrum into several energy bins, PCDs can provide better SNR by equal weighting of all photons and the absence of dark current. Thereby, the distribution of photon counts is purely Poisson and the dynamic range of the detector is extended down to zero photons.

In chapter 4 a clinical state-of-the-art dual energy CT scanner was evaluated in terms of image quality and quantitative accuracy. This system is based on a recently introduced dual-layer detector concept offering single-shot acquisitions of spectral projection data at each projection angle and the presented measurements constitute the first in-depth characterization of this system. Thereby, a baseline for the performance of today's spectral imaging methods was set. The overall accuracy was high enough to recover spectral imaging parameters (energy-dependent attenuation, contrast agent and effective atomic numbers) with only a few percent bias and often exceeds the performance reported in the available literature for other dual-energy systems. Explicitly worth mentioning is the behavior of CNR and noise in VMIs. Following explicit consideration of anti-correlation of basis material images in the projection space. Thereby, the noise curve is seemingly independent on VMI energy and only increases slightly towards very low energies. Thereby, the CNR increases continuously towards lower energies yielding more than two-fold improvement over the conventional images. This is to the best of our knowledge the first observation of this behavior in VMI.

Chapter 5 gives an introduction to a simulation framework developed during this thesis to model spectral imaging based on PCDs. With the background of still low availability and high cost of PCD systems, many research applications benefit from the ability to properly predict the performance in specific imaging tasks and thereby optimize the system design. Employing a CRLB analysis of the imaging system based on a detailed and viable model for the spectral response function of the detectors, many parame-

ters like the source spectrum, optimal energy threshold settings and calibration range can be optimized. Furthermore, accurate simulation of images acquired using PCDs can assist in the development and benchmarking of advanced spectral image reconstruction and postprocessing algorithms.
One key factor limiting the use of projection-based material decomposition in spectral x-ray imaging is the requirement for extensive calibration or characterization efforts of the complete imaging system. Therefore a new semi-empirical forward-model for spectral imaging was developed and discussed in chapter 6. The model termed PLB is based on approximating the polychromatic x-ray spectrum by a small set of discrete energies that are chosen such that the count number in each energy bin is accurately reproduced with deviations significantly less than $1\,\%$ in simulation studies. Thereby the amount of required calibration measurements could be reduced to a minimum and reliable decomposition results could be obtained using less than 10 calibration points while offering good extrapolation properties when the sample line-integrals exceed the calibrated range. MLE-based material decomposition using the PLB model yields unbiased estimates for basis material line-integrals and achieves the CRLB. Therefore we expect especially pre-clinical and micro-CT applications to benefit from the new model since frequent changes in the set-up configuration require repeated re-calibration.
The techniques developed so far have been applied to various samples from a clinical and material scientific context in experimental studies involving a commercial PCD with energy discrimination capability. In chapter 7 the quantitative accuracy in the PLB model was evaluated experimentally yielding results within a few percent of the nominal values of the material properties ρ_{el} and Z_{eff}. A large portion of the inaccuracies can be attributed to drifts of the detector's spectral response over time and the influence of scattered radiation on the spectral basis material images. Especially applications in the material science and NDT area showed very promising results concerning the reduction of beam-hardening artifacts and CNR enhancement in spectral CT.
Finally unique features of PCDs other than spectral resolution were investigated in terms of potential novel applications in x-ray imaging. Chapter 8 presents a new approach to x-ray microscopy exploiting the box-like shape of the PSF in detectors offering on-chip charge sharing correction. After a n-step raster scanning of the sample, deconvolution of the acquired images with the exactly predictable and sharp PSF is able to recover images with sub-pixel resolution. The achievable resolution is shown to be proportional to n which outperforms similar methods reported so far where the final resolution was reported to saturate after a small number of n. This approach could have many possible applications ranging to ultra-high resolution imaging in material science to clinical application requiring visualization of fine details, e. g. micro-calcification in mammography.

Besides further refinements to spectral imaging methods, future challenges will involve the identification of applications where PCD-based imaging will provide the biggest improvement in terms of

image quality and ideally make available image information that was formerly not accessible using conventional imaging approaches. The most promising among such applications is the use of multiple contrast agents that can be distinguished from one another via their different absorption edges. As an example, two contrast agents (Gd and I) can be employed to identify neoplastic masses in CT colonography [Muenzel2016]. In pre-clinical research, different functionalized stains that bind to specific types of biological tissues or metabolites can be labeled using multiple high-Z elements. Thereby, images much like in classic histology can be obtained, however in a non-destructive way and in 3D [Schirra2014a, Silva2015, Handschuh2017].
In order to enable wide-spread use of PCD-based spectral imaging by providing high quality basis material images, elaborate postprocessing is typically required to reduce noise amplification during material decomposition. Today's approaches typically separate the processes of material decomposition, tomographic reconstruction and de-noising while many still operate in image space. However, the statistical information present in the tomographic measurements could be exploited better when those processes are performed jointly. Recently, preliminary results have been presented [Mechlem2016] of a joint material decomposition and statistical iterative reconstruction (SIR) using a statistical model of the acquired projections. Such methods work both in projection and image space and can fully exploit all available information, leading to significantly improved image quality. Especially for low-dose scans, state-of-the-art spectral systems are limited by statistical bias [Rajbhandary2015]. Joint SIR can help to overcome this limit, but has to be benchmarked thoroughly in future studies. In SIR noise is suppressed by penalizing small-scale differences between reconstructed values in neighboring pixels. This procedure is known as regularization and should result in a more or less smooth appearance while preserving edges from real image features. Future research into the application of SIR in spectral imaging will need to address the problem of regularization. As distinct features in the objects do not necessarily occur in all basis material images altogether, cross-talk between basis material images can then occur. It is still an open question today how a joint regularization of all basis material images should be performed to limit such a cross-talk.

As pointed out at several occasions throughout this thesis, spectral x-ray imaging makes basic material properties like the electron density directly accessible. Besides material decomposition based on energy discrimination, x-ray phase contrast and dark-field imaging also yield information about an object's electron density and scattering power [Pfeiffer2006, Pfeiffer2008, Sarapata2014]. It has already been demonstrated that those techniques also benefit strongly from spectral information provided by PCDs in terms of CNR enhancement and artifact reduction [Weber2011, Pelzer2013]. A fully spectral MLE comparable to equation 2.28 has been presented in [Epple2015] for the electron density based on x-ray phase contrast measurements in several energy bins. However, noise propagation and correlation in phase-contrast images is fundamentally different from spectral attenuation-based imaging [Koehler2011]. By

properly modeling the statistical behavior of each measurement these differences could be exploited jointly to improve image quality and quantitative accuracy for both settings. Therefore, both methods will potentially benefit from a joint estimation of material properties in a spectral x-ray phase contrast set-up available in the future.

Bibliography

[Alles2007] J. Alles and R. F. Mudde. "Beam hardening: Analytical considerations of the effective attenuation coefficient of x-ray tomography". *Med. Phys.*, **34**(7): 2882, **2007**.

[Altman2009] A. Altman and R. Carmi. "TU-E-210A-03: A Double-Layer Detector, Dual-Energy CT — Principles, Advantages and Applications". *Med. Phys.*, **36**(6): 2750, **2009**.

[Alvarez1979] R. Alvarez and E. Seppi. "A Comparison of Noise and Dose in Conventional and Energy Selective Computed Tomography". *IEEE Trans. Nucl. Sci.*, **26**(2): 2853, **1979**.

[Alvarez2011] R. E. Alvarez. "Estimator for photon counting energy selective x-ray imaging with multibin pulse height analysis." *Med. Phys.*, **38**(July): 2324, **2011**.

[Alvarez2015] R. E. Alvarez. "Efficient, non-iterative estimator for imaging contrast agents with spectral x-ray detectors". *IEEE Trans. Med. Imaging*, **0062**(c): 1, **2015**.

[Alvarez1976] R. E. Alvarez and A. Macovski. "Energy-selective reconstructions in X-ray computerised tomography". *Phys. Med. Biol.*, **21**(5): 733, **1976**.

[Anghinolfi1992] F. Anghinolfi, P. Aspell, K. Bass, W. Beusch, L. Bosisio, C. Boutonnet, P. Burger, M. Campbell, E. Chesi, C. Claeys, J. Clemens, M. Cohen Solal, I. Debusschere, P. Delpierre, D. Di Bari, B. Dierickx, C. Enz, E. Focardi, F. Forti, Y. Gally, M. Glaser, T. Gys, M. Habrard, E. Heijne, L. Hermans, R. Hurst, P. Inzani, J. Jaeger, P. Jarron, F. Krummenacher, F. Lemeilleur, V. Lenti, V. Manzari, G. Meddeler, M. Morando, A. Munns, F. Nava, F. Navach, C. Neyer, G. Ottaviani, F. Pellegrini, F. Pengg, R. Perego, M. Pindo, R. Potheau, E. Quercigh, N. Redaelli, L. Rossi, D. Sauvage, G. Segato, S. Simone, G. Stefanini,

G. Tonelli, G. Vanstraelen, G. Vegni, H. Verweij, G. Viertel and J. Waisbard. "A 1006 element hybrid silicon pixel detector with strobed binary output". *IEEE Trans. Nucl. Sci.*, **39**(4): 654, **1992**.

[Anghinolfi1992a] F. Anghinolfi, P. Aspell, K. Bass, W. Beusch, L. Bosisio, C. Boutonnet, P. Burger, M. Campbell, E. Chesi, C. Claeys, J. Clemens, M. Cohen Solal, I. Debusschere, P. Delpierre, D. Di Bari, B. Dierickx, C. Enz, E. Focardi, F. Forti, Y. Gally, M. Glaser, T. Gys, M. Habrard, E. Heijne, L. Hermans, R. Hurst, P. Inzani, J. Jaeger, P. Jarron, F. Krummenacher, F. Lemeilleur, V. Lenti, V. Manzari, G. Meddeler, M. Morando, A. Munns, F. Nava, F. Navach, C. Neyer, G. Ottaviani, F. Pellegrini, F. Pengg, R. Perego, M. Pindo, R. Potheau, E. Quercigh, N. Redaelli, L. Rossi, D. Sauvage, G. Segato, S. Simone, G. Stefanini, G. Tonelli, G. Vanstraelen, G. Vegni, H. Verweij, G. Viertel and J. Waisbard. "Design and performance of the Omega-ion hybrid silicon pixel detector". In 6th Eur. Symp. Semicond. Detect., 1–15. **1992**.

[Ballabriga2013] R. Ballabriga, J. Alozy, G. Blaj, M. Campbell, M. Fiederle, E. Frojdh, E. H. M. Heijne, X. Llopart, M. Pichotka, S. Procz, L. Tlustos and W. Wong. "The Medipix3RX: a high resolution, zero dead-time pixel detector readout chip allowing spectroscopic imaging". *J. Instrum.*, **8**(02): C02016, **2013**.

[Ballabriga2016] R. Ballabriga, J. Alozy, M. Campbell, E. Frojdh, E. H. M. Heijne, T. Koenig, X. Llopart, J. Marchal, D. Pennicard, T. Poikela, L. Tlustos, P. Valerio, W. Wong and M. Zuber. "Review of hybrid pixel detector readout {ASICs} for spectroscopic {X}-ray imaging". *J. Inst.*, **11**(01): P01007, **2016**.

[Ballabriga2011] R. Ballabriga, M. Campbell, E. Heijne, X. Llopart, L. Tlustos and W. Wong. "Medipix3: A 64k pixel detector readout chip working in single photon counting mode with improved spectrometric performance". *Nucl. Instruments Methods Phys. Res. Sect. A Accel. Spectrometers, Detect. Assoc. Equip.*, **633**: S15, **2011**.

[Ballabriga2009] R. Ballabriga, W. Wong and X. Llopart. "Medipix3 manual". **2009**.

[Bamberg2011] F. Bamberg, A. Dierks, K. Nikolaou, M. F. Reiser, C. R. Becker and T. R. C. Johnson. "Metal artifact reduction by dual energy computed tomography using monoenergetic extrapolation." *Eur. Radiol.*, **21**(7): 1424, **2011**.

[Bell1974] R. O. Bell, G. Entine and H. B. Serreze. "Time-dependent polarization of CdTe gamma-ray detectors". *Nucl. Instruments Methods*, **117**(1): 267, **1974**.

[Bennett2014] J. R. Bennett, A. M. T. Opie, Qiong Xu, Hengyong Yu, M. Walsh, A. Butler, P. Butler, Guohua Cao, A. Mohs and Ge Wang. "Hybrid Spectral Micro-CT: System Design, Implementation, and Preliminary Results". *IEEE Trans. Biomed. Eng.*, **61**(2): 246, **2014**.

[Bodensteiner2009] C. Bodensteiner, C. Darolti and A. Schweikard. "Achieving super-resolution X-ray imaging with mobile C-arm devices". *Int. J. Med. Robot.*, **5**: 243, **2009**.

[Bonnin2014] A. Bonnin, P. Duvauchelle, V. Kaftandjian and P. Ponard. "Concept of effective atomic number and effective mass density in dual-energy X-ray computed tomography". *Nucl. Instruments Methods Phys. Res. Sect. B Beam Interact. with Mater. Atoms*, **318**: 223, **2014**.

[Boone1997] J. M. Boone, T. R. Fewell and R. J. Jennings. "Molybdenum, rhodium, and tungsten anode spectral models using interpolating polynomials with application to mammography." *Med. Phys.*, **24**(12): 1863, **1997**.

[Boone1997a] J. M. Boone and J. a. Seibert. "An accurate method for computer-generating tungsten anode x-ray spectra from 30 to 140 kV". *Med. Phys.*, **24**(11): 1661, **1997**.

[Broennimann2009a] C. Broennimann. "CMOS Hybrid Pixel Detectors for Scientific, Industrial and Medical Applications". In APS March Meeting Abstracts. **2009**.

[Brooks1978] R. Brooks and G. Di Chiro. "Split-Detector Computed Tomography: A Preliminary Report". *Radiology*, **126**(1): 255, **1978**.

[Cardinal1990] H. N. Cardinal. "An accurate method for direct dual-energy calibration and decomposition". *Med. Phys.*, **17**(3): 327, **1990**.

[Carmi2005] R. Carmi, G. Naveh and A. Altman. "Material separation with dual-layer CT". *IEEE Nucl. Sci. Symp. Conf. Rec.*, **4**: 1876, **2005**.

[Chae2010] E. J. Chae, J. B. Seo, Y. M. Jang, B. Krauss, C. W. Lee, H. J. Lee and K.-S. Song. "Dual-Energy CT for Assessment of the Severity of Acute Pulmonary

Embolism: Pulmonary Perfusion Defect Score Compared With CT Angiographic Obstruction Score and Right Ventricular/Left Ventricular Diameter Ratio". *Am. J. Roentgenol.*, **194**(3): 604, **2010**.

[Cohen-Tannoudji2004] C. Cohen-Tannoudji, J. Dupont-Roc and G. Grynberg. Atom-Photon Interactions: Basic Processes and Applications. Wiley-VCH, Weinheim, Germany, **2004**. ISBN 9783527617197.

[Cowen2008] A. Cowen, S. Kengyelics and A. Davies. "Solid-state, flat-panel, digital radiography detectors and their physical imaging characteristics". *Clin. Radiol.*, **63**(5): 487, **2008**.

[DelSordo2009] S. Del Sordo, L. Abbene, E. Caroli, A. M. Mancini, A. Zappettini and P. Ubertini. "Progress in the Development of CdTe and CdZnTe Semiconductor Radiation Detectors for Astrophysical and Medical Applications". *Sensors*, **9**(5): 3491, **2009**.

[Delpierre2014] P. Delpierre. "A history of hybrid pixel detectors, from high energy physics to medical imaging". *J. Instrum.*, **9**(05): C05059, **2014**.

[Ehn2016] S. Ehn, F. M. Epple, A. Fehringer, D. Pennicard, H. Graafsma, P. Noël and F. Pfeiffer. "X-ray deconvolution microscopy". *Biomed. Opt. Express*, **7**(4): 1227, **2016**.

[Ehn2017] S. Ehn, T. Sellerer, D. Muenzel, A. A. Fingerle, F. Kopp, M. Duda, K. Mei, B. Renger, J. Herzen, J. Dangelmaier, B. J. Schwaiger, A. Sauter, I. Riederer, M. Renz, R. Braren, E. J. Rummeny, F. Pfeiffer and P. B. Noël. "Spectral imaging performance of a full-body dual-layer spectral Computed Tomography system". *submitted to J. Appl. Clin. Med. Phys.*, **2017**.

[Engel2008] K. J. Engel, C. Herrmann and G. Zeitler. "X-ray scattering in single- and dual-source CT". *Med. Phys.*, **35**(1): 318, **2008**.

[Epple2015] F. M. Epple, S. Ehn, P. Thibault, T. Koehler, J. Herzen, D. Pennicard, H. Graafsma, P. B. Noel and G. Potdevin. "Phase unwrapping in spectral X-ray di ff erential phase-contrast imaging with an energy-resolving photon-counting pixel detector". *IEEE Trans. Med. Imaging*, **34**(3): 816, **2015**.

[Fehringer2014] A. Fehringer, T. Lasser, I. Zanette, P. B. Noël and F. Pfeiffer. "A versatile tomographic forward- and back-projection approach on multi-GPUs". In Proc. SPIE Med. Imaging, vol. 9034, 90344F–1 – 90344F–1. **2014**. ISBN 9780819498274.

[Flannery1987] B. P. FLANNERY, H. W. DECKMAN, W. G. ROBERGE and K. L. D'AMICO. "Three-Dimensional X-ray Microtomography". *Science (80-.).*, **237**(4821), **1987**.

[Flohr2006] T. G. Flohr, C. H. McCollough, H. Bruder, M. Petersilka, K. Gruber, C. Süβ, M. Grasruck, K. Stierstorfer, B. Krauss, R. Raupach, A. N. Primak, A. Küttner, S. Achenbach, C. Becker, A. Kopp and B. M. Ohnesorge. "First performance evaluation of a dual-source CT (DSCT) system". *Eur. Radiol.*, **16**(2): 256, **2006**.

[Fuchs2013] T. Fuchs, P. Keßling, M. Firsching, F. Nachtrab and G. Scholz. "Industrial Applications of Dual X-ray Energy Computed Tomography (2X-CT)". In Nondestruct. Test. Mater. Struct., 97–103. Springer Netherlands, Dordrecht, **2013**.

[Garcia-Molla2011] R. García-Mollá, R. Linares and R. Ayala. "Study of DQE dependence with beam quality on GE essential mammography flat panel." *J. Appl. Clin. Med. Phys.*, **12**(1): 3176, **2011**.

[Graser2008] A. Graser, T. R. C. Johnson, M. Bader, M. Staehler, N. Haseke, K. Nikolaou, M. F. Reiser, C. G. Stief and C. R. Becker. "Dual Energy CT Characterization of Urinary Calculi: Initial In Vitro and Clinical Experience". *Invest. Radiol.*, **43**(2): 112, **2008**.

[Guo2012] X. Guo, S. M. Johnston, G. A. Johnson and C. T. Badea. "A comparison of sampling strategies for dual energy micro-CT". 831332. International Society for Optics and Photonics, **2012**.

[Hamann2015] E. Hamann, T. Koenig, M. Zuber, A. Cecilia, A. Tyazhev, O. Tolbanov, S. Procz, A. Fauler, T. Baumbach and M. Fiederle. "Performance of a Medipix3RX Spectroscopic Pixel Detector With a High Resistivity Gallium Arsenide Sensor". *IEEE Trans. Med. Imaging*, **34**(3): 707, **2015**.

[Handschuh2017] S. Handschuh, C. Beisser, B. Ruthensteiner and B. Metscher. "Microscopic dual-energy CT (microDECT): a flexible tool for multichannel ex vivo 3D imaging of biological specimens". *J. Microsc.*, **00**(0): 1, **2017**.

[He2013] P. He, H. Yu, J. Bennett, P. Ronaldson, R. Zainon, A. Butler, P. Butler, B. Wei and G. Wang. "Energy-discriminative performance of a spectral micro-CT system". *J. Xray. Sci. Technol.*, **21**(3): 335, **2013**.

[Horowitz1972] P. Horowitz and J. Howell. "A scanning x-ray microscope using synchrotron radiation." *Science*, **178**(61): 608, **1972**.

[Hounsfield1973] G. N. Hounsfield. "Computerized transverse axial scanning (tomography): Part 1. Description of system". *Br. J. Radiol.*, **46**(552): 1016, **1973**.

[Hsieh2010] J. Hsieh, J. Fan, N. Chandra, P. Crandall and M. Kulpins. "A Reconstruction Technique for Dual-Energy X-ray Computed Tomography". *Proc. first Int. Conf. image Form. x-ray Comput. Tomogr.*, **1**: 10, **2010**.

[Hubbell1997] J. Hubbell. "Summary of Existing Information on the Incoherent Scattering of Photons, Particularly on the Validity of the Use of the Incoherent Scattering Function". *Radiat. Phys. Chem.*, **50**(1): 113, **1997**.

[Hubbell1975] J. H. Hubbell, W. J. Veigele, E. A. Briggs, R. T. Brown, D. T. Cromer and R. J. Howerton. "Atomic Form Factors, Incoherent Scattering Functions, and Photon Scattering Cross Sections". *J. Phys. Chem. Ref. Data*, **6**(2): 615, **1975**.

[Jackson1981] D. Jackson and D. Hawkes. "X-Ray Attenuation Coefficients of Elements and Mixtures". *Phys. Rep.*, **70**(3): 169, **1981**.

[Jakubek2007] J. Jakubek. "Data processing and image reconstruction methods for pixel detectors". *Nucl. Instruments Methods Phys. Res. Sect. A Accel. Spectrometers, Detect. Assoc. Equip.*, **576**(1): 223, **2007**.

[James2000] F. James. "Statistics". *The European Physical Journal C - Particles and Fields*, **15**(1): 195, **2000**.

[Jovanovic2013] Z. Jovanović, F. Khan, F. Enzmann and M. Kersten. "Simultaneous segmen-

tation and beam-hardening correction in computed microtomography of rock cores". *Comput. Geosci.*, **56**: 142, **2013**.

[Kalender1986] W. Kalender, W. Perman, J. Vetter and E. Klotz. "Evaluation of a prototype dual-energy computed tomographic apparatus. I. Phantom studies." *Med. Phys.*, **13**(3): 334, **1986**.

[Kalender1990] W. Kalender, W. Seissler, E. Klotz and P. Vock. "Spiral volumetric CT with single-breath-hold technique, continuous transport, and continuous scanner rotation." *Radiology*, **176**(1): 181, **1990**.

[Kalender1988] W. A. Kalender, E. Klotz and L. Kostaridou. "Algorithm for noise suppression in dual energy ct material density images." *IEEE Trans. Med. Imaging*, **7**(3): 218, **1988**.

[Kay1993] S. M. Kay. Fundamentals of statistical signal processing: Estimation Theory. Prentice Hall PTR, Upper Saddle River, NJ, **1993**. ISBN 0133457117 9780133457117 013504135X 9780135041352.

[Kelcz1979] F. Kelcz, P. M. Joseph and S. K. Hilal. "Noise Considerations in Dual Energy CT Scanning". *Med. Phys.*, **6**(5): 418, **1979**.

[Brown2015] S. Z. Kevin M. Brown, Gilad Shechter. "Impact of Spectral Separation in Dual-Energy CT with Anti-Correlated Statistical Reconstruction". In Proc. 13th Int. Meet. Fully Three-Dimensional Image Reconstr., 493 – 496. **2015**.

[Knoll2010] G. F. Knoll. Radiation detection and measurement. John Wiley & Sons, 4 ed., **2010**. ISBN 978-0470131480.

[Koehler2011] T. Köhler, K. Jürgen Engel and E. Rössl. "Noise properties of grating-based x-ray phase contrast computed tomography". *Med. Phys.*, **38**(S1): S106, **2011**.

[Koonce2014] J. D. Koonce, R. Vliegenthart, U. J. Schoepf, B. Schmidt, A. E. Wahlquist, P. J. Nietert, G. Bastarrika, T. G. Flohr and F. G. Meinel. "Accuracy of dual-energy computed tomography for the measurement of iodine concentration using cardiac CT protocols: validation in a phantom model". *Eur. Radiol.*, **24**(2): 512, **2014**.

[Kraft2009a] P. Kraft, A. Bergamaschi, C. Bronnimann, R. Dinapoli, E. F. Eikenberry, H. Graafsma, B. Henrich, I. Johnson, M. Kobas, A. Mozzanica, C. M. Schleputz and B. Schmitt. "Characterization and Calibration of PILATUS Detectors". *IEEE Trans. Nucl. Sci.*, **56**(3): 758, **2009**.

[Leblans2011] P. Leblans, D. Vandenbroucke and P. Willems. "Storage phosphors for medical imaging". *Materials (Basel).*, **4**(6): 1034, **2011**.

[Lee2003] S. C. Lee, H. K. Kim, I. K. Chun, M. H. Cho, S. Y. Lee and M. H. Cho. "A flat-panel detector based micro-CT system: performance evaluation for small-animal imaging". *Phys. Med. Biol.*, **48**(24): 4173, **2003**.

[Lee2002] T.-Y. Lee. "Functional CT: physiological models". *Trends Biotechnol.*, **20**(8): S3, **2002**.

[Lehmann1981] L. A. Lehmann. "Generalized image combinations in dual KVP digital radiography". *Med. Phys.*, **8**(5): 659, **1981**.

[Li2015] J. H. Li, Y. M. Du and H. M. Huang. "Accuracy of dual-energy computed tomography for the quantification of iodine in a soft tissue-mimicking phantom". *J. Appl. Clin. Med. Phys.*, **16**(5): 418, **2015**.

[Lucy1974] L. B. Lucy. "An iterative technique for rectification of observed distributions". *Astron. J.*, **79**(6): 745, **1974**.

[Mahesh2009] M. Mahesh and J. M. Hevezi. "Slice Wars vs Dose Wars in Multiple-Row Detector CT". *J. Am. Coll. Radiol.*, **6**(3): 201, **2009**.

[Mallinson2014] P. Mallinson, G. Antoniades, P. McLaughlin, L. Louis, S. Nicolaou, P. Munk and H. Ouellette. "Dual-Energy Computed Tomographic Tendon Algorithm in Acute Trauma: Initial Experiences." *Journal of computer assisted tomography*, **00**(00): 1, **2014**.

[Malm1974] H. L. Malm, M. Martini and M. Martini. "Polarization phenomena in CdTe nuclear radiation detectors". *IEEE Trans. Nucl. Sci.*, **21**(1): 322, **1974**.

[Marin2015] D. Marin, J. J. Pratts-Emanuelli, A. Mileto, D. B. Husarik, M. R. Bashir, R. C. Nelson and D. T. Boll. "Interdependencies of acquisition, detection, and re-

construction techniques on the accuracy of iodine quantification in varying patient sizes employing dual-energy CT". *Eur. Radiol.*, **25**(3): 679, **2015**.

[McCollough2015] C. H. McCollough, S. Leng, L. Yu and J. G. Fletcher. "Dual- and Multi-Energy CT: Principles, Technical Approaches, and Clinical Applications." *Radiology*, **276**(3): 637, **2015**.

[Mechlem2016] K. Mechlem, S. Allner, S. Ehn, E. Braig, F. Pfeiffer, K. Mei, M. Daniela and P. Noël. "A post-processing algorithm for dual energy CT material selective images using learned dictionaries". *Biomedical Physics & Engineering Express*, **3**(2): 1, **2016**.

[Mehta1986] P. K. Mehta. Concrete. Structure, Properties And Materials. Prentice-Hall, Englewood Cliffs, NJ, **1986**.

[Muenzel2016] D. Muenzel, D. Bar-Ness, E. Roessl, I. Blevis, M. Bartels, A. A. Fingerle, S. Ruschke, P. Coulon, H. Daerr, F. K. Kopp, B. Brendel, A. Thran, M. Rokni, J. Herzen, L. Boussel, F. Pfeiffer, R. Proksa, E. J. Rummeny, P. Douek and P. B. Noël. "Spectral Photon-counting CT: Initial Experience with Dual–Contrast Agent K-Edge Colonography". *Radiology*, 160890, **2016**.

[Murty1965] R. C. Murty. "Effective Atomic Numbers of Heterogeneous Materials". *Nature*, **207**(4995): 398, **1965**.

[Nachtrab2011] F. Nachtrab, S. Weis, P. Keßling, F. Sukowski, U. Haßler, T. Fuchs, N. Uhlmann and R. Hanke. "Quantitative material analysis by dual-energy computed tomography for industrial NDT applications". *Nucl. Instruments Methods Phys. Res. Sect. A Accel. Spectrometers, Detect. Assoc. Equip.*, **633**(SUPPL. 1): S159, **2011**.

[Nash2002] K. Nash, A. Hafeez and S. Hou. "Hospital-acquired renal insufficiency". *Am. J. Kidney Dis.*, **39**(5): 930, **2002**.

[Nowak2012] T. Nowak, M. Hupfer, F. Althoff, R. Brauweiler, F. Eisa, C. Steiding and W. a. Kalender. "Time-delayed summation as a means of improving resolution on fast rotating computed tomography systems." *Med. Phys.*, **39**(4): 2249, **2012**.

[Pache2010] G. Pache, B. Krauss, P. Strohm, U. Saueressig, P. Blanke, S. Bulla, O. Schäfer,

P. Helwig, E. Kotter, M. Langer and T. Baumann. "Dual-Energy CT Virtual Noncalcium Technique: Detecting Posttraumatic Bone Marrow Lesions—Feasibility Study". *Radiology*, **256**(2): 617, **2010**.

[Panta2014] R. K. Panta, M. Walsh, S. Bell, N. Anderson, A. Butler and P. Butler. "Energy Calibration of the Pixels of Spectral X-ray Detectors." *IEEE Trans. Med. Imaging*, **0062**(c): 1, **2014**.

[Pauwels2015] E. Pauwels, J. Dhaene, A. De Muynck, M. Dierik and L. van Hoorebeke. "Optimization of scanner parameters for dual energy micro-CT". In Proc. Tomogr. Mater. Struct., 87–91. **2015**.

[Pelzer2013] G. Pelzer, T. Weber, G. Anton, R. Ballabriga, F. Bayer, M. Campbell, T. Gabor, W. Haas, F. Horn, X. Llopart, N. Michel, U. Mollenbauer, J. Rieger, A. Ritter, I. Ritter, P. Sievers, S. Wölfel, W. S. Wong, A. Zang and T. Michel. "Grating-based x-ray phase-contrast imaging with a multi energy-channel photon-counting pixel detector." *Opt. Express*, **21**(22): 25677, **2013**.

[Pennicard2013] D. Pennicard, S. Lange, S. Smoljanin, H. Hirsemann, H. Graafsma, M. Epple, M. Zuvic, M.-O. Lampert, T. Fritzsch and M. Rothermund. "The LAMBDA photon-counting pixel detector". *J. Phys. Conf. Ser.*, **425**(6): 062010, **2013**.

[Persson2012] M. Persson and H. Bornefalk. "A framework for evaluating threshold variation compensation methods in photon counting spectral CT." *IEEE Trans. Med. Imaging*, **31**(10): 1861, **2012**.

[Petersilka2008] M. Petersilka, H. Bruder, B. Krauss, K. Stierstorfer and T. G. Flohr. "Technical principles of dual source CT". *Eur. J. Radiol.*, **68**(3): 362, **2008**.

[Petersilka2010] M. Petersilka, K. Stierstorfer, H. Bruder and T. Flohr. "Strategies for scatter correction in dual source CT." *Med. Phys.*, **37**(11): 5971, **2010**.

[Petrongolo2015a] M. Petrongolo, X. Dong and L. Zhu. "A general framework of noise suppression in material decomposition for dual-energy CT". *Med. Phys.*, **42**(8): 4848, **2015**.

[Petrongolo2015] M. Petrongolo and L. Zhu. "Noise Suppression for Dual-Energy CT through Entropy Minimization". *IEEE Trans. Med. Imaging*, **0062**(c): 1, **2015**.

[Pfeiffer2008] F. Pfeiffer, M. Bech, O. Bunk, P. Kraft, E. F. Eikenberry, C. Brönnimann, C. Grünzweig and C. David. "Hard-X-ray dark-field imaging using a grating interferometer." *Nat. Mater.*, **7**(2): 134, **2008**.

[Pfeiffer2006] F. Pfeiffer, T. Weitkamp, O. Bunk and C. David. "Phase retrieval and differential phase-contrast imaging with low-brilliance X-ray sources". *Nat. Phys.*, **2**(4): 258, **2006**.

[Pomerantz2013] S. R. Pomerantz, S. Kamalian, D. Zhang, R. Gupta, O. Rapalino, D. V. Sahani and M. H. Lev. "Virtual Monochromatic Reconstruction of Dual-Energy Unenhanced Head CT at 65–75 keV Maximizes Image Quality Compared with Conventional Polychromatic CT". *Radiology*, **266**(1): 318, **2013**.

[Prevrhal2004] S. Prevrhal. "Beam hardening correction and quantitative micro-CT". In U. Bonse (editor), Proc. SPIE, 152. International Society for Optics and Photonics, **2004**.

[Prokesch2016] M. Prokesch, S. A. Soldner, A. G. Sundaram, M. D. Reed, H. Li, J. F. Eger, J. L. Reiber, C. L. Shanor, C. L. Wray, A. J. Emerick, A. F. Peters and C. L. Jones. "CdZnTe Detectors Operating at X-ray Fluxes of". *IEEE Trans. Nucl. Sci.*, **63**(3): 1854, **2016**.

[Rajbhandary2015] P. L. Rajbhandary and N. J. Pelc. "Statistical bias in material decomposition in low photon statistics region". *Proc. SPIE Med. Imaging*, **9412**: 94124W, **2015**.

[Richardson1972] W. H. RICHARDSON. "Bayesian-Based Iterative Method of Image Restoration". *J. Opt. Soc. Am.*, **62**(1): 55, **1972**.

[Roessl2012] E. Roessl, H. Daerr, K. J. Engel, A. Thran, C. Schirra and R. Proksa. "Combined effects of pulse pile-up and energy response in energy-resolved, photon-counting computed tomography". *IEEE Nucl. Sci. Symp. Conf. Rec.*, (1): 2309, **2012**.

[Roessl2009] E. Roessl and C. Herrmann. "Cramér-Rao lower bound of basis image noise in multiple-energy x-ray imaging." *Phys. Med. Biol.*, **54**(5): 1307, **2009**.

[Roessl2006] E. Roessl and R. Proksa. "Optimal energy threshold arrangement in photon-

counting spectral x-ray imaging". *2006 IEEE Nucl. Sci. Symp. Conf. Rec.*, (6): 1950, **2006**.

[Roessl2007] E. Roessl and R. Proksa. "K-edge imaging in x-ray computed tomography using multi-bin photon counting detectors." *Phys. Med. Biol.*, **52**(15): 4679, **2007**.

[Roessl2007a] E. Roessl, A. Ziegler and R. Proksa. "On the influence of noise correlations in measurement data on basis image noise in dual-energylike x-ray imaging." *Med. Phys.*, **34**(3): 959, **2007**.

[Rowlands2002] J. A. Rowlands. "The physics of computed radiography". *Phys. Med. Biol.*, **47**: R123 , **2002**.

[Ruat2014] M. Ruat and C. Ponchut. "Defect signature, instabilities and polarization in CdTe X-ray sensors with quasi-ohmic contacts". *J. Instrum.*, **9**(04): C04030, **2014**.

[Sakdinawat2010] A. Sakdinawat and D. Attwood. "Nanoscale X-ray imaging". *Nat. Photonics*, **4**(12): 840, **2010**.

[Samei1998] E. Samei, M. J. Flynn and D. a. Reimann. "A method for measuring the presampled MTF of digital radiographic systems using an edge test device". *Med. Phys.*, **25**(1): 102, **1998**.

[Sarapata2014] A. Sarapata, M. Chabior, C. Cozzini, J. I. Sperl, D. Bequé, O. Langner, J. Coman, I. Zanette, M. Ruiz-Yaniz and F. Pfeiffer. "Quantitative electron density characterization of soft tissue substitute plastic materials using grating-based x-ray phase-contrast imaging". *Rev. Sci. Instrum.*, **85**(10), **2014**.

[Sarapata2015] A. Sarapata, M. Willner, M. Walter, T. Duttenhofer, K. Kaiser, P. Meyer, C. Braun, A. Fingerle, P. B. Noël, F. Pfeiffer and J. Herzen. "Quantitative imaging using high-energy X-ray phase-contrast CT with a 70 kVp polychromatic X-ray spectrum." *Opt. Express*, **23**(1): 523, **2015**.

[Sasov1998] A. Sasov and D. Van Dyck. "Desktop X-ray microscopy and microtomography." *J. Microsc.*, **191**(Pt 2): 151, **1998**.

[Schirra2014] C. Schirra, A. Thran, H. Daerr, E. Roessl and R. Proksa. "Towards in-vivo K-edge imaging using a new semi-analytical calibration method". *Proc. SPIE Med. Imaging*, **9033**: 90330N, **2014**.

[Schirra2014a] C. O. Schirra, B. Brendel, M. A. Anastasio and E. Roessl. "Spectral CT: A technology primer for contrast agent development". *Contrast Media Mol. Imaging*, **9**(1): 62, **2014**.

[Schlomka2008] J. P. Schlomka, E. Roessl, R. Dorscheid, S. Dill, G. Martens, T. Istel, C. Bäumer, C. Herrmann, R. Steadman, G. Zeitler, a. Livne and R. Proksa. "Experimental feasibility of multi-energy photon-counting K-edge imaging in pre-clinical computed tomography." *Phys. Med. Biol.*, **53**(15): 4031, **2008**.

[Schmahl1980] G. Schmahl, D. Rudolph, B. Niemann and O. Christ. "Zone-plate X-ray microscopy." *Q. Rev. Biophys.*, **13**(3): 297, **1980**.

[Schreuder2008] T. Schreuder, B. Verwer, C. van Nieuwkerk and C. Mulder. "Nonalcoholic fatty liver disease: An overview of current insights in pathogenesis, diagnosis and treatment". *World Journal of Gastroenterology*, **14**(16): 2474, **2008**.

[Seino2008] T. Seino, S. Kominami, Y. Ueno and K. Amemiya. "Pulsed Bias Voltage Shutdown to Suppress the Polarization Effect for a CdTe Radiation Detector". *IEEE Trans. Nucl. Sci.*, **55**(5): 2770, **2008**.

[Shefer2013] E. Shefer, A. Altman, R. Behling, R. Goshen, L. Gregorian, Y. Roterman, I. Uman, N. Wainer, Y. Yagil and O. Zarchin. "State of the Art of CT Detectors and Sources: A Literature Review". *Curr. Radiol. Rep.*, **1**(1): 76, **2013**.

[Sibarita2005] J.-B. Sibarita. "Deconvolution Microscopy". In J. Rietdorf (editor), Microscopy Techniques, 201–243. Springer Berlin Heidelberg, **2005**. ISBN 978-3-540-31545-2.

[Silva2015] J. M. d. S. e. Silva, I. Zanette, P. B. Noël, M. B. Cardoso, M. A. Kimm and F. Pfeiffer. "Three-dimensional non-destructive soft-tissue visualization with X-ray staining micro-tomography". *Sci. Rep.*, **5**: 14088, **2015**.

[Smith2009] G. E. Smith. "The invention and early history of the CCD". *Nucl. Instru-*

ments Methods Phys. Res. Sect. A Accel. Spectrometers, Detect. Assoc. Equip., **607**(1): 1, **2009**.

[Sones1989] R. A. Sones and G. T. Barnes. "Noise correlations in images acquired simultaneously with a dual-energy sandwich detector". *Med. Phys.*, **16**(6): 858, **1989**.

[Forbild2016] K. Sourbelle. "Forbild Thorax Phantom", **2016**.

[Spieler2005] H. Spieler. Semiconductor Detector Systems. Oxford University Press, **2005**. ISBN 9780198527848.

[Sriwayu2015] W. O. Sriwayu, F. Haryanto, S. N. Khotimah and F. D. E. Latief. "Beam hardening and smoothing correction effects on performance of micro-ct SkyScan 1173 for imaging low contrast density materials". In AIP Conf. Proc., 060014. **2015**.

[Taguchi2013] K. Taguchi and J. S. Iwanczyk. "Vision 20/20: Single photon counting x-ray detectors in medical imaging." *Med. Phys.*, **40**(10): 100901, **2013**.

[Takahashi2010] N. Takahashi, T. J. Vrtiska, A. Kawashima, R. P. Hartman, A. N. Primak, J. G. Fletcher and C. H. McCollough. "Detectability of Urinary Stones on Virtual Nonenhanced Images Generated at Pyelographic-Phase Dual-Energy CT". *Radiology*, **256**(1): 184, **2010**.

[Thim2011] J. Thim, B. Norlin, M. O'Nils, S. Abdalla and B. Oelmann. "Realizing increased sub-pixel spatial resolution in X-ray imaging using displaced multiple images". *Nucl. Instruments Methods Phys. Res. Sect. A Accel. Spectrometers, Detect. Assoc. Equip.*, **633**: S247, **2011**.

[Tromberg2005] B. J. Tromberg, A. Cerussi, N. Shah, M. Compton, A. Durkin, D. Hsiang, J. Butler and R. Mehta. "Imaging in breast cancer: Diffuse optics in breast cancer: detecting tumors in pre-menopausal women and monitoring neoadjuvant chemotherapy". *Breast Cancer Research*, **7**(6): 279, **2005**.

[Uher2011] J. Uher and J. Jakubek. "Equalization of Medipix2 imaging detector energy thresholds using measurement of polychromatic X-ray beam attenuation". *J. Instrum.*, **6**(11): C11012, **2011**.

[Ullberg2013] C. Ullberg, M. Urech, N. Weber, A. Engman, A. Redz and F. Henckel. "Measurements of a dual-energy fast photon counting CdTe detector with integrated charge sharing correction". *Proc. SPIE Med. Imaging*, **8668**: 86680P, **2013**.

[VanAarle2014] W. van Aarle, K. J. Batenburg, G. Van Gompel, E. Van de Casteele and J. Sijbers. "Super-resolution for computed tomography based on discrete tomography." *IEEE Trans. Image Process.*, **23**(3): 1181, **2014**.

[Abbema2015] J. K. van Abbema, M.-J. van Goethem, M. J. W. Greuter, A. van der Schaaf, S. Brandenburg and E. R. van der Graaf. "Relative electron density determination using a physics based parameterization of photon interactions in medical DECT". *Phys. Med. Biol.*, **60**(9): 3825, **2015**.

[VanBeek2008] E. J. van Beek and E. A. Hoffman. "Functional Imaging: CT and MRI". *Clin. Chest Med.*, **29**(1): 195, **2008**.

[VandeCasteele2002] E. Van de Casteele, D. Van Dyck, J. Sijbers and E. Raman. "An energy-based beam hardening model in tomography." *Phys. Med. Biol.*, **47**(23): 4181, **2002**.

[Vavrik2011] D. Vavrik. "CT artefact reduction by signal to thickness calibration function shaping". *Nucl. Instruments Methods Phys. Res. Sect. A Accel. Spectrometers, Detect. Assoc. Equip.*, **633**: S177, **2011**.

[Wang2008] C. L. Wang, R. H. Cohan, J. H. Ellis, E. M. Caoili, G. Wang and I. R. Francis. "Frequency, Outcome, and Appropriateness of Treatment of Nonionic Iodinated Contrast Media Reactions". *Am. J. Roentgenol.*, **191**(2): 409, **2008**.

[Weber2011] T. Weber, F. Bayer, W. Haas, G. Pelzer, J. Rieger, A. Ritter, L. Wucherer, J. Durst, T. Michel and G. Anton. "Energy-dependent visibility measurement and its simulation in X-ray Talbot interferometry", **2011**.

[White1977] D. White. "An analysis of the Z-dependence of photon and electron interactions". *Phys. Med. Biol.*, **22**(2): 219, **1977**.

[ICRU44] D. R. White, J. Booz, R. V. Griffith, J. J. Spokas and I. J. Wilson. "Report 44". *J. Int. Comm. Radiat. Units Meas.*, **os23**(1), **1989**.

[Willis2011] C. E. Willis, Y. Y. Vinogradskiy, B. K. Lofton and R. A. White. "Gain and off-

set calibration reduces variation in exposure-dependent SNR among systems with identical digital flat-panel detectors." *Med. Phys.*, **38**(7): 4422, **2011**.

[Willner2016] M. Willner, M. Viermetz, M. Marschner, K. Scherer, C. Braun, A. Fingerle, P. Noël, E. Rummeny, F. Pfeiffer and J. Herzen. "Quantitative Three-Dimensional Imaging of Lipid, Protein, and Water Contents via X-Ray Phase-Contrast Tomography". *PLoS One*, **11**(3): e0151889, **2016**.

[Wischmann2002] H. Wischmann, H. Luijendijk, H. Meulenbrugge, M. Overdick, R. Schmid and K. Kiani. "Correction of amplifier nonlinearity, offset, gain, temporal artifacts, and defects for flat-panel digital imaging devices". In Proc. SPIE Med. Imaging, vol. 4682, 427–437. **2002**.

[Woodard1986] H. Q. Woodard and D. R. White. "The composition of body tissues". *Br. J. Radiol.*, **59**: 1209, **1986**.

[Yamada2014] Y. Yamada, M. Jinzaki, T. Hosokawa, Y. Tanami, T. Abe and S. Kuribayashi. "Abdominal CT: An intra-individual comparison between virtual monochromatic spectral and polychromatic 120-kVp images obtained during the same examination". *Eur. J. Radiol.*, **83**(10): 1715, **2014**.

[Yu2011] L. Yu, J. A. Christner, S. Leng, J. Wang, J. G. Fletcher and C. H. McCollough. "Virtual monochromatic imaging in dual-source dual-energy CT: Radiation dose and image quality". *Med. Phys.*, **38**(12): 6371, **2011**.

[Yu2012] L. Yu, S. Leng and C. H. McCollough. "Dual-energy CT-based monochromatic imaging." *AJR. Am. J. Roentgenol.*, **199**(5 Suppl): S9, **2012**.

[Yuan2012] R. Yuan, W. P. Shuman, J. P. Earls, C. J. Hague, H. A. Mumtaz, A. Scott-Moncrieff, J. D. Ellis, J. R. Mayo and J. A. Leipsic. "Reduced Iodine Load at CT Pulmonary Angiography with Dual-Energy Monochromatic Imaging: Comparison with Standard CT Pulmonary Angiography—A Prospective Randomized Trial". *Radiology*, **262**(1): 290, **2012**.

[Zhang2011] D. Zhang, X. Li and B. Liu. "Objective characterization of GE Discovery CT750 HD scanner: Gemstone spectral imaging mode". *Med. Phys.*, **38**(3): 1178, **2011**.

List of Figures

List of Tables

List of abbreviations

1D one-dimensional

2D two-dimensional

3D three-dimensional

ADC analog-to-digital converter

ASIC application-specific integrated circuit

CCD charge-coupled device

CDI coherent diffraction imaging

CdTe cadmium-telluride

CNR contrast-to-noise ratio

CR computed radiography

CRLB Cramér-Rao lower bound

CSM charge-summing mode

CT computed tomography

CTDIvol volumetric computed tomography dose index

EID energy-integrating detector

FBP filtered back-projection

FOV field-of-view

FPD flat-panel detector

FWHM full width at half-maximum value

HA calcium-hydroxyapatite

HU Hounsfield units

ICRU International Commission on Radiation Units

LSF line-spread function

MLE maximum-likelihood estimator

MTF modulation-transfer function

NDT non-destructive testing

NLL negative log-likelihood

NPS noise-power spectrum

PCD photon-counting detector

PLB Polychromatic Beer-Lambert

PMMA poly-methyl methacrylate

PSF point-spread function

PVC poly-vinyl chloride

RMS root-mean-squared

ROI region-of-interest

SBI spectral base image

SID source-to-image distance

SIR statistical iterative reconstruction

SNR signal-to-noise ratio

SOD source-to-object distance

TDS time-delayed summation

THL energy threshold

TXM transmission x-ray microscopy

VMI virtual-monochromatic image

XDM x-ray deconvolution microscopy

List of publications

1st author peer-reviewed publications:

- S. Ehn, F. Epple, A. Fehringer, D. Pennicard, H. Graafsma, P. Noël and F. Pfeiffer
  "X-Ray Deconvolution Microscopy"
  Biomedical Optics Express **7**(4): 1227 (2016)

- S. Ehn, T. Sellerer, K. Mechlem, A. Fehringer, F. Epple, J. Herzen, F. Pfeiffer and P. Noël
  "Basis Material Decomposition in Spectral CT Using a Semi-Empirical, Polychromatic Adaption of the Beer–Lambert Model"
  Physics in Medicine and Biology **62**(1): N1 (2016)

- S. Ehn, T. Sellerer, D. Muenzel, A. Fingerle, F. Kopp, M. Duda., K. Mei, B. Renger, J. Herzen, J. Dangelmaier, B. Schwaiger, A. Sauter, I. Riederer, M. Renz, R. Braren, E. Rummeny, F. Pfeiffer and P. Noël
  "Assessment of Quantification Accuracy and Image Quality of a Full-Body Dual-Layer Spectral CT System"
  submitted to: Journal of Applied Clinical Medical Physics (2017)

Contributing author peer-reviewed publications:

- F. Epple, S. Ehn, P. Thibault, T. Koehler, G. Potdevin, J. Herzen, D. Pennicard, H. Graafsma, P. Noël and F. Pfeiffer
  "Phase Unwrapping in Spectral X-Ray Differential Phase-Contrast Imaging With an Energy-Resolving Photon-Counting Pixel Detector"
  IEEE Transactions on Medical Imaging **34**(3): 816 (2015)

- K. Mechlem, S. Allner, S. Ehn, K. Mei, E. Braig, D. Muenzel, F. Pfeiffer and P. Noël
  "A Post-Processing Algorithm for Dual Energy CT Material Selective Images Using Learned Dictionaries"
  Biomedical Physics & Engineering Express **3**(2): 025009 (2016)

Conference presentations and proceedings:

- S. Ehn, M. Epple, P. Noël, S. Kaczmarz, B. Adam, D. Pennicard, H. Graafsma, D. Renker and F. Pfeiffer
  "Spectral X-Ray Imaging Methods Using the New LAMBDA Detector"
  Talk at the *International Workshop on X-ray and Neutron Phase Imaging with Gratings (XNPIG)*, Garmisch Partenkirchen, Germany (2014)

- K. Mechlem, S. Ehn, T. Sellerer, F. Pfeiffer and P. Noël
  "Statistical iterative material image reconstruction for spectral CT using a semi-empirical forward model"
  Proceedings of SPIE Medical Imaging **10132**: 1013238 (2017)

- T. Sellerer, S. Ehn, K. Mechlem, F. Pfeiffer, J. Herzen and P. Noël
  "A polychromatic adaption of the Beer-Lambert model for spectral decomposition"
  Proceedings of SPIE Medical Imaging **10132**: 101323H (2017)

Acknowledgments

This work would not have been possible without the kind support of many people around me. It is impossible to name everyone who provided help and guidance throughout the last years but I want to take the opportunity to thank a few colleagues and friends in person. My cordial thanks to

- **My whole family,**
  for your loving and continuous support throughout my whole life and for making it possible to pursue my goals. Thank you Mona, my ‘lucky shot’, for your patience and for support when some things just wont work out.

- **Prof. Franz Pfeiffer,**
  for giving me the opportunity to do my research at the E17 chair. From my first day as a Diploma student towards the end of my PhD project you have always supported so many of my ideas. Thank you also for giving me the opportunity to take the responsibility in several projects and for providing all the necessary framework for all of us at E17,

- **PD Dr. Peter Noël,**
  for being my mentor during this project and for all the helpful and - sometimes - funny discussion on our projects,

- **Thorsten and Korbinian,**
  and the rest of the ‘spectral island’ for all the help you provided and the funny moments we share day to day. Special thanks to Thorsten for assisting me with so many measurements and Korbinian for really digging into the spectral processing code. Also thank you both for proof-reading this thesis and for providing several helpful comments,

- **My former supervisor Michael Epple,**
  for introducing me to the field of photon-counting detectors and the ideas of spectral imaging,

- **Our contacts and collaborators at various detector manufacturers,**

namely Christer and Nathanael (XCounter AB), Christian, Alexandre and Michael (Dectris Ltd.) and Heinz and David (DESY/XSpectrum GmbH) for all the valuable input on technical questions to various detectors used throughout this work,

- **The E17 IT experts,**
  for providing and maintaining the `pyCT` reconstruction framework and for keeping the computing infrastructure up and running for all of us,

- **My office mates and 'neighbors' at the chair,**
  for the coffee breaks and the general help you have always provided,

- **Lorenz, Matthias and Kai**
  for profound discussions at various Schafkopf rounds,

- **Nelly,**
  for helping with so many organizational issues and keeping track of all our accounts when ordering new equipment,

- **All other people who could not be named here in person!**